

Accurate Statistics from Optical Transmission Matrix Measurements

Nauwkeurige statistiek uit metingen
van de optische transmissiematrix

Pritam Pai

Cover

Cover designed by Ishani Sarkar, freelance photographer. It features an artistic representation of scattering invariant modes that are transmitted the same way through a transparent and a scattering medium.

Pai, Pritam

Accurate Statistics from Optical Transmission Matrix Measurements

P. Pai - Utrecht

Universiteit Utrecht

Faculteit Bètawetenschappen

Departement Natuur- en Sterrenkunde

Thesis Universiteit Utrecht - With a summary in Dutch

ISBN: 978-94-640-2156-1

Accurate Statistics from Optical Transmission Matrix Measurements

Nauwkeurige statistiek uit metingen
van de optische transmissiematrix

(met een samenvatting in het Nederlands)

Proefschrift

ter verkrijging van de graad van doctor
aan de Universiteit Utrecht op gezag van
de rector magnificus, prof. dr. H.R.B.M. Kummeling,
ingevolge het besluit van het college voor promoties
in het openbaar te verdedigen op
dinsdag 31 maart 2020 des ochtends te 10.30 uur

door

Pritam Pai

geboren op 20 oktober 1991 te Puducherry, India

Promotor: Prof. dr. A. P. Mosk
Copromotor: Dr. ir. S. Faez

This work is financially supported by the Netherlands Organisation for Scientific Research (NWO).

Contents

1	Introduction	1
2	Theory of light transport	7
2.1	Diffusion	7
2.2	General approach	9
2.3	Relation between the S-matrix and the dyadic Green's function	10
2.4	Transmission channels	13
2.4.1	Marchenko-Pastur and DMPK distributions	16
3	Optical transmission matrix measurement sampled on a dense hexagonal lattice	25
3.1	Introduction	25
3.2	Sampling the transmission matrix	27
3.3	Measurement and data processing	30
3.3.1	Apparatus	30
3.3.2	Experimental sampling density	32
3.3.3	Digital filtering of the transmitted fields	32
3.3.4	Sampling the transmitted field	32
3.3.5	Phase drift correction	34
3.4	TM of a zero-thickness reference	34
3.5	Conclusion	37
3.A	Geometrical limitations	39
3.B	Procedural details	40
3.B.1	Auto-focusing on the sample	40
3.B.2	Step size calibration	41
3.B.3	Field retrieval using off-axis holography	44
3.B.4	Digital correction for out-of-focus images	46
3.B.5	Affine transformation	47
3.C	Eigenvalue statistics	48
4	Resampling the transmission matrix in an aberration-corrected Bessel mode basis	55
4.1	Resampling procedure	56
4.2	Implementation for a zero-thickness reference	59

4.3	Transmission eigenvectors of a thin slab of air	63
4.3.1	Airy spot basis	64
4.3.2	Analogy with Fox-Li modes of a cavity with finite mirrors	69
4.3.3	Bessel mode basis	72
4.4	Conclusion	75
5	Mesoscopic correlations in transmission matrices of strongly scattering media	79
5.1	Methods	80
5.1.1	Sample preparation	80
5.1.2	TM measurement	81
5.2	Singular value distribution	82
5.2.1	Comparison with a filtered DMPK model	85
5.3	Properties of individual transmission channels	87
5.3.1	Spatial profile	87
5.3.2	Intensity statistics	89
5.4	Conclusion	93
6	Scattering invariant modes	97
6.1	Definition	97
6.2	Experimental determination of SIMs	99
6.3	SIM projection	101
6.4	Eigenvalue statistics	103
6.5	Avoidance of scatterers	106
6.5.1	Single scattering layer	107
6.5.2	Double scattering layer	112
6.6	Conclusion	121
7	Summary and outlook	125
	Samenvatting en vooruitzichten	129
	Acknowledgments	133
	About the author	137

1 Introduction

We perceive a large part of the world around us using our sense of sight. We see objects because light scatters off them and reaches our eye or an optical detector. In this regard, light scattering is indispensable for imaging. However, when another object lies between the detector and the object we wish to look at, the light reaching the detector is distorted and the amount of distortion depends on how strongly scattering the obstructing object is. To obtain an accurate image in these situations, we have to compensate for the undesirable aberrations.

In the weak or single scattering regime where most of the detected light is ballistic, e.g., in atmospheric imaging and earth-based astronomy, the distorted wavefronts can be corrected with deformable mirrors and adaptive optics techniques [1–3]. On the other hand, many common everyday objects such as paper, paint, milk and skin are examples of strong scattering where an image transmitted through such an object is totally unrecognizable. In this multiple scattering regime it is a much greater challenge to retrieve the original image from the (completely) scrambled transmitted light. Typically, coherent light is scrambled into seemingly random speckle patterns after a few random scattering events.

The first experimental demonstration of focusing light through an opaque medium was shown in 2007 [4]. The experimentalists succeeded in doing so by shaping the wavefront of the incident beam with a spatial light modulator (SLM) to maximize constructive interference at the output. The basic concept of wavefront shaping is illustrated in Fig. 1.1, which is taken from the original paper. Here, the optimal wavefront was found by measuring a vector of transmission coefficients and conjugating the phases.

The other outstanding breakthrough of controlling the transmission of light through diffuse media, first experimentally achieved by Popoff and coauthors [5], was the measurement of rows and columns of the optical transmission matrix (TM) [6–10] of the scattering sample, linking its input and output modes. This enabled a method to predict the transmission response of the medium to any input field and this technique was subsequently used for successful image transmission through strongly scattering media [11], fulfilling a visionary idea by Freund [12]. Moreover, polarization properties were analyzed by using the polarization transmission matrix [13].

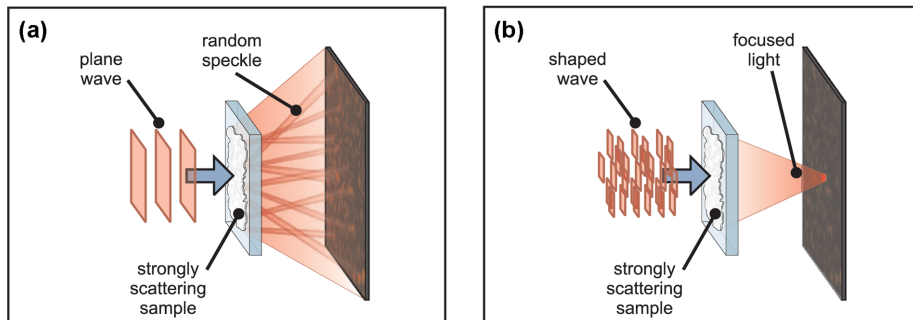


Figure 1.1: Concept of wavefront shaping. (a) A plane wave transmitted through a strongly scattering sample is randomly scattered, but (b) an appropriately shaped incident wavefront can transmit a single focus. Image taken from [4].

These two pioneering feats of wavefront shaping and measuring the TM, along with the advent of advanced and fast SLM technology, burst the field of experimental optical complex media wide open, with a plethora of research papers published in the last decade (for review articles, see Refs. [7, 9]).

Apart from its imaging applications, the TM is an important quantity because its statistics are related to the transmission eigenchannels of the sample, which are the building blocks that transport light in the medium [14–18]. Many properties of light transport in scattering media, such as correlations between amplitudes or intensities of speckles, can be understood in terms of channels. Therefore, transmission channels have received significant attention in recent years [9, 19–34].

Outline of this thesis

Since the transmission matrix is a powerful tool to understand the transport of light and to exploit a random medium for imaging purposes, this thesis mainly focuses on experimental improvements in measuring the transmission matrix coupled with an exciting new application of finding scattering invariant modes of the system.

Chapter 2 contains the theoretical basics for the rest of the thesis. We review the theoretical definition of the transmission matrix and link it to the dyadic Green’s function. Additionally, we introduce the concept of transmission channels in the framework of radio frequency physics and express its equivalence in optics. We also discuss the predicted distribution of the channels for strongly scattering samples.

Chapter 3 shows a novel experimental procedure for measuring the TM of light waves in a slab geometry based on sampling the light field on a hexagonal lattice close to the critical sampling density. The procedure and analysis is demonstrated on a clear sample which serves as an important reference for other systems and geometries such as dense scattering media.

Chapter 4 goes one step further and explains why the TM is better expressed in a basis of Bessel modes of the first kind and describes how to resample the TM in this basis. Moreover, we measure the TM of a finite thickness of air and show that its eigenvectors have a direct link with the Fox-Li modes of a confocal cavity with finite mirrors.

The experimental procedure developed in **Chapters 3** and **4** are put to use in **Chapter 5**, where we study the statistics and properties of the transmission channels of a strongly scattering sample of zinc oxide nanopowder. We observe mesoscopic correlations in the sample by comparing the experimental results to a theoretical model. We also investigate the spatial profiles and speckle intensity statistics of the transmission channels and compare these to theoretical predictions for light transport through a few channels.

Chapter 6 describes a novel concept, scattering invariant modes (SIMs) of a multiple scattering layer, which are similar to waves transmitted through a transparent medium. Such waves are experimentally projected through a scattering layer and then through air, and the transmitted fields exhibit a high degree of similarity. We compare the statistics of the SIMs to predictions from random matrix theory and investigate whether these special waves avoid scatterers in sparse scattering media.

Finally, **Chapter 7** summarizes the results of this thesis and outlines potential new research that could follow this work.

Bibliography

- [1] R. W. Lee and J. C. Harp, “Weak scattering in random media, with applications to remote probing,” *Proceedings of the IEEE* **57**, 375–406 (1969).
- [2] W. B. Bridges, P. T. Brunner, S. P. Lazzara, T. A. Nussmeier, T. R. O’Meara, J. A. Sanguinet, and W. P. Brown, “Coherent optical adaptive techniques,” *Appl. Opt.* **13**, 291–300 (1974).
- [3] F. F. Roddier, *Adaptive optics in astronomy* (Cambridge, U.K. ; New York : Cambridge University Press, 1999). Includes bibliographical references and index.
- [4] I. M. Vellekoop and A. P. Mosk, “Focusing coherent light through opaque strongly scattering media,” *Opt. Lett.* **32**, 2309–2311 (2007).
- [5] S. M. Popoff, G. Lerosey, R. Carminati, M. Fink, A. C. Boccara, and S. Gigan, “Measuring the transmission matrix in optics: An approach to the study and control of light propagation in disordered media,” *Phys. Rev. Lett.* **104**, 100601 (2010).
- [6] C. W. J. Beenakker, “Random-matrix theory of quantum transport,” *Rev. Mod. Phys.* **69**, 731–808 (1997).
- [7] A. Mosk, A. Lagendijk, G. Lerosey, and M. Fink, “Controlling waves in space and time for imaging and focusing in complex media,” *Nature photonics* **6**, 283–292 (2012).
- [8] M. C. W. van Rossum and T. M. Nieuwenhuizen, “Multiple scattering of classical waves: microscopy, mesoscopy, and diffusion,” *Rev. Mod. Phys.* **71**, 313–371 (1999).
- [9] S. Rotter and S. Gigan, “Light fields in complex media: Mesoscopic scattering meets wave control,” *Rev. Mod. Phys.* **89**, 015005 (2017).
- [10] E. van Putten and A. Mosk, “The information age in optics: Measuring the transmission matrix,” *Physics* **3**, 1–3 (2010).
- [11] S. Popoff, G. Lerosey, M. Fink, A. C. Boccara, and S. Gigan, “Image transmission through an opaque material,” *Nature Communications* **1**, 81 (2010).
- [12] I. Freund, “Looking through walls and around corners,” *Physica A: Statistical Mechanics and its Applications* **168**, 49 – 65 (1990).
- [13] T. W. Kohlgraf-Owens and A. Dogariu, “Transmission matrices of random media: means for spectral polarimetric measurements,” *Opt. Lett.* **35**, 2236–2238 (2010).
- [14] Y. V. Nazarov and Y. M. Blanter, *Quantum Transport: Introduction to Nanoscience* (Cambridge University Press, 2009).
- [15] E. N. Economou and C. M. Soukoulis, “Static conductance and scaling theory of localization in one dimension,” *Phys. Rev. Lett.* **46**, 618–621 (1981).

-
- [16] H. Baranger, D. DiVincenzo, R. Jalabert, and A. Stone, “Classical and quantum ballistic-transport anomalies in microjunctions,” *Phys. Rev. B* **44**, 10637–10675 (1991).
- [17] D. S. Fisher and P. A. Lee, “Relation between conductivity and transmission matrix,” *Phys. Rev. B* **23**, 6851–6854 (1981).
- [18] J. Pendry, A. MacKinnon, and A. Pretre, “Maximal fluctuations — a new phenomenon in disordered systems,” *Physica A: Statistical Mechanics and its Applications* **168**, 400–407 (1990).
- [19] I. M. Vellekoop and A. P. Mosk, “Universal optimal transmission of light through disordered materials,” *Phys. Rev. Lett.* **101**, 120601 (2008).
- [20] Z. Shi and A. Z. Genack, “Transmission eigenvalues and the bare conductance in the crossover to Anderson localization,” *Phys. Rev. Lett.* **108**, 043901 (2012).
- [21] M. Davy, Z. Shi, J. Wang, and A. Z. Genack, “Transmission statistics and focusing in single disordered samples,” *Opt. Express* **21**, 10367–10375 (2013).
- [22] B. Gérardin, J. Laurent, A. Derode, C. Prada, and A. Aubry, “Full transmission and reflection of waves propagating through a maze of disorder,” *Phys. Rev. Lett.* **113**, 173901 (2014).
- [23] X. Hao, L. Martin-Rouault, and M. Cui, “A self-adaptive method for creating high efficiency communication channels through random scattering media,” *Sci. Rep.* **4** (2014).
- [24] S. Liew, S. Popoff, A. Mosk, W. Vos, and H. Cao, “Transmission channels for light in absorbing random media: from diffusive to ballistic-like transport,” *Phys. Rev. B* **89**, 224202–1–224202–10 (2014).
- [25] M. Kim, W. Choi, C. Yoon, G. H. Kim, S. hyun Kim, G.-R. Yi, Q.-H. Park, and W. Choi, “Exploring anti-reflection modes in disordered media,” *Optics Express* **23**, 12740 (2015).
- [26] M. Davy, Z. Shi, J. Park, C. Tian, and A. Z. Genack, “Universal structure of transmission eigenchannels inside opaque media,” *Nature Communications* **6** (2015).
- [27] A. Daniel, L. Liberman, and Y. Silberberg, “Wavefront shaping for glare reduction,” *Optica* **3**, 1104–1106 (2016).
- [28] D. Akbulut, T. Strudley, J. Bertolotti, E. P. A. M. Bakkers, A. Lagendijk, O. L. Muskens, W. L. Vos, and A. P. Mosk, “Optical transmission matrix as a probe of the photonic strength,” *Phys. Rev. A* **94**, 043817 (2016).
- [29] C. W. Hsu, S. F. Liew, A. Goetschy, H. Cao, and A. D. Stone, “Correlation-enhanced control of wave focusing in disordered media,” *Nature Physics* **13**, 497–502 (2017).
- [30] P. Hong, O. S. Ojambati, A. Lagendijk, A. P. Mosk, and W. L. Vos,

- “Three-dimensional spatially resolved optical energy density enhanced by wavefront shaping,” *Optica* **5**, 844–849 (2018).
- [31] P. Fang, C. Tian, L. Zhao, Y. P. Bliokh, V. Freilikher, and F. Nori, “Universality of eigenchannel structures in dimensional crossover,” *Phys. Rev. B* **99**, 094202 (2019).
- [32] H. Yilmaz, C. W. Hsu, A. Goetschy, S. Bittner, S. Rotter, A. Yamilov, and H. Cao, “Angular memory effect of transmission eigenchannels,” *Phys. Rev. Lett.* **123**, 203901 (2019).
- [33] H. Yilmaz, C. W. Hsu, A. Yamilov, and H. Cao, “Transverse localization of transmission eigenchannels,” *Nature Photonics* **13**, 352–358 (2019).
- [34] D. A. B. Miller, “Waves, modes, communications, and optics: a tutorial,” *Adv. Opt. Photon.* **11**, 679–825 (2019).

2 Theory of light transport

In this chapter, we discuss some theoretical concepts of light transport that lay down the framework to interpret the experimental work performed in this thesis. We first explain diffusion theory, which is the most widely used tool to study the diffusion of light in multiple scattering media. We then introduce the Green's function, which solves the forward problem of finding the light field at any given point in space using information of the position and electromagnetic response of all scatterers. Next, we define the scattering matrix which gives the relation between incident and outgoing waves, and subsequently link it to the Green's function. Finally, we discuss the transmission matrix – the tool on which this thesis is entirely based – and elaborate on statistical models predicting the distribution of its transmission channels in disordered media.

2.1 Diffusion

The scattering of light through a physical system can be calculated in several ways, the most exact being the solution of Maxwell's equations [1]. However, given a medium consisting of randomly placed scatterers, there is no analytic solution of Maxwell's equations and it is also computationally impossible to solve because the exact location, shape and size of all scatterers is a priori unknown and impossible to recover using current technological methods. Even if these parameters were known, the computing power required to solve such a problem would follow a power law scaling with the geometry of the system and become unfeasible when the number of scatterers is on the order of a million. The same argument would also hold true for calculating the random walk of all incident photons and determining their eventual interference pattern [2]. The other alternative to an exact solution of Maxwell's equations or of the random walk of photons is to use a statistical approach to predict the general ensemble averaged properties of the light field.

Some important parameters in scattering physics are the transport mean free path ℓ_t and the scattering mean free path ℓ_s . There are several definitions for these quantities, but the most exact ones are that the transport mean free path is equal to momentum correlation length, while the scattering mean free path, which is typically shorter, is equal to the field correlation length. They are

related by [3]

$$\ell_t = \frac{\ell_s}{1 - \langle \cos \theta \rangle}, \quad (2.1)$$

where θ is the angle between the incident and scattered directions and $\langle \dots \rangle$ denotes an average over an ensemble of scatterer positions. For isotropic scattering, $\langle \cos \theta \rangle = 0$ and therefore $\ell_t = \ell_s$. In contrast, for pure forward scattering, $\langle \cos \theta \rangle = 1$ and hence $\ell_t = \infty$.

Let us now consider samples with a slab geometry, which extend infinitely in the transverse directions x and y and have a finite thickness L in the z -direction. In the case of $\ell_s \ll \ell_t \ll L$, the averaged statistics of light transport can be accurately described by the well-known and extensively studied diffusion theory [4]. For isotropic scattering without absorption and for a time-independent source S at position \mathbf{r}_0 , the intensity distribution $I(\mathbf{r})$ is given by the simple time-independent diffusion equation [3]

$$D\nabla^2 I(\mathbf{r}) + S(\mathbf{r}_0) = 0, \quad (2.2)$$

where D is the diffusion constant in the medium. However, diffusion theory is only valid in the bulk and not at the interfaces or close to the source. In that case, we have to use radiative transfer theory, which studies the transfer of electromagnetic radiation through the medium by taking into account emission, absorption and scattering processes [5].

If a plane wave is normal to the medium surface, the photons typically lose their direction after traveling a distance ℓ_t . In such circumstances, and only for normal incidence, light diffusion can be modeled as emanating from a diffuse source inside the medium at an injection depth of $z_i = \ell_t$ [6]. For a focused beam on the sample or any non-normal incident light, the injection depth is smaller and depends on the numerical aperture (NA) of the focusing lens [7, 8]. Additionally, the consideration of internal reflections at the surfaces of the medium modifies the boundary conditions such that the diffusive intensity drops to zero at so-called extrapolation lengths z_{e1} and z_{e2} away from the front and back surfaces of the sample, respectively [9, 10]. These lengths depend on the effective refractive indices of the medium and the surroundings [11]. The extrapolation lengths are important quantities because the ensemble averaged transmittance through the medium is given by [12]

$$\langle \mathcal{T} \rangle = \frac{z_i + z_{e1}}{L + z_{e1} + z_{e2}}. \quad (2.3)$$

The diffusion approximation is a powerful analysis tool because it can predict the statistics of scattered light waves without knowing the exact positions of the scatterers. However, its drawback is that it is only suitable for ensemble-

averaged analysis and fails to predict the transmission of a single instance of a single incident wave on a specific sample.

2.2 General approach

The general approach to solve a light scattering problem is to find the Green's function G given the permittivity $\varepsilon(r)$ and permeability $\mu(r)$ at all points in space. However, we note that most materials do not exhibit any magnetic response at optical frequencies, so we assume $\mu = \mu_0$ in the following. Starting from Maxwell's equations, light propagation in vacuum can be described by the electromagnetic wave equation [1]

$$\nabla^2 \mathbf{E} = \mu_0 \epsilon_0 \frac{\partial^2 \mathbf{E}}{\partial t^2}, \quad \nabla^2 \mathbf{B} = \mu_0 \epsilon_0 \frac{\partial^2 \mathbf{B}}{\partial t^2}, \quad (2.4)$$

where \mathbf{E} and \mathbf{B} are the electric and magnetic fields, and μ_0 and ϵ_0 are the vacuum permeability and permittivity respectively. From this wave equation, one can compute the Green's function in free space and subsequently derive the field of an oscillating electric dipole or of an arbitrary current distribution at every point in space.

The problem of finding the Green's function is more complicated for light scattering from a bunch of dipoles as the contribution of the fields emanating from the various dipoles has to be accounted for. Nonetheless, this is still possible to calculate by solving the Foldy-Lax equations [13, 14] as long as the number of scatterers is small and the dipole approximation is valid.

In an actual multiple scattering environment, the number of scatterers is typically more than a million, thus making it challenging to evaluate the Green's function of the system. Moreover, when the size of the scatterers is comparable to or larger than the wavelength of light, the dipole approximation does not hold. In this case, we treat the scatterers as Mie spheres and proceed by performing a series of multipole expansions [15, 16], thereby rapidly escalating the computational difficulty.

A second approach is to solve Maxwell's equations directly using a finite-difference time-domain (FDTD) method [17] which involves discretizing the time-dependent Maxwell's equations in space and time. However, this too is computationally restricted to a relatively small number of scatterers and hence cannot be used to simulate a large physical system. We note that similar considerations hold for other numerical methods.

Given that both approaches, viz., finding the system's Green's function and performing a FDTD simulation, are conceptually powerful but limited in scope, we require a more pragmatic approach to study a multiple scattering situa-

tion. One such possibility is to simplify the problem by treating the scattering medium as a black box and looking only in the far-field where we have complete knowledge of the electromagnetic fields [18]. To this end, we can define the transition matrix (or T-matrix) which relates incident waves to scattered fields. This can further be extended to include non-scattered fields by defining the scattering matrix (or S-matrix) that transforms all incoming waves to outgoing waves (both scattered and non-scattered). The scattering matrix has proven to be a useful tool to study multiple scattering media within the framework of random matrix theory (RMT) [19].

The scattering matrix is a matrix representation of the scattering operator, expressed in a suitable basis. Details on the choice of basis vectors are explained in Section 3.2. As the scattering matrix is conventionally defined in terms of an angular representation of fields, it is instructive to first decompose the incident and scattered field as a superposition of plane waves, which includes both propagating and evanescent ones [20]. For a scattering matrix measurement in the far field of the sample, there are by definition no evanescent waves whose amplitudes decay exponentially with increasing distance from the sample.

2.3 Relation between the S-matrix and the dyadic Green's function

We have two mathematical tools that describe light transport through a scattering medium – the Green's function and the S-matrix. In this section we aim to connect the definitions of the Green's function which is defined in a spatial basis and the S-matrix defined between spot wavefunctions on the sample surface. The electric Green's function gives the field response to a source term $\mathbf{J}(\mathbf{r})$,

$$\mathbf{E}(\mathbf{r}) = i\omega\mu \iiint d^3\mathbf{r}' \overline{\overline{\mathbf{G}}}(\mathbf{r}, \mathbf{r}') \cdot \mathbf{J}(\mathbf{r}'), \quad (2.5)$$

where $\mathbf{E}(\mathbf{r})$ is the electric field, ω is the angular frequency, μ is the magnetic permeability, and $\overline{\overline{\mathbf{G}}}(\mathbf{r}, \mathbf{r}')$ is the dyadic Green's function expressed by

$$\overline{\overline{\mathbf{G}}}(\mathbf{r}, \mathbf{r}') = \left[\overline{\overline{\mathbf{I}}} + \frac{1}{k^2} \nabla \nabla \right] g(\mathbf{r}, \mathbf{r}'). \quad (2.6)$$

Here $\overline{\overline{\mathbf{I}}}$ is the unit dyad and g is the scalar Green's function that satisfies the Helmholtz equation

$$(\nabla^2 + k^2) g(\mathbf{r}, \mathbf{r}') = -\delta(\mathbf{r} - \mathbf{r}'). \quad (2.7)$$

On the other hand, a scattering matrix links outgoing channel amplitudes $E_{\sigma'\mathbf{k}'}$ with wavevector \mathbf{k}' and polarization σ' to incident channel amplitudes $E_{\sigma\mathbf{k}}$ with wavevector \mathbf{k} and polarization σ [20–22],

$$E_{\sigma'\mathbf{k}'} = S_{\sigma\mathbf{k}\sigma'\mathbf{k}'} E_{\sigma\mathbf{k}}. \quad (2.8)$$

Since both tools describe the same phenomena, there must be an explicit relation that connects the two. We therefore first begin with a general dyadic Green's function formulation that gives the field flux at any point in space resulting from the incident field on a predefined surface. We then proceed to obtain the relation of the Green's dyad to the scattering matrix.

Given any closed surface S' enclosing all radiation sources, the following equations give the electric field \mathbf{E} and magnetic field \mathbf{H} at any point in space outside this surface,

$$\begin{aligned} \mathbf{E}(\mathbf{r}) = \iint_{S'} dS' \{ & i\omega\mu \overline{\overline{\mathbf{G}}}(\mathbf{r}, \mathbf{r}') \cdot [\hat{\mathbf{n}} \times \mathbf{H}(\mathbf{r}')] \\ & + (\nabla \times \overline{\overline{\mathbf{G}}}(\mathbf{r}, \mathbf{r}')) \cdot [\hat{\mathbf{n}} \times \mathbf{E}(\mathbf{r}')] \}, \end{aligned} \quad (2.9)$$

$$\begin{aligned} \mathbf{H}(\mathbf{r}) = \iint_{S'} dS' \{ & -i\omega\varepsilon \overline{\overline{\mathbf{G}}}(\mathbf{r}, \mathbf{r}') \cdot [\hat{\mathbf{n}} \times \mathbf{E}(\mathbf{r}')] \\ & + (\nabla \times \overline{\overline{\mathbf{G}}}(\mathbf{r}, \mathbf{r}')) \cdot [\hat{\mathbf{n}} \times \mathbf{H}(\mathbf{r}')] \}. \end{aligned} \quad (2.10)$$

This is a mathematical formulation of Huygens' principle but only taking into account propagation in the forward direction. The derivation of this result can be found in Chapter 5 of the book “Electromagnetic Wave Theory” by Jin Kong [23], which takes into account the vectorial nature of light and includes both the electric and magnetic components of the light field.

So far, we have defined the scattering matrix in a Fourier basis. Nevertheless, for the linear media that we assume here, any linear transformation of the angular basis is also a valid basis. One such transformation is the Fourier transform with which we convert the k -space basis to a real space basis. Mathematically, the Fourier transform of all monochromatic plane waves, including ones that do not satisfy the dispersion relation, is an Airy function in real space. In practice, such a transformation is performed with a lens or microscope objective, and hence we are limited by the diffraction limit of light [24]. More importantly, in the far field, we cannot include the off-shell with $k_x^2 + k_y^2 + k_z^2 > k_0^2(\text{NA})^2$, where k_0 is the wavevector in free space. The spatial basis thereby consists of a collection of diffraction limited spots.

Eqs. (2.9) and (2.10) give the electromagnetic field at a single observation

point in space due to fields on a closed surface containing radiating sources. A detector m in an experiment, e.g., a pixel, is not a single point but occupies a finite area S_m . Nonetheless, if we assume the detector m to be small enough so that the field is more or less uniform over its surface S_m , we can consider the field at the detector to be the field at the position $\mathbf{r} = \mathbf{r}_m$. Consequently, the electric and magnetic fields at detector m caused by a diffracted limited input spot at source n are given by

$$\begin{aligned} \mathbf{E}_m = \iint_{S'} dS' \{ & i\omega\mu \bar{\bar{G}}(\mathbf{r}_m, \mathbf{r}') \cdot [\hat{n} \times \mathbf{H}_n(\mathbf{r}')] \\ & + (\nabla \times \bar{\bar{G}}(\mathbf{r}_m, \mathbf{r}')) \cdot [\hat{n} \times \mathbf{E}_n(\mathbf{r}')] \}, \end{aligned} \quad (2.11)$$

$$\begin{aligned} \mathbf{H}_m = \iint_{S'} dS' \{ & -i\omega\varepsilon \bar{\bar{G}}(\mathbf{r}_m, \mathbf{r}') \cdot [\hat{n} \times \mathbf{E}_n(\mathbf{r}')] \\ & + (\nabla \times \bar{\bar{G}}(\mathbf{r}_m, \mathbf{r}')) \cdot [\hat{n} \times \mathbf{H}_n(\mathbf{r}')] \}. \end{aligned} \quad (2.12)$$

In the above expressions, the only contribution from the surface S' is over the diffraction limited spot at source n . The rest of S' does not contribute to the integral because of the absence of any electromagnetic field.

Since a light field consists of two orthogonal polarization components, we can treat each of them separately. Considering only one polarization component, we can write the electric field as $\mathbf{E}_n(\mathbf{r}') = E_n^{\text{in}} \tilde{\mathbf{E}}_n(\mathbf{r}')$, where E_n^{in} is a normalization constant ($\sum_n |E_n^{\text{in}}|^2 = 1$) that represents the contribution of the n^{th} input spot. If only source n is illuminated, $E_n^{\text{in}} = 1$. Using the relation $\nabla \times \mathbf{E}(\mathbf{r}) = i\omega\mu\mathbf{H}(\mathbf{r})$, eq. (2.11) can be finally expressed as

$$\begin{aligned} \mathbf{E}_m = E_n^{\text{in}} \iint_{S'} dS' \{ & \bar{\bar{G}}(\mathbf{r}_m, \mathbf{r}') \cdot [\hat{n} \times (\nabla' \times \tilde{\mathbf{E}}_n(\mathbf{r}'))] \\ & + (\nabla \times \bar{\bar{G}}(\mathbf{r}_m, \mathbf{r}')) \cdot [\hat{n} \times \tilde{\mathbf{E}}_n(\mathbf{r}')] \}, \end{aligned} \quad (2.13)$$

where ∇' is the spatial derivative with respect to the coordinate \mathbf{r}' .

The complex element s_{mn} of the scattering matrix linking the flux of the n^{th} input mode to that of the m^{th} output mode can be calculated as

$$E_m^{\text{out}} = s_{mn} E_n^{\text{in}}. \quad (2.14)$$

Comparing then eq. (2.13) with eq. (2.14) for a single illuminated spot n , we conclude that the scattering matrix elements s_{mn} can be expressed as a function

of the dyadic Green's function with the following expression:

$$s_{mn} = \iint_{S'} dS' \{ \overline{\overline{G}}(\mathbf{r}_m, \mathbf{r}') \cdot [\hat{n} \times (\nabla' \times \tilde{\mathbf{E}}_n(\mathbf{r}'))] + (\nabla \times \overline{\overline{G}}(\mathbf{r}_m, \mathbf{r}')) \cdot [\hat{n} \times \tilde{\mathbf{E}}_n(\mathbf{r}')] \}. \quad (2.15)$$

From the above expression, we see that it is possible to find the sampled scattering matrix from knowing the complete Green's dyad, but not vice versa. The reason for this is that while $\overline{\overline{G}}$ contains near-field terms and is in principle defined for all points in space, the scattering matrix is defined in the far field and is band-limited because it is calculated by integrating over band-limited basis vectors $\tilde{\mathbf{E}}_n$. This is true even in the case of a zero-thickness medium, where the incident and transmitted fields lie on the same plane. For such a sample, the Green's function $\overline{\overline{G}}$ contains near-field terms and diverges. However, the S-matrix is free of this problem and more straightforward to compute.

For situations where the input modes are on one side of the sample and the output modes are on the other, the matrix elements s_{mn} are denoted as t_{mn} and represent the **transmission matrix** of the sample, which is a subset of the scattering matrix. In essence, we have provided a rigorous definition of the transmission matrix by connecting it to the Green's dyad which contains all information with the far- and near-field. However, finding the Green's dyad for a random medium in general requires near-field probes and is beyond the scope of this thesis.

2.4 Transmission channels

A convenient and popular method to analyze transmission matrices of clear (Chapters 3, 4) and scattering (Chapters 5, 6) samples is to decompose them into transmission channels. To understand the concept of transmission channels of a scattering medium and its relation to the transmission matrix [25], let us first begin with a simple example from the radio frequency (RF) domain. We assume we have an input array of several “transmission” antennas and an output array of many “receiver” antennas. Such a system is known as MIMO (multiple-input-multiple-output) and is a well known configuration in the field of wireless communication [26]. Other names by which this system is referred to in literature are “MIMO-MISO”, “transmit diversity”, “beamforming” and “phased array” [27].

Let us assume that we have the same number M of input and output antennas. We can represent the total transmitted signal as the vector $\mathbf{s} = (s_1, s_2, \dots, s_M)$ and the total received signal as the vector $\mathbf{y} = (y_1, y_2, \dots, y_M)$,

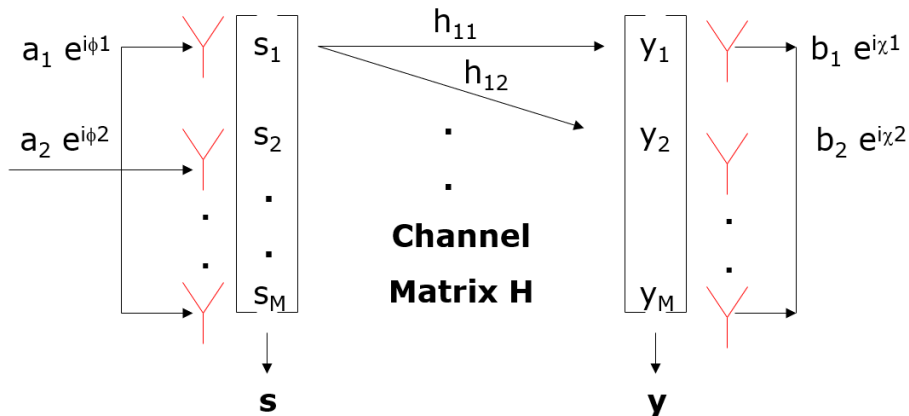


Figure 2.1: Sketch of a MIMO system. The input signal is driven with signal \mathbf{a} . The signal is then transmitted from the “transmit” antennas \mathbf{s} to the “receive” antennas \mathbf{y} . The channel matrix H describes this process. The received signal is then recombined with the signal \mathbf{b} . Figure adapted from [28].

where s_i is the transmitted signal from the i^{th} “transmit” antenna and y_j is the received signal from the j^{th} “receive” antenna. If the transmission coefficient of the signal relating s_i to y_j is given by the matrix element h_{ij} of the channel matrix H , then the situation can be mathematically described as [28]

$$\mathbf{y} = H\mathbf{s} + \mathbf{n}, \quad (2.16)$$

with \mathbf{n} a noise vector. For the moment, we assume that we are in the ideal case of a noise-free environment so that we can set $\mathbf{n} = 0$.

The optimal way of maximizing data transfer from the input antennas to the receiving antennas is through the transmission channels which, by definition, are communication paths that are orthogonal [29–31]. Since H is a matrix which depends on the environment, it is hard to modify its elements. However, by driving the “transmit” antennas and linearly combining the signal of “receive” antennas, one can optimize the amount of information sent across. The optimal channels are found by driving the antennas with a drive signal $\mathbf{a} = (a_1 e^{i\phi_1}, a_2 e^{i\phi_2}, \dots, a_M e^{i\phi_M})$ and recombining the received signal with $\mathbf{b} = (b_1 e^{i\chi_1}, b_2 e^{i\chi_2}, \dots, b_M e^{i\chi_M})$, generating the strongest total signal subject to power normalization ($a^2 = b^2 = 1$). A graphical representation of such an optimized MIMO system is illustrated in Fig. 2.1.

To know how to construct the drive and recombine signals, let us look at the problem again in terms of matrices. According to linear algebra, any complex

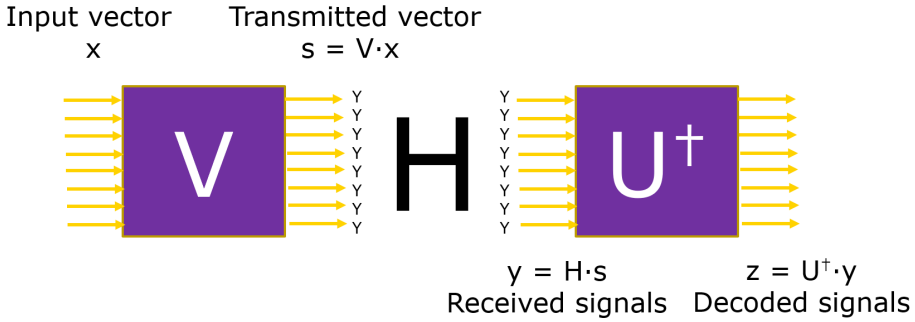


Figure 2.2: Optimized MIMO system described with matrices. An input vector \mathbf{x} is first encoded with the matrix \mathbf{V} before passing through the channel matrix \mathbf{H} . The received signal is then decoded with the matrix \mathbf{U}^\dagger to yield the final signal \mathbf{z} .

matrix \mathbf{H} can be factorized as

$$\mathbf{H} = \mathbf{U}\mathbf{D}\mathbf{V}^\dagger, \quad (2.17)$$

where \mathbf{U} and \mathbf{V} are complex unitary matrices, i.e., $\mathbf{U}^\dagger = \mathbf{U}^{-1}$ and $\mathbf{V}^\dagger = \mathbf{V}^{-1}$, and \mathbf{D} is a real and positive diagonal matrix. This factorization is known as singular value decomposition and the diagonal elements s of \mathbf{D} are called the singular values of the matrix \mathbf{H} .

Now if the signals are driven with the encoding matrix \mathbf{V} and recombined with the decoding matrix \mathbf{U}^\dagger , then for an input vector \mathbf{x} , the configuration can be represented as in Fig. 2.2. The transmitted signal is $\mathbf{s} = \mathbf{V} \cdot \mathbf{x}$, the received signal is $\mathbf{y} = \mathbf{H} \cdot \mathbf{s}$, and the final decoded signal is $\mathbf{z} = \mathbf{U}^\dagger \cdot \mathbf{y}$. Combining these relations, and remembering that \mathbf{H} can be factorized as in eq. (2.17) and that \mathbf{U} and \mathbf{V} are unitary matrices, we obtain a final decoded signal

$$\mathbf{z} = \mathbf{U}^\dagger \mathbf{H} \mathbf{V} \cdot \mathbf{x} = \mathbf{U}^\dagger \mathbf{U} \mathbf{D} \mathbf{V}^\dagger \mathbf{V} \cdot \mathbf{x} = \mathbf{D} \cdot \mathbf{x}. \quad (2.18)$$

Using \mathbf{V} and \mathbf{U} as the encoding and decoding matrices, we see that the decoded signal \mathbf{z} is simply the product of a diagonal matrix \mathbf{D} with the raw input signal \mathbf{x} . We thus have M transmission channels without cross-talk with transmission s_i , with s_i the diagonal elements of \mathbf{D} . Effectively, the singular values s of the matrix \mathbf{H} represent the transmission coefficients of the individual channels. The right singular vectors \mathbf{v} (rows of \mathbf{V}^\dagger /columns of \mathbf{V}), which are the eigenvectors of $\mathbf{H}^\dagger \mathbf{H}$ with eigenvalues s^2 , are the transmission channels of \mathbf{H} . Conversely, the transmission channels to go from right to left via the matrix \mathbf{H}^\dagger are the left singular vectors \mathbf{u} (columns of \mathbf{U}) which are the eigenvectors of $\mathbf{H} \mathbf{H}^\dagger$ with the

same eigenvalues s^2 .

We can implement the same concept of transmission channels to scattering optics by making an analogy between the RF antennas and the optical modes of a scattering sample. In a slab geometry, the number of modes over an area A of a strongly scattering sample is given by $2\pi A/\lambda^2$, where λ is the wavelength of light [32, 33]. In that case, optical transmission channels are cross-talk free “paths” from the input modes to the output modes of the sample [19, 34, 35]. If we send a channel \mathbf{v}_i through a sample with transmission matrix T , the transmitted intensity I_{out} is

$$I_{out} = E_{out}^\dagger E_{out} = (T\mathbf{v}_i)^\dagger (T\mathbf{v}_i) = \mathbf{v}_i^\dagger T^\dagger T \mathbf{v}_i = \mathbf{v}_i^\dagger s_i^2 \mathbf{v}_i = s_i^2 I_{in}. \quad (2.19)$$

Hence we see that the channel \mathbf{v}_i has a transmittance s_i^2 . A normalized transmittance of 1 corresponds to open channels, which transport all the incident light through the scattering medium [36, 37]. On the other hand, a transmittance of 0 is associated to closed channels, which completely reflect the incident light and do not let any of it pass through the sample. Intermediate transmittances represent partially open and partially closed channels.

2.4.1 Marchenko-Pastur and DMPK distributions

To understand light transport in a diffuse sample and to exploit it for imaging purposes, we are interested to model the distribution of the transmission channels inside random scattering media which can be represented by random matrices. The simplest model is a random uncorrelated matrix with independent elements from an uniform random distribution. The normalized singular values s of such a matrix follow the Marchenko-Pastur law derived from random matrix theory [38], and their probability distribution is given by

$$P(s) = \frac{\gamma \sqrt{s^2 - s_{\min}^2} \sqrt{s_{\max}^2 - s^2}}{\pi s}, \quad (2.20)$$

where $s_{\min} = 1 - \sqrt{1/\gamma}$ and $s_{\max} = 1 + \sqrt{1/\gamma}$, and γ is the aspect ratio (number of rows m divided by number of columns n , with $m \geq n$) of the matrix. Here, s is normalized to the root mean square (RMS) value. The Marchenko-Pastur probability distribution is plotted in Fig. 2.3 for different values of γ .

A special case of the Marchenko-Pastur law is for a square matrix ($\gamma = 1$), when eq. (2.20) reduces to

$$P(s) = \frac{1}{\pi} \sqrt{4 - s^2}. \quad (2.21)$$

This well-known case is called the quarter circle law since the distribution re-

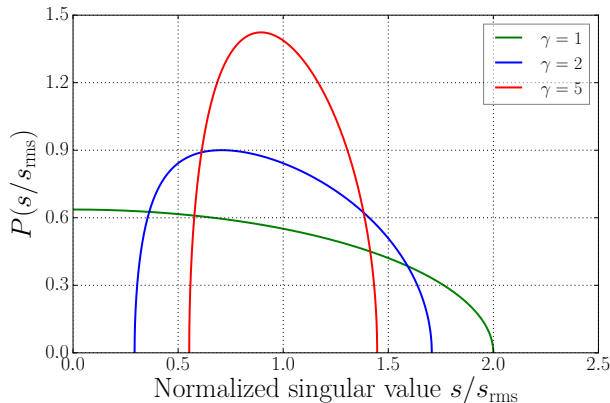


Figure 2.3: Marchenko-Pastur distribution (eq. (2.20)) of singular values s for a random matrix with an aspect ratio γ . The singular values are normalized with respect to the root mean square (RMS) value.

sembles a quarter circle. Therefore, conversely, if the singular value histogram of a square matrix does *not* follow the quarter circle law, then the matrix elements are *not* independent identically distributed random variables.

However, in an actual random scattering sample, the elements of the scattering matrix are not completely uncorrelated. The reason for this can succinctly be explained by energy conservation. If one matrix element changes, there must be at least another element that simultaneously changes to satisfy the unitarity of the S-matrix. Since the TM is a smaller fraction of the S-matrix, it reflects some of the correlations present in the S-matrix and it has been shown that the singular value distribution of the TM of a disordered sample does not follow the Marchenko-Pastur law. The distribution of the singular values instead follows DMPK statistics, named after scientists who contributed significantly to its development, viz., Dorokhov, Mello, Pereyra and Kumar [39–41]. They obtained the distribution by considering the propagation of the field through the scattering medium in a succession of thin weakly scattering layers. This distribution is dependent on the number of modes N , the medium thickness L and the transport mean free path ℓ_t . Here we assume isotropic scattering so that the transport mean free path ℓ_t is equal to the scattering mean free path ℓ_s . The average transmission through the medium is roughly $\langle \mathcal{T} \rangle = \ell_t/L$ [18]. The DMPK probability function for the transmittance s^2 of the channels, valid only in disordered media, is expressed as [39, 42, 43]

$$P(s^2) = \frac{N\ell_t}{2L} \frac{1}{s^2\sqrt{1-s^2}} \quad (2.22)$$

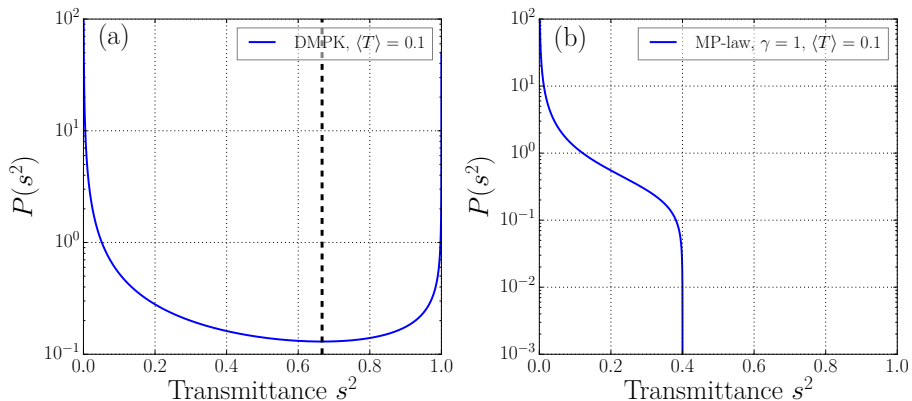


Figure 2.4: The probability distribution of the transmittance s^2 of the channels for a matrix obeying (a) DMPK statistics (eq. (2.22) with $\langle \mathcal{T} \rangle = 0.1$ and $N = 1$) and (b) Marchenko-Pastur statistics ($\gamma = 1$ and $\langle \mathcal{T} \rangle = 0.1$). The dashed vertical line in (a) at $s^2 = 2/3$ indicates the transmittance at which the DMPK function exhibits a minimum. The values on the y -axes are on a logarithmic scale.

and plotted in Fig. 2.4(a) for $\langle \mathcal{T} \rangle = 0.1$. Unlike Fig. 2.3, the transmittance is in absolute scale and not normalized to the RMS value. In the diffusive regime, where $\ell_t \ll L \ll \xi$ (localization length), the curve begins for a minimum transmittance of $s_{\min}^2 = \cosh^{-2}(L/\ell_t) \approx 4 \exp(-2L/\ell_t)$. Since the divergence at $s^2 = 1$ is integrable, this makes the function well defined and normalized such that $\int_{s_{\min}^2}^1 P(s^2) ds^2 = N$.

The distribution is bimodal, with a high probability of finding closed ($s^2 \approx 0$) and open ($s^2 \approx 1$) channels. It is however asymmetric, with a larger number of closed channels than open channels ($s^2 \approx 1$). Interestingly, there is a relatively small probability to find partially transmitting channels in the intermediate region. The minimum of the function occurs exactly at $s^2 = 2/3$ (see Fig. 2.4(a)), and it is therefore reasonable to call channels highly transmitting for transmittances greater than this characteristic dip. The outstanding feature is that there always exist a number of these highly transmitting eigenchannels ($s^2 \geq 2/3$) in a strongly scattering medium in the diffusive regime. Consequently, there would be almost no loss of transmitted intensity if the incident field couples exclusively to these open channels. Conversely, all the incident light will be diffusively reflected if it couples solely to closed channels.

For comparison, the equivalent Marchenko-Pastur transmittance distribution for a square matrix with the same average transmission $\langle \mathcal{T} \rangle = 0.1$ is plotted in Fig. 2.4(b). We notice that the highest transmittance exhibited by such a

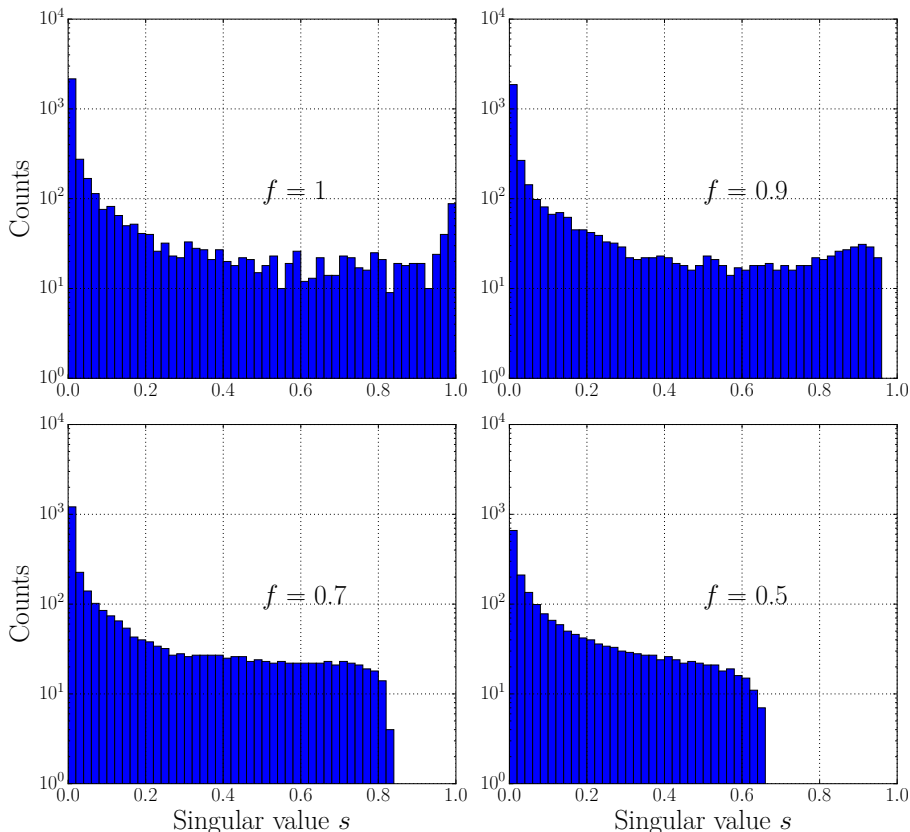


Figure 2.5: Singular value histograms for different fractions f of a DMPK matrix of size 4000×4000 with an average transmission $\langle \mathcal{T} \rangle = 0.1$.

matrix is 0.4, which is in stark contrast to the fully transmitting channels of the DMPK matrix. This shows that mesoscopic correlations are responsible for an increased transmission through scattering media.

Unfortunately, unlike the regime of microwaves [44] and ultrasound [45], it is experimentally impossible to measure the complete TM in free space optics because of the limited numerical aperture, limited field of view and an escape of energy to the sides parallel to the sample surface. It has been shown that the distribution of singular values is sensitive to the measured fraction of the complete TM [46, 47]. To demonstrate the effect of a partial TM on the statistics, we generate a large DMPK matrix and then filter it down to a smaller size and look at the corresponding singular value statistics. To numerically construct a $M \times M$ DMPK matrix with average transmittance $\langle \mathcal{T} \rangle$, we first generate a list of M singular values with a DMPK distribution ranging from $\cosh^{-1}(\langle \mathcal{T} \rangle)$ to 1.

We then create a $M \times M$ diagonal matrix D with the list of singular values as the diagonal elements. We find the final matrix with DMPK statistics T_{DMPK} by calculating $T_{\text{DMPK}} = UDV^\dagger$, where U and V^\dagger are $M \times M$ complex unitary matrices obtained from the singular value decomposition of a $M \times M$ random complex Gaussian matrix. We subsequently reduce T_{DMPK} to a smaller size by randomly eliminating the same number of rows and columns.

Fig. 2.5 shows the singular value histograms for different fractions f of an original DMPK matrix of size 4000×4000 with an average transmission $\langle \mathcal{T} \rangle = 0.1$. We observe that even for a fraction as high as 0.9, the peak at 1 vanishes. This proves that eliminating 10% of a DMPK matrix is sufficient to miss out on detecting fully transmitting open channels. The maximum transmission only reduces further for smaller TM fractions of 70% and 50% as the highest value drops to about 0.65, following approximately $s_{\text{max}}^2 \approx f$ [48]. Conversely, the shape of the curve at low singular values remains more or less unaffected although the count drops with matrix truncation. We see therefore that the statistics of a partial matrix differ greatly from the bimodal distribution. This makes it an interesting and ongoing study to investigate to what extent highly transmitting open channels can be found and coupled to in such open systems experimentally [36, 49–52].

Bibliography

- [1] J. D. Jackson, *Classical electrodynamics* (Wiley, New York, NY, 1999), 3rd ed.
- [2] G. H. Weiss, J. M. Porrà, and J. Masoliver, “The continuous-time random walk description of photon motion in an isotropic medium,” *Optics Communications* **146**, 268 – 276 (1998).
- [3] M. C. W. van Rossum and T. M. Nieuwenhuizen, “Multiple scattering of classical waves: microscopy, mesoscopy, and diffusion,” *Rev. Mod. Phys.* **71**, 313–371 (1999).
- [4] B. W. P. Steven L. Jacques, “Tutorial on diffuse light transport,” *Journal of Biomedical Optics* **13**, 1 – 19 – 19 (2008).
- [5] S. Chandrasekhar, *Radiative Transfer*, Dover Books on Intermediate and Advanced Mathematics (Dover Publications, 1960).
- [6] E. Akkermans, P. E. Wolf, and R. Maynard, “Coherent backscattering of light by disordered media: Analysis of the peak line shape,” *Phys. Rev. Lett.* **56**, 1471–1474 (1986).
- [7] J. H. Li, A. A. Lisiansky, T. D. Cheung, D. Livdan, and A. Z. Genack, “Transmission and surface intensity profiles in random media,” *Europhysics Letters (EPL)* **22**, 675–680 (1993).
- [8] D. Akbulut, “Measurements of strong correlations in the transport of light through strongly scattering materials,” Ph.D. thesis, University of Twente (2013).
- [9] A. Lagendijk, R. Vreeker, and P. D. Vries, “Influence of internal reflection on diffusive transport in strongly scattering media,” *Physics Letters A* **136**, 81 – 88 (1989).
- [10] J. X. Zhu, D. J. Pine, and D. A. Weitz, “Internal reflection of diffusive light in random media,” *Phys. Rev. A* **44**, 3948–3959 (1991).
- [11] M. U. Vera and D. J. Durian, “Angular distribution of diffusely transmitted light,” *Phys. Rev. E* **53**, 3215–3224 (1996).
- [12] J. G. Rivas, R. Sprik, C. M. Soukoulis, K. Busch, and A. Lagendijk, “Optical transmission through strong scattering and highly polydisperse media,” *Europhysics Letters (EPL)* **48**, 22–28 (1999).
- [13] L. L. Foldy, “The multiple scattering of waves. I. General theory of isotropic scattering by randomly distributed scatterers,” *Phys. Rev.* **67**, 107–119 (1945).
- [14] M. Lax, “Multiple scattering of waves. II. The effective field in dense systems,” *Phys. Rev.* **85**, 621–629 (1952).
- [15] G. Mie, “Beiträge zur Optik trüber Medien, speziell kolloidaler Metallösungen,” *Annalen der Physik* **330**, 377–445 (1908).
- [16] J. A. Stratton, *Electromagnetic theory* (John Wiley & Sons, 2007).

- [17] Kane Yee, “Numerical solution of initial boundary value problems involving Maxwell’s equations in isotropic media,” *IEEE Transactions on Antennas and Propagation* **14**, 302–307 (1966).
- [18] E. Akkermans and G. Montambaux, *Mesoscopic Physics of Electrons and Photons* (Cambridge University Press, 2007).
- [19] C. W. J. Beenakker, “Random-matrix theory of quantum transport,” *Rev. Mod. Phys.* **69**, 731–808 (1997).
- [20] E. Wolf, “A scalar representation of electromagnetic fields: II,” *Proceedings of the Physical Society* **74**, 269–280 (1959).
- [21] M. Nieto-Vesperinas, *Scattering and Diffraction in Physical Optics*, 2nd Edition (World Scientific Publishing Company, 2006).
- [22] M. Nieto-Vesperinas and E. Wolf, “Generalized Stokes reciprocity relations for scattering from dielectric objects of arbitrary shape,” *J. Opt. Soc. Am. A* **3**, 2038–2046 (1986).
- [23] J. Kong, *Electromagnetic Wave Theory*, A Wiley-Interscience publication (Wiley, 1986).
- [24] J. Goodman, *Introduction to Fourier Optics*, McGraw-Hill Series in Electrical and Computer Engineering: Communications and Signal Processing (McGraw-Hill, 1996).
- [25] D. A. B. Miller, “Waves, modes, communications, and optics: a tutorial,” *Adv. Opt. Photon.* **11**, 679–825 (2019).
- [26] G. J. Foschini, “Layered space-time architecture for wireless communication in a fading environment when using multi-element antennas,” *Bell Labs Technical Journal* **1**, 41–59 (1996).
- [27] A. J. Paulraj, D. A. Gore, R. U. Nabar, and H. Bolcskei, “An overview of MIMO communications - a key to gigabit wireless,” *Proceedings of the IEEE* **92**, 198–218 (2004).
- [28] H. Ganapathy, “Multiple input multiple output (MIMO) systems: Basic principles, algorithms and networking applications,” (2005).
- [29] A. Kaye and D. George, “Transmission of multiplexed PAM signals over multiple channel and diversity systems,” *IEEE Transactions on Communication Technology* **18**, 520–526 (1970).
- [30] L. H. Brandenburg and A. D. Wyner, “Capacity of the Gaussian channel with memory: The multivariate case,” *The Bell System Technical Journal* **53**, 745–778 (1974).
- [31] W. van Etten, “Maximum likelihood receiver for multiple channel transmission systems,” *IEEE Transactions on Communications* **24**, 276–283 (1976).
- [32] B. Saleh and M. Teich, *Fundamentals of Photonics*, Wiley Series in Pure and Applied Optics (Wiley, 2007).
- [33] A. Mosk, A. Lagendijk, G. Lerosey, and M. Fink, “Controlling waves in

- space and time for imaging and focusing in complex media,” *Nature photonics* **6**, 283–292 (2012).
- [34] J. Pendry, A. MacKinnon, and A. Pretre, “Maximal fluctuations — a new phenomenon in disordered systems,” *Physica A: Statistical Mechanics and its Applications* **168**, 400–407 (1990).
- [35] E. N. Economou and C. M. Soukoulis, “Static conductance and scaling theory of localization in one dimension,” *Phys. Rev. Lett.* **46**, 618–621 (1981).
- [36] I. M. Vellekoop and A. P. Mosk, “Universal optimal transmission of light through disordered materials,” *Phys. Rev. Lett.* **101**, 120601 (2008).
- [37] J. Pendry, “Light finds a way through the maze,” *Physics* **1**, 20 (2008).
- [38] V. A. Marčenko and L. A. Pastur, “Distribution of eigenvalues for some sets of random matrices,” *Mathematics of the USSR-Sbornik* **1**, 457–483 (1967).
- [39] O. Dorokhov, “On the coexistence of localized and extended electronic states in the metallic phase,” *Solid State Communications* **51**, 381 – 384 (1984).
- [40] P. Mello, P. Pereyra, and N. Kumar, “Macroscopic approach to multichannel disordered conductors,” *Annals of Physics* **181**, 290 – 317 (1988).
- [41] S. Rotter and S. Gigan, “Light fields in complex media: Mesoscopic scattering meets wave control,” *Rev. Mod. Phys.* **89**, 015005 (2017).
- [42] Y. Imry, “Active transmission channels and universal conductance fluctuations,” *Europhysics Letters (EPL)* **1**, 249–256 (1986).
- [43] J. B. Pendry, A. MacKinnon, and P. J. Roberts, “Universality classes and fluctuations in disordered systems,” *Proceedings of the Royal Society of London. Series A: Mathematical and Physical Sciences* **437**, 67–83 (1992).
- [44] Z. Shi and A. Z. Genack, “Transmission eigenvalues and the bare conductance in the crossover to Anderson localization,” *Phys. Rev. Lett.* **108**, 043901 (2012).
- [45] A. Aubry and A. Derode, “Random matrix theory applied to acoustic backscattering and imaging in complex media,” *Phys. Rev. Lett.* **102**, 084301 (2009).
- [46] A. Goetschy and A. D. Stone, “Filtering random matrices: The effect of incomplete channel control in multiple scattering,” *Phys. Rev. Lett.* **111**, 063901 (2013).
- [47] H. Yu, T. R. Hillman, W. Choi, J. O. Lee, M. S. Feld, R. R. Dasari, and Y. Park, “Measuring large optical transmission matrices of disordered media,” *Phys. Rev. Lett.* **111**, 153902 (2013).
- [48] S. A. Goorden, “Reversible scattering of light exploited for quantum-secure authentication,” Ph.D. thesis, University of Twente (2015).

- [49] W. Choi, A. P. Mosk, Q.-H. Park, and W. Choi, “Transmission eigenchannels in a disordered medium,” *Phys. Rev. B* **83**, 134207 (2011).
- [50] M. Kim, Y. Choi, C. Yoon, W. Choi, J. Kim, Q.-H. Park, and W. Choi, “Maximal energy transport through disordered media with the implementation of transmission eigenchannels,” *Nature Photonics* **6**, 581 (2012).
- [51] S. M. Popoff, A. Goetschy, S. F. Liew, A. D. Stone, and H. Cao, “Coherent control of total transmission of light through disordered media,” *Phys. Rev. Lett.* **112**, 133903 (2014).
- [52] H. Yilmaz, C. W. Hsu, A. Yamilov, and H. Cao, “Transverse localization of transmission eigenchannels,” *Nature Photonics* **13**, 352–358 (2019).

3 Optical transmission matrix measurement sampled on a dense hexagonal lattice¹

3.1 Introduction

In wave physics, the scattering operator of a sample links the incident waves to the ballistic and scattered outgoing waves [1, 2]. By definition it considers only waves that propagate to, or from, the far field. If the sample has a slab geometry, the part of the scattering operator that relates the incident field to the transmitted one is called the transmission operator (TO). By choosing a basis of incident and outgoing modes one can construct a matrix representation of the transmission operator known as the transmission matrix (TM) [3–8]. A TM measurement that gives full information on the transmission operator requires a basis that spans all incident and outgoing modes of the wave field. The number of independent modes N_s incident on an area A on the surface of a slab is equal to the number of modes in a waveguide of the same area, $N_s = 2\pi A/\lambda^2$ [5, 9], where λ is the wavelength. It is however not straightforward to find an orthogonal and complete basis on a finite sample in free space.

One of the reasons to measure the TM is to explore the distribution and properties of its singular values which, if the TM accurately represents the TO, correspond to the transmission eigenchannels of the sample. These channels are useful in imaging and communication [5, 10] and are an important building block of quantum transport theory in scattering samples [11–15]. The predicted theoretical distribution of the singular values in a multiple scattering waveguide is a bimodal distribution known as the Dorokhov-Mello-Pereyra-Kumar curve [16, 17] and the properties of transmission channels are a subject of recent intense research [7, 10, 18–32]. In an open optical system, the finite field of view and finite numerical aperture of the optics and the escape of energy parallel to the surface of the sample make it impossible to measure the complete matrix.

¹This chapter has been accepted for publication in OSA Continuum as: P. Pai, J. Bosch and A. P. Mosk, **Vol. 3 (2020)**. arXiv:1912.00933

The appendix contains supplementary information not included in the paper. It elaborates on experimental details and discusses statistics of the eigenvalues of the transmission matrix.

The statistics of a partial transmission matrix has been shown to differ strongly from that of a full one [33,34]. This is less of a problem for guided waves such as microwaves [19,20], ultrasound [35,36] and elastic waves [21] where it is easier to access a large fraction of the scattered field. It is an ongoing challenge to accurately measure the largest possible fraction of the TM of a three-dimensional sample in an open optical system [8].

Popoff and coauthors published the first measurements of the optical TM of a multiple scattering sample, using a spatial light modulator (SLM) to project light fields on a Hadamard basis and with an unmodulated part of the light as the phase reference [4]. They demonstrated transmitting predetermined focused spots and images [37]. The low sampling density in their experiment precluded the observation of open channels or other mesoscopic correlations. Other methods employed a basis of spots in real or Fourier space, using a scan-mirror to enhance measurement speed as well as a separate reference arm to retrieve the transmitted field with a single shot method [27,34,38–40]. Interferometric methods are sensitive to phase drifts, and to this end it has been shown that the TM can also be measured without a reference beam [41]. However, this method requires a much larger number of measurements than the number of independent modes. Optical TM measurements close to the critical sampling density have been performed by scanning the beam on a square lattice [27,31,32,34,42]. When approaching the critical sampling density, where the number of sampled incident modes equals the total number of linearly independent modes N_s , bandwidth-limited input spots become correlated as the nearest neighbor spot wavefunctions (usually Airy disks) show increasing overlap, leading to distorted statistics of the TM. The amount of overlap depends on the lattice configuration.

In this chapter, we demonstrate TM measurements using a hexagonal lattice of Airy disks spaced at the Rayleigh criterion, where the field overlap between neighboring spots is exactly zero and only small overlap exists between more distant spots. We note that measurements on an undersampled hexagonal grid far from the Rayleigh criterion have been demonstrated in Ref. [43]. We show that the hexagonal grid leads to a better representation of the statistics of the TM than square-grid sampling only close to the Rayleigh criterion. As in [27,34], we measure a polarization-complete TM. The spots are scanned in an outward hexagonal spiral which helps determine efficiently the point after which the beam escapes the microscope objective’s field of view or numerical aperture. We describe the experimental method and data analysis and perform a measurement of the TM of a zero-thickness medium, i.e., a clear medium where the focal planes of the input and output optics are the same. In this case the incident and transmitted fields are identical and the transmission operator

is diagonal. Crucially, the orthogonality of the basis determines whether the transmission matrix is also diagonal, and we can check directly how the statistics of the TM are influenced by the sampling lattice.

3.2 Sampling the transmission matrix

Theoretically, the scattering matrix is expressed using a basis set of orthogonal flux-normalized far-field modes. We have natural basis sets in the case of a sample in a waveguide (flux-normalized waveguide modes) as well as in the case of a small scatterer in free space (flux-normalized partial waves) [10]. For a slab-type sample in free space the S-matrix is conventionally written as $S_{\sigma\mathbf{k}\sigma'\mathbf{k}'}$, where \mathbf{k} and \mathbf{k}' are the wavevectors and σ and σ' the polarizations corresponding to the incoming and scattered waves respectively [1, 44, 45]. The scattering matrix element $S_{\sigma\mathbf{k}\sigma'\mathbf{k}'}$ represents the amplitude scattered into the flux-normalized channel \mathbf{k}' with polarization σ' due to an incident flux with normalized amplitude in channel \mathbf{k} and polarization σ . If k and k' are on opposite sides of a slab-type sample we speak of a transmission matrix element. On a finite sample, infinite plane waves are not a useful basis set and one has to resort to modes that are confined both in real space and Fourier space, such as diffraction limited spots.

Here we choose a real-space basis of diffraction limited spots that are generated by our microscope objective. We note that the TM can equivalently be measured in a k -space basis, where similar considerations apply. An objective fulfilling the Abbe sine condition [46] filled with a uniform collimated beam produces an Airy disk in the focal plane, which is a band-limited field defined by the circular shape of the pupil. The optimal sampling configuration for band-limited signals by a periodic lattice on a 2D plane is a hexagonal lattice (also known as a triangular lattice) [47]. If the density of sampling points is at least the critical or Nyquist density, corresponding to one sampling point per mode, the entire signal can be reconstructed from the sampled points.

On a square grid with a lattice constant a , as shown on the left image in Fig. 3.1, the diagonal neighbors have a separation of $a\sqrt{2}$. Consequently, the transmitted fields from two spots separated by a or by $a\sqrt{2}$ yield different amounts of overlap. However, in our hexagonal sampling grid as illustrated on the right of Fig. 3.1, the six nearest neighbors are all at a distance a , while the six second neighbors are at a distance $a\sqrt{3}$. Critical sampling (within the band limit imposed by the NA) is achieved for the square lattice at

$$a_{sq}^2 = \frac{\lambda^2}{\pi} (\text{NA})^{-2}, \quad (3.1)$$

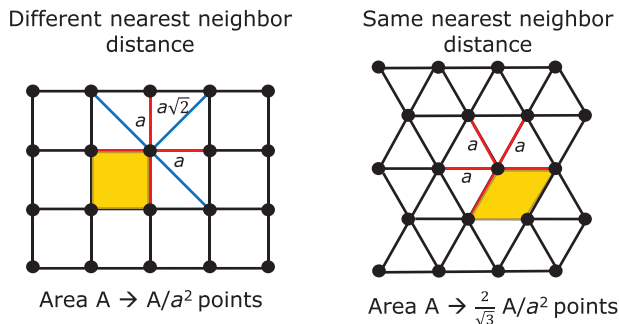


Figure 3.1: Comparison between sampling on a square (left) and hexagonal (right) lattice. The lattice constant is a and the shaded area represents the unit cell.

and for the hexagonal lattice at

$$a_{hex}^2 = \frac{2}{\sqrt{3}} \frac{\lambda^2}{\pi} (\text{NA})^{-2} \approx 1.15 \frac{\lambda^2}{\pi} (\text{NA})^{-2}. \quad (3.2)$$

Remarkably, near critical sampling the nearest neighbor Airy spots on the hexagonal grid are almost exactly at the Rayleigh criterion

$$a_{hex} = 0.994 a_{Ray} \quad \text{with} \quad a_{Ray} = \frac{z_1 \lambda}{2\pi} (\text{NA})^{-1}, \quad (3.3)$$

where a_{Ray} is the Rayleigh distance at which the maximum of one spot coincides with the first zero of its neighbor and the field overlap integral vanishes. Here $z_1 \approx 3.83$ is the first zero of the J_1 Bessel function. As a consequence, the nearest neighbor spots at critical sampling have almost zero overlap, while the overlap with the second neighbors is also low. Thanks to this feature of the hexagonal lattice, we reduce spurious correlations between measured transmitted fields and thus measure a more accurate TM when compared to sampling on a square grid with the same spacing a . The hexagonal grid also has around 15% higher sampling density because its unit cell is smaller. The choice of a hexagonal lattice scan therefore allows the measurement of a larger fraction of the complete TM at the same level of correlations and consequently represents the statistics of the scattering properties of the sample more faithfully.

Next, we compare the effect of sampling density for both lattices, for simplicity assuming $\text{NA} = 1$ and a single polarization component. A good measure to gauge these effects is the normalized rank of the basis of sampling modes, which is defined as the number of linearly independent modes divided by the total number of modes in the basis. We numerically compute the normalized

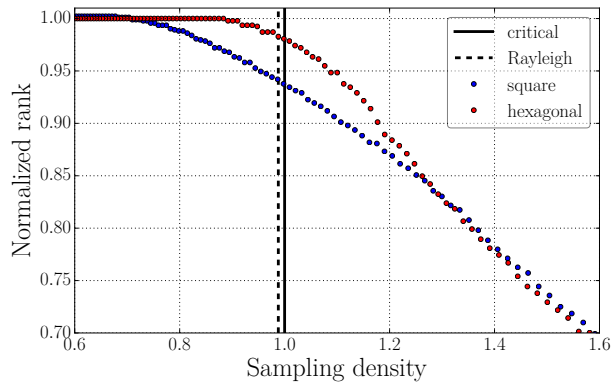


Figure 3.2: Normalized rank of a sampling basis versus the sampling density for a square and hexagonal lattice. The horizontal axis is normalized to the critical sampling density of π/λ^2 , represented by the vertical line at 1. The dashed vertical line indicates the Rayleigh sampling density for the hexagonal lattice. In this numerical calculation $\text{NA} = 1$.

rank of a basis of 933 spots within a circular area for the hexagonal grid and 931 spots within the same area for the square grid, as a function of the area density of sampling points. Computationally we find the normalized rank by constructing the matrix of inner products between the modes of the basis and calculating the fraction of its singular values s that are larger than $c \cdot s_{\text{rms}}$, where s_{rms} is the RMS (root mean square) singular value and $c = 0.05$ is the numerical tolerance factor below which we consider a singular value to be effectively zero. Our results are quite insensitive to the choice of c .

Fig. 3.2 shows the normalized rank as a function of the sampling density N/A , where N is the number of sampling points, normalized to the critical density of π/λ^2 . The vertical line indicates the critical sampling density and the dashed line indicates the Rayleigh criterion for a hexagonal lattice. Ideally, the spots should be orthogonal and therefore lead to a normalized rank of 1. This is indeed the case for either lattice if we sample far below the critical sampling density. Close to the critical sampling density, the hexagonal lattice exhibits less spot overlap as indicated by a normalized rank closer to 1. At the critical sampling density, a hexagonal grid yields a normalized rank of 0.981 while a square one gives 0.935. In other words, close to critical sampling the square lattice induces three times more spurious near-zero singular values than the hexagonal one. Oversampling beyond the critical density can increase signal to noise but only with a square root law in measurement time. Without further data analysis and regularization procedures, it leads to additional spurious zero singular values in the TM as the neighboring lattice spots increase in overlap.

Beyond a sampling density of 1.3, both lattices exhibit a similar amount of spurious zeros. This is not necessarily a problem since any critically or over-sampled basis may be resampled into a strictly orthogonal set of functions that is complete within the FOV and NA, such as Bessel function modes. Such a resampling procedure requires accurate knowledge of the incident fields and introduces extra parameters and complexity in the data analysis which may be undesirable in real-time applications. The hexagonal grid of Airy spots spaced at the Rayleigh criterion is almost a complete basis, close to orthogonal and straightforward to implement in an experiment. To maintain symmetry in the system configuration, we choose to use the same basis in the detection plane, yielding a square TM. In case $NA < 1$, the maximum achievable sampling density unavoidably scales with NA^2 irrespective of the sampling method or lattice, and the results in Fig. 3.2 are still valid with the x -axis now representing the scaled sampling density.

The polarization-complete TM can be composed from four measurements of sub-matrices as [48]

$$T = \begin{pmatrix} T_{HH} & T_{VH} \\ T_{HV} & T_{VV} \end{pmatrix}, \quad (3.4)$$

where H and V are labels for modes which have horizontal and vertical polarization respectively in the back pupil of the objective. Here, the first index indicates the incident polarization while the second indicates the transmitted one. For high NA the polarization is more complicated in the focal plane, but it is uniquely defined in the pupil.

3.3 Measurement and data processing

3.3.1 Apparatus

Our experimental setup to perform polarization-complete TM measurements is depicted in Fig. 3.3. Light from a Helium-Neon continuous wave (CW) laser (JDS Uniphase, 5 mW) with a wavelength of 633 nm first passes through a polarizer to ensure a linear and well defined polarization after which it is split into a signal (transmitted) and reference (reflected) beam. The signal beam is expanded, and directed with a two-axis scan-mirror (Newport FSM-300) towards the sample. A $4f$ relay telescope images the scan mirror to the pupil of the microscope objective O1 (Zeiss Achroplan 63x, 0.95-NA). A $\lambda/2$ -plate on a motorized rotation stage controls the incident beam polarization. The transmitted light is collected with an oil immersion microscope objective O2 (Olympus PlanApo N 60x, 1.42-NA). The vertical and horizontal polarization components of the light are split by a polarizing beamsplitter (PBS) and imaged through a

camera chip and provide a nearly flat intensity profile. The signal and reference path lengths are equal to within a few cm, which is crucial to avoid drifts due to changes of the laser frequency and coherence length. The $\lambda/2$ -plate in the reference arm controls the ratio of the reference beam power directed to the cameras C1 and C2. Two light-emitting diodes (LED1 and LED2, 633 nm), which are switched off during the measurement, enable wide field illumination to locate desired regions of the sample and to focus the microscope objectives on the sample.

To measure the polarization-complete TM (eq. (3.4)), we first set the incident polarization to H, after which the scan mirror steers the beam across the front surface of the sample. We start the spot scan at the center and then spiral outwards, which enables straightforward cropping of the resulting matrix to a smaller spatial area. For each incident spot, the cameras C1 and C2 record the V and H polarized transmitted light respectively. The process is repeated for V incident polarization. Dark and reference beam images, averaged over four images to even out the background noise, are taken before and after the measurement.

3.3.2 Experimental sampling density

The effective area covered by the TM measurement is $A = 156 \mu\text{m}^2$, which corresponds to the hexagonal envelope containing all measured points including half a unit cell outside the outermost spot centers so that the Airy spots belonging to this layer are contained entirely inside the measurement area. This area corresponds to $2\pi A/\lambda^2 = 2443$ optical modes. However, our experimental TM has a dimension of 1838×1838 , resulting in a sampling density of $1838/2443 \approx 0.75$.

The specified NA of our microscope objective O1 is 0.95, but the effective NA retrieved by examining the first zero of the Airy spot is somewhat lower and estimated to be 0.9 possibly due to apertures and slight aberrations in the optical system. The sampling density is therefore estimated to be at $0.75/0.9^2 = 0.93$ of the maximum sampling density allowed by the NA and close to the Rayleigh criterion at 0.988. Hence, according to Fig. 3.2, we expect to be in a situation of slight undersampling but preserving the statistics of the TM very well with only about 1% of spurious zero singular values.

3.3.3 Digital filtering of the transmitted fields

The transmitted fields are measured through the optical system with an NA of 1.4 (objective O2), which exceeds the NA of the incident fields. For the case of a clear medium, and in general whenever we want to obtain a square TM, we need the transmitted fields to be filtered to the same NA as the incident fields.

We accomplish this by digitally Fourier filtering the measured fields. We filter with a supergaussian disc SG with radius R ,

$$SG(r) = \exp \left[-2 \left(\frac{r}{R} \right)^n \right], \quad (3.5)$$

where r is the radial coordinate and the supergaussian exponent is chosen to be $n = 50$. The supergaussian filter reduces the Gibbs phenomenon [52]. We set $R = 1.59 \mu\text{m}^{-1}$, which corresponds to a filter that drops off sharply beyond $\text{NA} = 0.95$, so that it just passes the spatial frequencies present in the incident beam.

3.3.4 Sampling the transmitted field

We convert the measured and filtered fields to a vector by sampling at the positions that correspond to the spot centers of our incident field, which we obtain from the centers of mass (COM) of the transmitted images of the input Airy spots focused on a plain glass slide. The lattice constant of the hexagonal grid of the output basis is the mean separation of the COM of the input spots. We sample the fields at the output lattice points by linearly interpolating the field values from neighboring pixels. In this manner, the output sampling vector has the same size as the incident sampling vector which is equal to the number N of input spots. The measured TM is therefore a square $N \times N$ matrix.

Due to a rotation of the CCDs and possible conformal distortion induced by optical elements, the input and output bases do not overlap exactly. This problem is usually ignored when measuring TMs of strongly scattering samples as there are no theoretical values of the matrix elements to compare to, but it leads to incorrect results for clear samples. To correct for this mismatch with a minimum number of parameters, we use an affine transformation to map the input grid to the measured grid of COM points.

A least squares algorithm is used to minimize the difference between the COM coordinates and the transformed grid coordinates. The result of this transformation is shown in Fig. 3.4. In (a), the generated (output) and measured (input) grids do not initially overlap. After performing an affine transformation on the generated lattice, Fig. 3.4(b) demonstrates that the input and output grids are superimposed to within 60 nm.

3.3.5 Phase drift correction

During the course of the measurement slow phase drifts occur because of temperature, mechanical and laser wavelength drifts. These phase drifts affect the statistics and reproducibility of the measured TM. A typical measurement of a

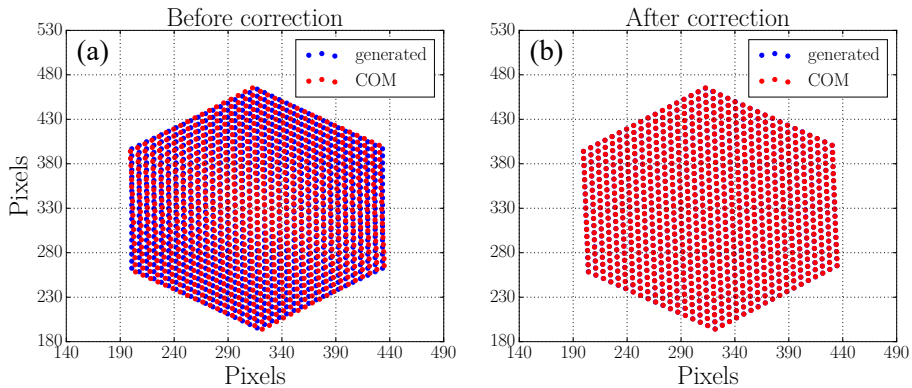


Figure 3.4: Coordinates of the generated hexagonal grid (blue dots) representing the output sampling basis (a) before and (b) after performing an affine transformation to match the grid found from the centers of mass (COM) of the focused input laser spots (red dots).

complete TM of dimension 1838×1838 elements takes approximately 11 minutes, and phase drifts of order 1 rad occur in this time. Similar to the method used in [53], we account for these phase drifts by taking a reference image after every 20 scan positions of the input laser beam. The reference position is chosen to be the central spot of the hexagonal spiral. The phase of these reference fields is then compared to the phase of the starting spot by calculating the angle of their inner product. The phase drifts are interpolated with a one-dimensional smoothing spline fit. Finally, the computed corrections are applied to the retrieved fields to compensate for the phase drifts, reducing the inter-frame phase error to 0.07 rad.

3.4 TM of a zero-thickness reference

We study the accuracy and precision of our method by measuring the TM of a zero-thickness sample, i.e., objectives O1 and O2 are focused in the same plane. The focal plane we choose is the interface between a crown glass microscope cover slide and air. We note that this zero-thickness TM does not contain any near field terms according to the definition of the scattering matrix, and can consequently be measured with far-field optics. We scan 919 incident spots, corresponding to 18 complete hexagon layers across the interface, which leads to a polarization-complete TM of 1838×1838 elements.

A simulated TM is obtained by scanning a numerically generated Airy field on a hexagonal grid, spaced by the Rayleigh criterion just as in the experiment.

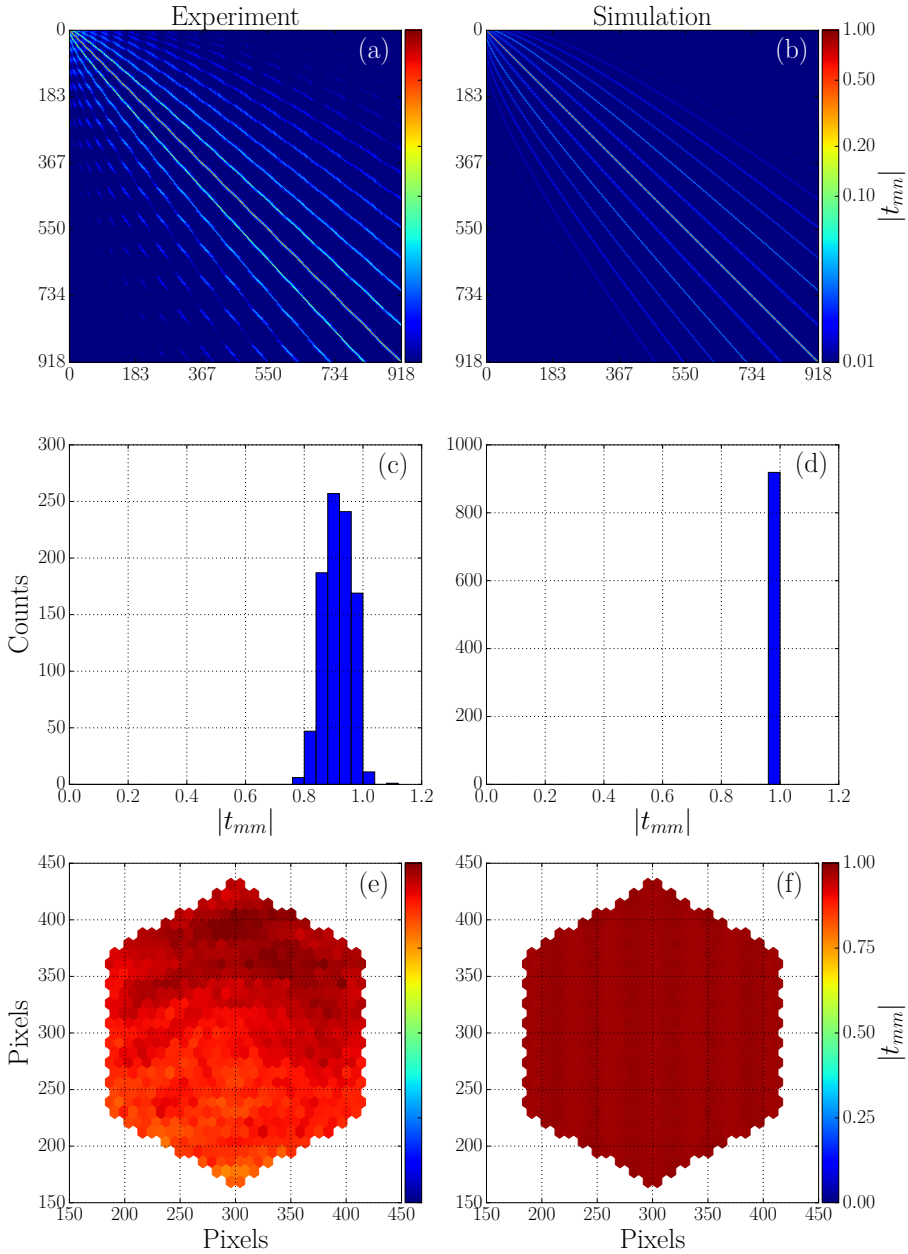


Figure 3.5: Results of the TM measurement and simulations. The left and right column display the measured and simulated results respectively. (a,b) Magnitude of the TM elements for the 919×919 T_{HH} polarization component of a zero-thickness reference. (c,d) Histogram of the magnitudes of the diagonal elements. (e,f) Magnitude of the diagonal elements $|t_{mm}|$ as a function of the input position m .

The number of spots is 919, corresponding to a single polarization component as cross-polarization terms are absent in the numerical case.

The magnitude of one component (H incident, H transmitted) of the measured and simulated TM elements is shown in Fig. 3.5. The magnitude is normalized to the RMS singular value of T_{HH} . In Fig. 3.5(a), the main diagonal of the TM is close to 1 and dominates the off-diagonal elements, with 84% of the total power in the diagonal elements. This indicates that the fields associated to different input spots are nearly orthogonal. Other lines, which are clearly visible due to the logarithmic color scale, emerge from the crosstalk between neighbor and next-neighbor Airy disks. This crosstalk is also visible, albeit at a slightly lower amplitude, in the simulated TM elements in Fig. 3.5(b). In this case 95% of the total power is in the diagonal elements, indicating a smaller level of crosstalk with non-nearest neighbor points. In the histogram in Fig. 3.5(c) we plot the distribution of the magnitude of the diagonal elements, which is peaked close to 1, as expected for a situation with only small crosstalk. The broadened width of the peak compared to the calculated one in Fig. 3.5(d) is attributed to experimental noise and imperfect imaging of the scan mirror on the pupil of the objective O1. In Fig. 3.5(e) we show the magnitude of the diagonal elements as a function of their input position. The nonuniform distribution favoring the upper positions of the grid indicates a slightly angle-dependent transmission of our optical system. In the numerical case displayed in Fig. 3.5(f), the diagonal elements exhibit very small fluctuations of around 1% which arise due to the conversion from a rectangular pixel-based sampling to a hexagonal sampling. We conclude that our experimental data agrees very well with numerical simulations even though this direct comparison detects imperfections in the experiment very sensitively.

A zero-thickness glass sample is the ideal test case to verify whether the sampling procedure leads to distortions of the TM statistics. An important quantitative probe of these statistics is the distribution of the singular values [10, 15]. The singular value histograms of the individual polarization sub-matrices and of the complete TM are plotted in Fig. 3.6. All histograms are normalized to the RMS singular value of the respective co-polarized sub-matrix. In Fig. 3.6(a,e), associated to polarization conserving measurements, the singular value histograms exhibit a pronounced peak at $s = 1$ corresponding to completely transmitting channels. The histogram exhibits a low pedestal extending from $s = 0$ to almost $s = 2$. In Fig. 3.6(b,d), the singular value distributions for the cross-polarization matrices follow the Marchenko-Pastur law [54], which predicts the singular value probability function for a random uncorrelated matrix [55, 56]. Since the glass sample does not cause appreciable cross-polarization scattering, we attribute the random values to a combination

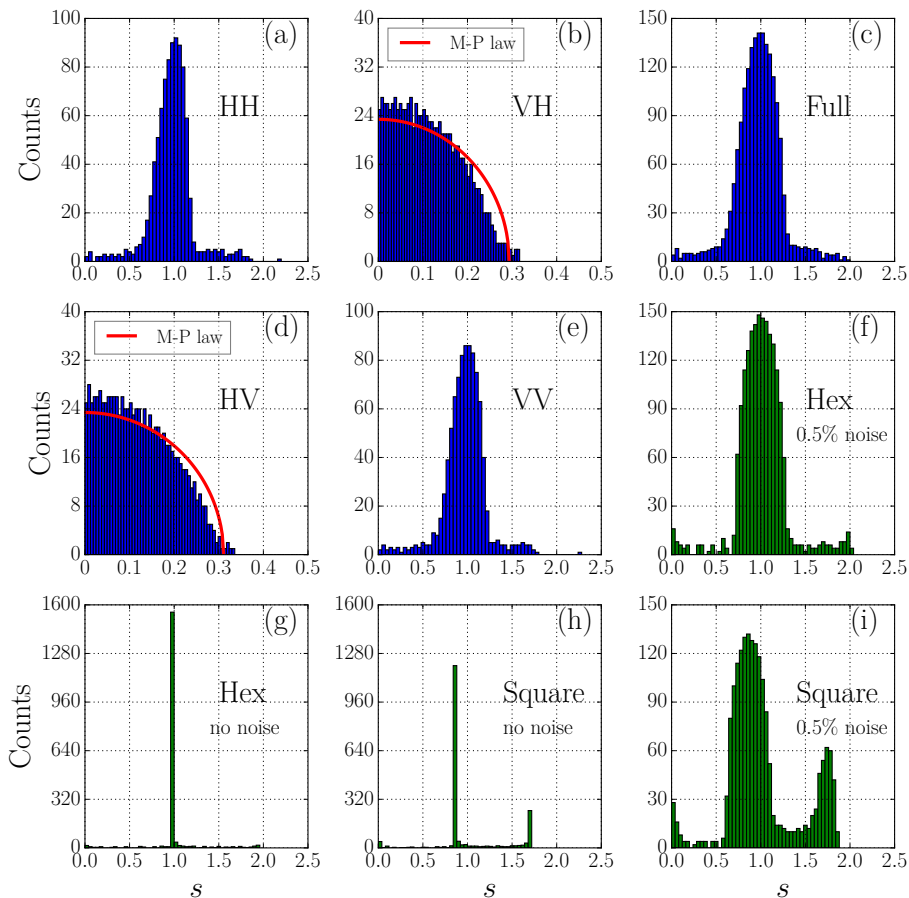


Figure 3.6: Singular value histograms of the transmission matrix. (a,b,d,e) Singular values s of the measured polarization sub-matrices and (c) of the full experimental TM. (f) Simulated histogram for the full TM including 0.5% RMS noise and (g) without noise. (h) Simulated TM for square lattice sampling with the same lattice constant, without noise and (i) with noise. In the cross-polarization matrices (b,d), the red curve corresponds to the Marchenko-Pastur law of a random matrix of the same size.

of camera noise and imperfections in the polarizing beamsplitter. In Fig. 3.6(c) we show the singular value histogram for the full experimental TM, and it resembles the T_{HH} and T_{VV} sub-matrices. The width is a little broader because of the noise from the cross-polarization channels. The singular value histogram of a simulated TM including 0.5% RMS Gaussian random noise on all matrix

elements is displayed in Fig. 3.6(f). We observe that the width of the peak and the pedestal of the experimental histogram are well reproduced by this model. Without noise, as shown in Fig. 3.6(g), the simulated histogram is much narrower, but the pedestal remains. We conclude that the peak width is caused by experimental noise while the pedestal is a sampling feature. The low density of effectively zero singular values ($s < 0.05$) indeed matches the results shown in Fig. 3.2. For comparison we plot in Fig. 3.6(h,i) the corresponding histograms for the case of square-lattice sampling with the same lattice constant without and with noise, respectively. The square-lattice sampling introduces much stronger spurious side lobes in the histogram, which obscure the true statistics of the sample TM. This proves clearly the advantage of sampling the TM on a hexagonal grid at the Rayleigh criterion.

3.5 Conclusion

In summary, we have measured the optical transmission matrix (TM) of a zero-thickness medium using a novel sampling method, namely a hexagonal sampling grid of Airy disks at the Rayleigh criterion. We show in numerical simulations that this sampling method induces far less distortions in the singular value statistics than the usual procedure of sampling on a square grid. We provide experimental verification of the statistics in a reference case of a zero-thickness sample. Experimentally verifying that sampling does not lead to distortion of the statistics is an important prerequisite for probing more complex samples such as scattering media. The advantage of sampling on a Rayleigh-criterion spaced hexagonal grid applies to any kind of waves including ultrasound and microwaves, and it can be used to measure the transmission matrix of fibers [42, 57–60], waveguides [19] and for full scattering matrix measurements of samples in other geometries.

3.A Geometrical limitations

In an experimental measurement of the TM, we assume that both the source and detector are at a large distance R from the sample, and we make a specific choice for the source and detection planes, namely a half-sphere S with radius R on either side of the sample. Furthermore, we assume that the area of interest on the scattering sample is much smaller than R . In such a configuration, the far field expressions used in this chapter are valid.

The TM element $t_{\sigma\mathbf{k}\sigma'\mathbf{k}'}$ is the response to sending an incident plane wave with wave vector \mathbf{k} and polarization σ on the sample that is transmitted with wave vector \mathbf{k}' and polarization σ' in the far field. Theoretically, the incoming and outgoing k -vectors span the entire half-sphere S on either side of the sample. However, experimentally, there is a cutoff spatial frequency determined by the numerical aperture (NA) of two microscope objectives on either side of the sample. The incident objective is for illuminating the sample and the objective behind the sample is to collect the transmitted light. The area of interest is given implicitly by the field of view (FOV) of the objective.

For an infinite slab the flux normalized channels are plane waves, which carry a flux through that sample surface that is proportional to $\cos\theta$, where θ is the angle between the k -vector and the normal to the sample surface. However a camera or other intensity detector that is parallel to the sample plane measures flux, taking care of the flux normalization. When measuring in the pupil of the objective we automatically get a flux normalized measurement of the coefficients $\phi(\mathbf{k})$ of the flux in direction \mathbf{k} .

If the objectives fulfil the Abbe sine condition [46], they map the channels \mathbf{k} to spots in the back focal plane according to $x = Mk_x/k_0$ and $y = Mk_y/k_0$, with M being the magnification of the objectives. Each k -vector incident on the sample corresponds thus to one point on the back focal plane of the illumination objective. This point in turn can be mapped to the source plane with a Fourier transform. If the objective has a high magnification, then the spread of angles on the source plane is small ($< 4^\circ$), i.e., the field is paraxial. In that case, the source plane can be considered parallel to the sample and the field fluxes are proportional to the absolute square of the fields.

Similarly, the light emerging from the collection objective is further imaged on a camera with an imaging lens with a large focal distance (> 20 cm). This again corresponds to a small angle spread, so the camera plane can be approximated to lie on the detection sphere S . Therefore, the fields are no longer different quantities and we do not have to worry about flux normalization on the camera image.

3.B Procedural details

3.B.1 Auto-focusing on the sample

To ensure diffraction limited laser spots on the front surface of the sample and focused images of the back surface with cameras C1 and C2, the setup requires the front surface of the sample to be at the focus of the microscope objective O1 and the back surface at the focus of O2 (see Fig. 3.3). It is important to note that accurate focusing using a contrast criterion requires incoherent illumination, as under coherent illumination there is always a high speckle contrast. To achieve a consistent focusing condition, we automate the process by using an auto-focusing algorithm [61].

To focus on the front surface of the sample, we shine LED1 on the sample and capture the reflected intensity image with the camera C3 (Basler daA1600-60um). The objective O1, mounted on a closed loop piezo-actuated stage (Thorlabs 3-axis NanoMax flexure stage), is approximately placed at a focal distance away from the sample. It is then programmed to move longitudinally in sufficiently small steps ($d \approx 75$ nm), at each of which an image is taken and its sharpness metric calculated.

To obtain a sharpness metric for an $M \times N$ image, its Fourier transform F is computed. We then take its absolute value and identify the maximum value $V = \max(|F|)$ of the frequency component in F . A threshold $T = V/1000$ is set and we find the total number of pixels P whose pixel value is greater than the threshold T . The sharpness metric S for the image is then given by

$$S = \frac{P}{M \times N}. \quad (3.6)$$

Finally, the objective O1 is moved to the longitudinal point where the sharpness metric is at its maximum. The same method is used to focus on the back surface of the sample by using LED2 and camera C2. The focusing condition is quite insensitive to the the threshold T as long as it is chosen such that camera noise is rejected.

The result of such an auto-focusing procedure on a glass slide coated with a thin layer of ZnO nanoparticles is depicted in Fig. 3.7. The width of the sharpness metric in Fig. 3.7(a) is relatively narrow (≈ 2.0 μm) and thus shows that the focus is sensitive to the position of the microscope objective. Fig. 3.7(b) and Fig. 3.7(d) illustrate a defocused image on either side of the focus, and Fig. 3.7(c) shows the focused image found by the algorithm.

The auto-focusing algorithm described above works when focusing on a scattering sample as long as the correct focus position is within the 20 μm travel range of the objective stage and the thickness variation of the sample in the

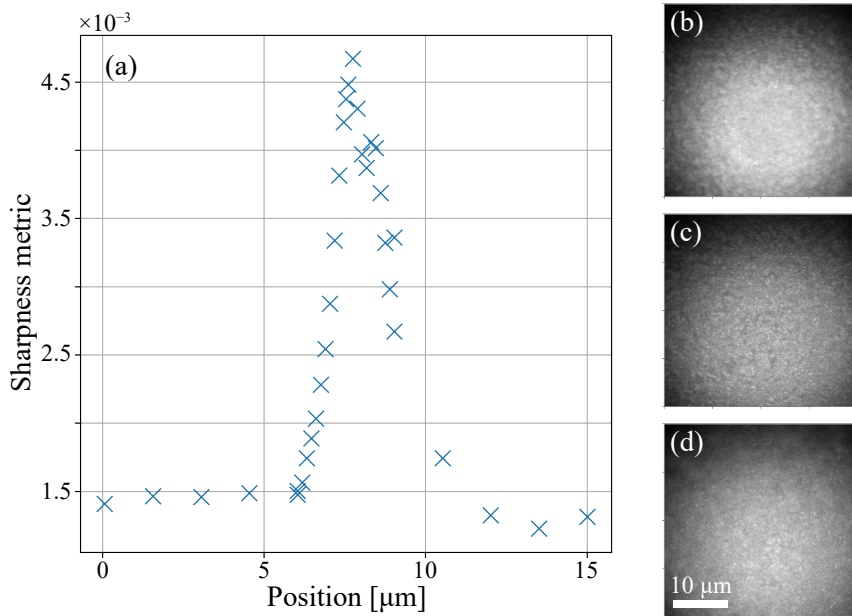


Figure 3.7: Auto-focusing on a sample of ZnO nanoparticles. (a) Sharpness metric of the camera image as a function of the position, in micrometers, of the incident objective. (b) Defocused image corresponding to a point to the left of the sharpness peak. (c) Focused image for which the sharpness metric is highest. (d) Defocused image corresponding to a point to the right of the sharpness peak.

camera's field of view is less than a micron. However, it is harder to use this algorithm when attempting to focus on a plain microscope cover glass because of a lack of image contrast. In such cases, we search for dust specks on the glass surface and focus on these dust particles.

3.B.2 Step size calibration

The Rayleigh criterion refers to the smallest spot separation at which there is no correlation between the corresponding incident fields. Mathematically, this is the smallest distance at which the dot product or field overlap of the input fields falls to zero. The scalar product of two Airy fields $A(x, y)$ and $A(x - x_0, y - y_0)$ centered at $(0, 0)$ and (x_0, y_0) respectively is expressed as

$$q(x_0, y_0) = \int_{-\infty}^{\infty} \int_{-\infty}^{\infty} dx dy A(x, y) A^*(x - x_0, y - y_0). \quad (3.7)$$

This can first be expanded by using the definition of the Fourier transform $\tilde{A}(k_x, k_y)$ of $A(x, y)$, and then simplified using that of the delta function to obtain

$$\begin{aligned}
 q(x_0, y_0) &= \iint_{-\infty}^{\infty} dx dy \iint_{-\infty}^{\infty} \frac{dk_x}{2\pi} \frac{dk_y}{2\pi} \tilde{A}(k_x, k_y) e^{i(k_x x + k_y y)} \\
 &\quad \iint_{-\infty}^{\infty} \frac{dk'_x}{2\pi} \frac{dk'_y}{2\pi} \tilde{A}^*(k'_x, k'_y) e^{i(k'_x(x-x_0) + k'_y(y-y_0))} \\
 &= \iint_{-\infty}^{\infty} \frac{dk_x}{2\pi} \frac{dk_y}{2\pi} \iint_{-\infty}^{\infty} \frac{dk'_x}{2\pi} \frac{dk'_y}{2\pi} \tilde{A}(k_x, k_y) \tilde{A}^*(k'_x, k'_y) e^{i(k'_x x_0 + k'_y y_0)} \\
 &\quad \iint_{-\infty}^{\infty} dx dy e^{i((k_x - k'_x)x + (k_y - k'_y)y)} \\
 &= \iint_{-\infty}^{\infty} \frac{dk_x}{2\pi} \frac{dk_y}{2\pi} \iint_{-\infty}^{\infty} \frac{dk'_x}{2\pi} \frac{dk'_y}{2\pi} \tilde{A}(k_x, k_y) \tilde{A}^*(k'_x, k'_y) e^{i(k'_x x_0 + k'_y y_0)} \\
 &\quad 2\pi\delta(k_x - k'_x) \cdot 2\pi\delta(k_y - k'_y) \\
 &= \iint_{-\infty}^{\infty} \frac{dk_x}{2\pi} \frac{dk_y}{2\pi} |\tilde{A}(k_x, k_y)|^2 e^{i(k_x x_0 + k_y y_0)}.
 \end{aligned}$$

The Fourier transform of an Airy field is a disk with some amplitude h [62], and since the squared modulus of a disk is the same disk but with amplitude h^2 , we have

$$q(x_0, y_0) = h \iint_{-\infty}^{\infty} \frac{dk_x}{2\pi} \frac{dk_y}{2\pi} \tilde{A}(k_x, k_y) e^{i(k_x x_0 + k_y y_0)} = h A(x, y), \quad (3.8)$$

thereby proving that the field overlap between two Airy fields $A(x, y)$ is also an Airy field but with a squared amplitude. Consequently, the ideal step size corresponds to the first zero of this Airy field.

To determine this ideal step size, we scan the beam across the sample in steps much smaller than the expected ideal separation. Since we choose to distribute our spots in a hexagonal lattice as explained in Section 3.2, we perform our calibration scan in the directions along the three sides of an equilateral triangle as depicted in Fig. 3.8 – in the horizontal (0°), southwest-northeast (SW-NE, $+60^\circ$) and northwest-southeast (NW-SE, -60°) directions. We typically scan the beam back and forth along these three directions and calculate the corresponding field overlap for all point separations. To calculate the field we use the off-axis digital holography method described in Section 3.B.3.

The field overlap plot in Fig. 3.9, realized on a microscope cover glass, shows the averaged real part of the field overlap as a function of the spot separation. We don't expect any different behavior for the three different scan directions because the field overlap should only depend on the spot separation and not on

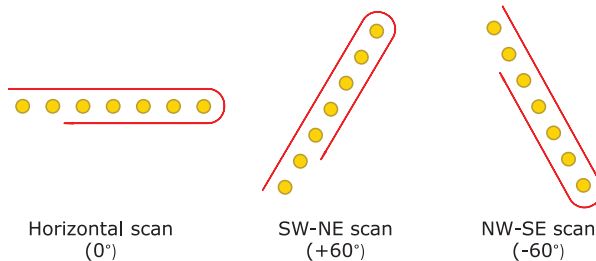


Figure 3.8: Different directions along which a back-and-forth calibration line-scan is performed. The directions are selected along the sides of an equilateral triangle – in the horizontal (0°), southwest-northeast (SW-NE, $+60^\circ$) and northwest-southeast (NW-SE, -60°) directions.

the direction. This is exactly what we observe in the field overlap plot shown in Fig. 3.9, realized on a microscope cover glass, where there is no significant deviations in the curves along the three different scan directions. The slight mismatch of the curves occurs because the beam center incident on the scan mirror does not completely coincide with the pivot point of the mirror. The tails of the curves deviate more since the field amplitude of the tails is comparable to the background noise. For a point spacing of 0, one would expect a field overlap of 1, but the graph indicates a lower value about 0.9. The reason for this is that we don't correlate any measured field with itself but rather correlate the fields that should correspond to the same point in space when we scan the beam forward and backward during the calibration line-scans in the three selected directions. The reduced value of around 0.9 is a result of the experimental noise, but it is however still the highest correlation value as expected. The curve itself resembles an Airy pattern, representative of the diffraction limited focus on the input side and as predicted by eq. (3.8). The Rayleigh criterion step size where the curve first drops to zero is found to be at a spacing of 450 nm. This step size is then selected as the spot separation during the measurement of the TM, described earlier in Section 3.3.1.

3.B.3 Field retrieval using off-axis holography

To find the transmission matrix, we need to know in image space the complex amplitudes of the light scattered into each transmission channel. The cameras in the setup however only measure the beam intensity. Therefore, in order to retrieve the phase of the electric fields, we use a method known as off-axis holography wherein the signal beam is made to interfere with a known reference

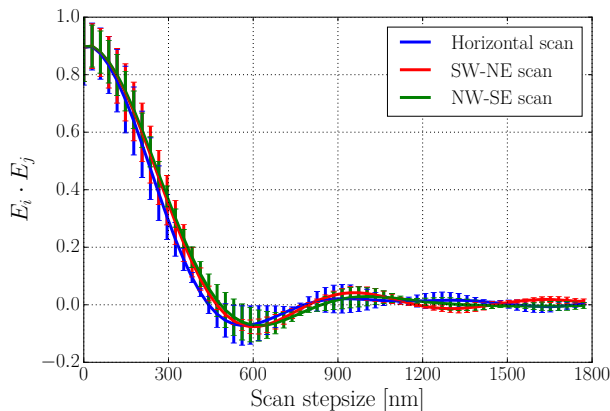


Figure 3.9: Field overlap of transmitted fields through a microscope cover slide. The graph shows the real part of the Hermitian product of the transmitted fields as a function of input spot separation along three different directions, plotted in three different colors. The first zero corresponding to a point spacing of 450 nm is the selected step size.

beam. This method was first proposed by Leith and Upatnieks [49], the idea of its digital implementation was later suggested by Takeda [50], and the way in which we numerically use it first appeared in [51]. The advantage of this technique is that the field can be obtained with a single interferometric image.

In this interferometric technique, the signal beam is normal to the camera sensor and the reference beam is tilted at an angle θ with respect to the signal beam. If the reference beam E_r has the same polarization as the signal beam E_s , the intensity I measured on the camera (in the xy -plane) is given by

$$\begin{aligned}
 I(x, y) = & \underbrace{|E_r(x, y)|^2 + |E_s(x, y)|^2}_{\text{centered at } 0} \\
 & + \underbrace{E_r(x, y)E_s^*(x, y)e^{ik \sin \theta \cdot (x+y)}}_{\text{centered at } +\nu} \\
 & + \underbrace{E_r^*(x, y)E_s(x, y)e^{-ik \sin \theta \cdot (x+y)}}_{\text{centered at } -\nu}, \quad (3.9)
 \end{aligned}$$

where k is the wavevector of the laser beam and $\nu = k \sin \theta / (2\pi)$ is the phase gradient resulting from the tilt between the signal and reference beams. The recorded intensity, shown in Fig. 3.10(a) for a focused beam through a standard microscope cover glass, can be grouped into three terms centered around spatial frequencies 0, $+\nu$ and $-\nu$. This becomes apparent when taking the Fourier

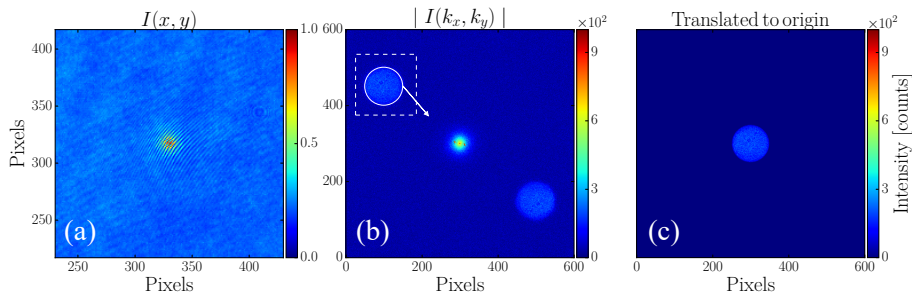


Figure 3.10: (a) Intensity image on the camera, consisting of the signal beam (focused spot at the center) and the reference beam (uniform background). (b) FFT of the intensity image. The center of mass of the -1 order is found inside the bigger dashed box and then a smaller circle is drawn around the center of mass to filter the -1 order. (c) The circle containing the -1 order is translated to the center.

transform of the intensity profile. The result, for which the Fourier transform of the reference beam image has been subtracted, is plotted in Fig. 3.10(b).

If the carrier frequency ν is greater than the maximal spatial frequency of the intensity terms centered around 0, the three terms are separable in momentum space, as is the case in Fig. 3.10(b). At the same time, ν should be smaller than $f_{\text{Nyq}}/2 = 2\pi/(2d_{\text{pix}})$, where f_{Nyq} is the Nyquist frequency and d_{pix} is the camera pixel size. This ensures that the ± 1 orders fit within the bounds of Fourier space. We also note the correction due to the modulation transfer function (MTF) of the detection system, which represents the image contrast as a function of the spatial frequency. The MTF is large (close to 1) for low spatial frequencies and reduces for higher frequencies, and the exact response depends on the shape and size of the camera pixels [62, 63]. Thus, we prefer the first order terms to be located at low spatial frequencies well below the Nyquist frequency.

Next, to determine the value of the carrier frequency ν , the following procedure is performed only once at the start of the measurement. We isolate one of the terms centered around $-\nu$ or $+\nu$. The choice doesn't matter since they are simply each other's complex conjugate. To isolate them effectively, we first determine the center of mass inside the bigger dashed box drawn in Fig. 3.10(b). To prevent low intensities consisting of noise from affecting the position of the true center of mass, we neglect the elements with the bottom 50% intensities when determining the center of mass. We then filter the first order by multiplying it with a supergaussian disc as explained in Section 3.3.3. By isolating the first order term in this way and translating it to the origin, i.e.,

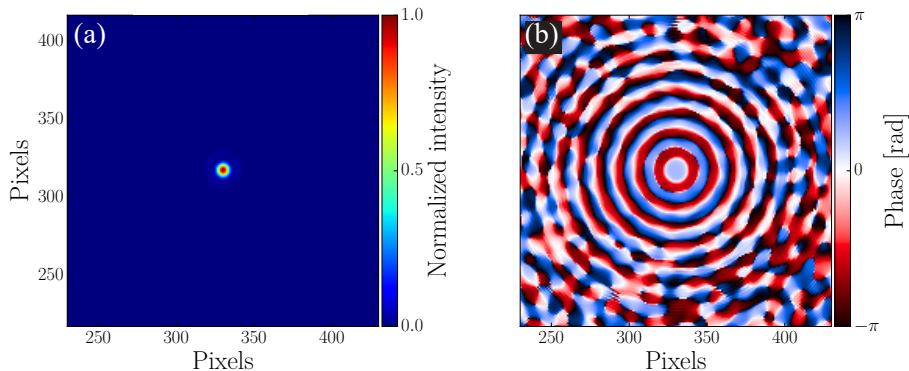


Figure 3.11: (a) Normalized intensity and (b) phase of the retrieved field of a focused spot on a microscope cover glass.

setting $\nu = 0$, we have $\tilde{I}(k_x, k_y) = \mathcal{F}[E_r^*(x, y)E_s(x, y)]$, depicted in Fig. 3.10(c). Taking subsequently its inverse Fourier transform, we are finally left with

$$\tilde{E} = E_r^*(x, y)E_s(x, y). \quad (3.10)$$

If the reference beam is a plane wave with a flat phase profile, then $E_r^*(x, y) = |E_r(x, y)|$ is a constant which can be divided out to obtain the original complex signal field $E_s(x, y)$. In practice, the magnitude of the retrieved field is $ME_s(x, y)$, where M is the MTF of the camera. Assuming that the MTF is constant over the first order region, the field modulus is simply scaled to a lower value because of the reduced contrast. The retrieved intensity and phase of a diffraction limited spot on a glass slide are plotted in Fig. 3.11.

3.B.4 Digital correction for out-of-focus images

The transmission images in the experimental procedure are taken by two cameras C1 and C2, shown in Fig. 3.3. Since these two cameras are placed at the focal plane of the imaging lens by hand, they might not lie exactly at the focal plane and each of them could also have a slightly different distance to the lens. Since the lens has a focal length of 20 cm, it has a sufficiently small NA and the beams can therefore be propagated to the correct plane using Fourier optics.

The reference image to calibrate the camera positions is the image of a focused laser spot on a standard microscope cover glass. The transmitted field is retrieved using off-axis holography. As described in [62], the field can subsequently be propagated along the optical axis using the transfer function of free

space given by

$$H(f_x, f_y, z) = \exp \left[iz \sqrt{(2\pi\lambda^{-1})^2 - (2\pi f_x)^2 - (2\pi f_y)^2} \right], \quad (3.11)$$

where f_x and f_y are the spatial frequencies in the x - and y -directions, z is the distance along the optical axis and λ is the wavelength of the laser light. At every z -position, the intensity is fitted with an Airy disk even though out of the focal plane the intensity profile is not strictly an Airy pattern. The position at which the first zero of the Airy disk is the smallest corresponds to the correct focal plane of the imaging system. The value of the first zero radius is nearly constant around this plane since it falls within the Rayleigh range of the imaged beam. Beyond the Rayleigh range, the beam expands more rapidly and consequently so does the first zero of the Airy fit.

Once the ideal z -position for each camera has been found, its value is kept fixed since the cameras do not move during the experiment. All the fields retrieved in the post-processing are then propagated appropriately to the correct imaging plane of the respective camera after the digital Fourier filtering step.

3.B.5 Affine transformation

To correct for the mismatch between the input and output sampling lattices, we use an affine transformation to transform the generated output grid G_{gen} with coordinates (x, y) to the grid G_{COM} found by the measured input spot COMs with coordinates $(x_{\text{COM}}, y_{\text{COM}})$. The problem can be mathematically stated as

$$G_{\text{gen}} \cdot A = G_{\text{COM}}, \quad (3.12)$$

with A being the affine transformation matrix. The equation can be explicitly expressed as

$$\begin{pmatrix} y_1 & x_1 & 1 \\ y_2 & x_2 & 1 \\ \vdots & \vdots & \vdots \\ y_N & x_N & 1 \end{pmatrix} \cdot \begin{pmatrix} a_{1,y} & a_{1,x} \\ a_{2,y} & a_{2,x} \\ a_{3,y} & a_{3,x} \end{pmatrix} = \begin{pmatrix} y_{1,\text{COM}} & x_{1,\text{COM}} \\ y_{2,\text{COM}} & x_{2,\text{COM}} \\ \vdots & \vdots \\ y_{N,\text{COM}} & x_{N,\text{COM}} \end{pmatrix}, \quad (3.13)$$

with G_{gen} padded with ones as its third column so that the transformation can perform translations too. The constants $a_{3,x}$ and $a_{3,y}$ represent the global translation of the generated grid in the x - and y -directions respectively. This can be seen when transforming the i^{th} generated coordinate-pair to its corresponding

COM counterpart:

$$x_{i,\text{COM}} = a_{1,x}y_i + a_{2,x}x_i + a_{3,x}, \quad (3.14)$$

$$y_{i,\text{COM}} = a_{1,y}y_i + a_{2,y}x_i + a_{3,y}. \quad (3.15)$$

Since the grid formed of COMs is in general not completely evenly spaced because of optical aberrations, there is no exact solution to the affine transformation. Hence, a least squares algorithm is used to minimize the difference between the COM coordinates and the transformed grid coordinates.

3.C Eigenvalue statistics

Along with the singular values of the TM, another essential statistic of the TM is its eigenvalue spectrum, which is of interest because the associated eigenvectors are waves that enter and exit the medium with the exact same spatial profile. For eigenvalues λ_n and eigenvectors E_n , we have the eigenvalue equation

$$TE_n = \lambda_n E_n. \quad (3.16)$$

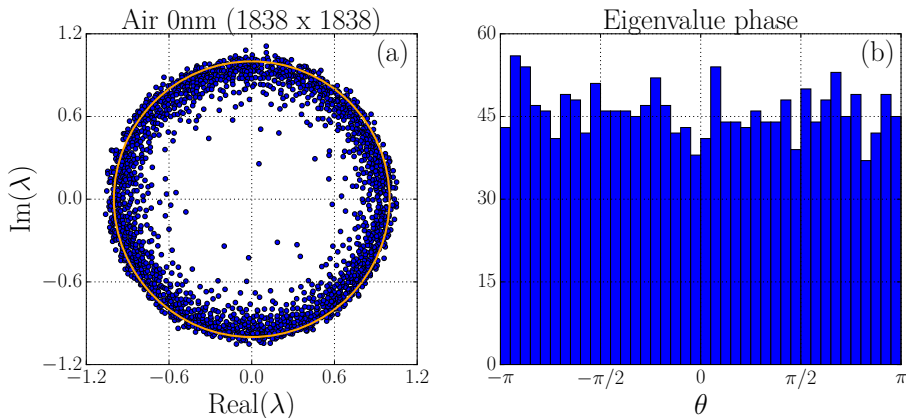


Figure 3.12: (a) Complex eigenvalue spectrum of a zero-thickness TM. The horizontal and vertical axes represent the real and imaginary axes respectively. The orange circle with radius 1 serves as a guide to the eye. (b) Histogram of the phases θ of the complex eigenvalues.

The zero-thickness matrix T must be diagonal and real (ideally the identity matrix), so $T^\dagger = T$. In that case

$$T^\dagger T E_n = T^2 E_n = \lambda_n^2 E_n. \quad (\text{zero thickness TM}) \quad (3.17)$$

Since the singular values are the square root of the eigenvalues of $T^\dagger T$, we see that for the zero-thickness TM the eigenvalues and the singular values are identical up to a sign and we should also observe this in our measurements.

The complex eigenvalue spectrum, plotted in Fig. 3.12, shows that nearly all the eigenvalues have a modulus of 1. This is reasonable because all the eigenmodes present in the zero thickness medium must be completely transmitting with eigenvalue 1. In the ideal case all eigenvalues should be identical to the singular values and therefore must be real. However, we observe that they are spread out more or less uniformly in the complex plane and the phase is randomized as shown in Fig. 3.12(b). We attribute this to experimental noise, a non-telecentric optical setup, aberrations and non-flatness of the incident fields.

These effects do not show up when computing the singular values as in eq. (3.17) because the T^\dagger cancels all the distortions introduced by T . The study of eigenvalues and eigenvectors therefore provides a metric for the alignment of our system and its consequences on the generated TM that complements the study of singular values.

Bibliography

- [1] M. Nieto-Vesperinas and E. Wolf, “Generalized Stokes reciprocity relations for scattering from dielectric objects of arbitrary shape,” *J. Opt. Soc. Am. A* **3**, 2038–2046 (1986).
- [2] A. Lagendijk and B. A. van Tiggelen, “Resonant multiple scattering of light,” *Physics Reports* **270**, 143 – 215 (1996).
- [3] C. W. J. Beenakker, “Random-matrix theory of quantum transport,” *Rev. Mod. Phys.* **69**, 731–808 (1997).
- [4] S. M. Popoff, G. Lerosey, R. Carminati, M. Fink, A. C. Boccarda, and S. Gigan, “Measuring the transmission matrix in optics: An approach to the study and control of light propagation in disordered media,” *Phys. Rev. Lett.* **104**, 100601 (2010).
- [5] A. P. Mosk, A. Lagendijk, G. Lerosey, and M. Fink, “Controlling waves in space and time for imaging and focusing in complex media,” *Nature photonics* **6**, 283–292 (2012).
- [6] M. C. W. van Rossum and T. M. Nieuwenhuizen, “Multiple scattering of classical waves: microscopy, mesoscopy, and diffusion,” *Rev. Mod. Phys.* **71**, 313–371 (1999).
- [7] S. Rotter and S. Gigan, “Light fields in complex media: Mesoscopic scattering meets wave control,” *Rev. Mod. Phys.* **89**, 015005 (2017).
- [8] E. van Putten and A. P. Mosk, “The information age in optics: Measuring the transmission matrix,” *Physics* **3**, 1–3 (2010).
- [9] B. Saleh and M. Teich, *Fundamentals of Photonics*, Wiley Series in Pure and Applied Optics (Wiley, 2007).
- [10] D. A. B. Miller, “Waves, modes, communications, and optics: a tutorial,” *Adv. Opt. Photon.* **11**, 679–825 (2019).
- [11] Y. V. Nazarov and Y. M. Blanter, *Quantum Transport: Introduction to Nanoscience* (Cambridge University Press, 2009).
- [12] E. N. Economou and C. M. Soukoulis, “Static conductance and scaling theory of localization in one dimension,” *Phys. Rev. Lett.* **46**, 618–621 (1981).
- [13] H. Baranger, D. DiVincenzo, R. Jalabert, and A. Stone, “Classical and quantum ballistic-transport anomalies in microjunctions,” *Phys. Rev. B* **44**, 10637–10675 (1991).
- [14] D. S. Fisher and P. A. Lee, “Relation between conductivity and transmission matrix,” *Phys. Rev. B* **23**, 6851–6854 (1981).
- [15] J. Pendry, A. MacKinnon, and A. Pretre, “Maximal fluctuations – a new phenomenon in disordered systems,” *Physica A: Statistical Mechanics and its Applications* **168**, 400–407 (1990).
- [16] P. Mello, P. Pereyra, and N. Kumar, “Macroscopic approach to multichan-

- nel disordered conductors,” *Annals of Physics* **181**, 290 – 317 (1988).
- [17] T. Martin and R. Landauer, “Wave-packet approach to noise in multichannel mesoscopic systems,” *Phys. Rev. B* **45**, 1742–1755 (1992).
- [18] I. M. Vellekoop and A. P. Mosk, “Universal optimal transmission of light through disordered materials,” *Phys. Rev. Lett.* **101**, 120601 (2008).
- [19] Z. Shi and A. Z. Genack, “Transmission eigenvalues and the bare conductance in the crossover to Anderson localization,” *Phys. Rev. Lett.* **108**, 043901 (2012).
- [20] M. Davy, Z. Shi, J. Wang, and A. Z. Genack, “Transmission statistics and focusing in single disordered samples,” *Opt. Express* **21**, 10367–10375 (2013).
- [21] B. Gérardin, J. Laurent, A. Derode, C. Prada, and A. Aubry, “Full transmission and reflection of waves propagating through a maze of disorder,” *Phys. Rev. Lett.* **113**, 173901 (2014).
- [22] X. Hao, L. Martin-Rouault, and M. Cui, “A self-adaptive method for creating high efficiency communication channels through random scattering media,” *Sci. Rep.* **4** (2014).
- [23] S. Liew, S. Popoff, A. Mosk, W. Vos, and H. Cao, “Transmission channels for light in absorbing random media: from diffusive to ballistic-like transport,” *Phys. Rev. B* **89**, 224202–1–224202–10 (2014).
- [24] M. Kim, W. Choi, C. Yoon, G. H. Kim, S. hyun Kim, G.-R. Yi, Q.-H. Park, and W. Choi, “Exploring anti-reflection modes in disordered media,” *Optics Express* **23**, 12740 (2015).
- [25] M. Davy, Z. Shi, J. Park, C. Tian, and A. Z. Genack, “Universal structure of transmission eigenchannels inside opaque media,” *Nature Communications* **6** (2015).
- [26] A. Daniel, L. Liberman, and Y. Silberberg, “Wavefront shaping for glare reduction,” *Optica* **3**, 1104–1106 (2016).
- [27] D. Akbulut, T. Strudley, J. Bertolotti, E. P. A. M. Bakkers, A. Lagendijk, O. L. Muskens, W. L. Vos, and A. P. Mosk, “Optical transmission matrix as a probe of the photonic strength,” *Phys. Rev. A* **94**, 043817 (2016).
- [28] C. W. Hsu, S. F. Liew, A. Goetschy, H. Cao, and A. D. Stone, “Correlation-enhanced control of wave focusing in disordered media,” *Nature Physics* **13**, 497–502 (2017).
- [29] P. Hong, O. S. Ojambati, A. Lagendijk, A. P. Mosk, and W. L. Vos, “Three-dimensional spatially resolved optical energy density enhanced by wavefront shaping,” *Optica* **5**, 844–849 (2018).
- [30] P. Fang, C. Tian, L. Zhao, Y. P. Bliokh, V. Freilikher, and F. Nori, “Universality of eigenchannel structures in dimensional crossover,” *Phys. Rev. B* **99**, 094202 (2019).

- [31] H. Yilmaz, C. W. Hsu, A. Goetschy, S. Bittner, S. Rotter, A. Yamilov, and H. Cao, “Angular memory effect of transmission eigenchannels,” *Phys. Rev. Lett.* **123**, 203901 (2019).
- [32] H. Yilmaz, C. W. Hsu, A. Yamilov, and H. Cao, “Transverse localization of transmission eigenchannels,” *Nature Photonics* **13**, 352–358 (2019).
- [33] A. Goetschy and A. D. Stone, “Filtering random matrices: The effect of incomplete channel control in multiple scattering,” *Phys. Rev. Lett.* **111**, 063901 (2013).
- [34] H. Yu, T. R. Hillman, W. Choi, J. O. Lee, M. S. Feld, R. R. Dasari, and Y. Park, “Measuring large optical transmission matrices of disordered media,” *Phys. Rev. Lett.* **111**, 153902 (2013).
- [35] R. Sprik, A. Tourin, J. de Rosny, and M. Fink, “Eigenvalue distributions of correlated multichannel transfer matrices in strongly scattering systems,” *Phys. Rev. B* **78**, 012202 (2008).
- [36] A. Aubry and A. Derode, “Random matrix theory applied to acoustic backscattering and imaging in complex media,” *Phys. Rev. Lett.* **102**, 084301 (2009).
- [37] S. Popoff, G. Lerosey, M. Fink, A. C. Boccarda, and S. Gigan, “Image transmission through an opaque material,” *Nature Communications* **1**, 81 (2010).
- [38] Y. Choi, T. D. Yang, C. Fang-Yen, P. Kang, K. J. Lee, R. R. Dasari, M. S. Feld, and W. Choi, “Overcoming the diffraction limit using multiple light scattering in a highly disordered medium,” *Phys. Rev. Lett.* **107**, 023902 (2011).
- [39] M. Kim, Y. Choi, C. Yoon, W. Choi, J. Kim, Q.-H. Park, and W. Choi, “Maximal energy transport through disordered media with the implementation of transmission eigenchannels,” *Nature Photonics* **6**, 581–585 (2012).
- [40] W. Choi, C. Fang-Yen, K. Badizadegan, S. Oh, N. Lue, R. R. Dasari, and M. S. Feld, “Tomographic phase microscopy,” *Nature Methods* **4**, 717–719 (2007).
- [41] A. Drémeau, A. Liutkus, D. Martina, O. Katz, C. Schülke, F. Krzakala, S. Gigan, and L. Daudet, “Reference-less measurement of the transmission matrix of a highly scattering material using a DMD and phase retrieval techniques,” *Opt. Express* **23**, 11898–11911 (2015).
- [42] M. Plöschner, T. Tyc, and T. Čížmár, “Seeing through chaos in multimode fibres,” *Nat Photon* **9** (2015).
- [43] A. Boniface, I. Gusachenko, K. Dholakia, and S. Gigan, “Rapid broadband characterization of scattering medium using hyperspectral imaging,” *Optica* **6**, 274–279 (2019).
- [44] M. Nieto-Vesperinas, *Scattering and Diffraction in Physical Optics*, 2nd

- Edition* (World Scientific Publishing Company, 2006).
- [45] E. Wolf, “A scalar representation of electromagnetic fields: II,” *Proceedings of the Physical Society* **74**, 269–280 (1959).
 - [46] E. Abbe Hon., “VII. – On the estimation of aperture in the microscope.” *Journal of the Royal Microscopical Society* **1**, 388–423 (1881).
 - [47] D. P. Petersen and D. Middleton, “Reconstruction of multidimensional stochastic fields from discrete measurements of amplitude and gradient,” *Information and Control* **7**, 445 – 476 (1964).
 - [48] S. Tripathi, R. Paxman, T. Bifano, and K. C. Toussaint, “Vector transmission matrix for the polarization behavior of light propagation in highly scattering media,” *Opt. Express* **20**, 16067–16076 (2012).
 - [49] E. N. Leith and J. Upatnieks, “Reconstructed wavefronts and communication theory,” *J. Opt. Soc. Am.* **52**, 1123–1130 (1962).
 - [50] M. Takeda, H. Ina, and S. Kobayashi, “Fourier-transform method of fringe-pattern analysis for computer-based topography and interferometry,” *J. Opt. Soc. Am.* **72**, 156–160 (1982).
 - [51] E. Cuche, P. Marquet, and C. Depeursinge, “Spatial filtering for zero-order and twin-image elimination in digital off-axis holography,” *Appl. Opt.* **39**, 4070–4075 (2000).
 - [52] Y. C. Eldar, *Sampling Theory: Beyond Bandlimited Systems* (Cambridge University Press, 2015).
 - [53] M. Plöschner, B. Straka, K. Dholakia, and T. Čižmár, “GPU accelerated toolbox for real-time beam-shaping in multimode fibres,” *Opt. Express* **22**, 2933–2947 (2014).
 - [54] V. A. Marčenko and L. A. Pastur, “Distribution of eigenvalues for some sets of random matrices,” *Mathematics of the USSR-Sbornik* **1**, 457–483 (1967).
 - [55] M. Mehta, *Random Matrices*, ISSN (Elsevier Science, 2004).
 - [56] J. Shen, “On the singular values of Gaussian random matrices,” *Linear Algebra and its Applications* **326**, 1 – 14 (2001).
 - [57] S. Rosen, D. Gilboa, O. Katz, and Y. R. Silberberg, “Focusing and scanning through flexible multimode fibers without access to the distal end,” (2015).
 - [58] A. Descloux, L. V. Amitonova, and P. W. H. Pinkse, “Aberrations of the point spread function of a multimode fiber due to partial mode excitation,” *Opt. Express* **24**, 18501–18512 (2016).
 - [59] R. N. Mahalati, R. Y. Gu, and J. M. Kahn, “Resolution limits for imaging through multi-mode fiber,” *Opt. Express* **21**, 1656–1668 (2013).
 - [60] N. Borhani, E. Kakkava, C. Moser, and D. Psaltis, “Learning to see through multimode fibers,” *Optica* **5**, 960–966 (2018).
 - [61] K. De and V. Masilamani, “Image sharpness measure for blurred images

- in frequency domain,” *Procedia Engineering* **64**, 149 – 158 (2013). International Conference on Design and Manufacturing (IConDM2013).
- [62] J. Goodman, *Introduction to Fourier Optics*, McGraw-Hill Series in Electrical and Computer Engineering: Communications and Signal Processing (McGraw-Hill, 1996).
- [63] J. C. Feltz and M. A. Karim, “Modulation transfer function of charge-coupled devices,” *Appl. Opt.* **29**, 717–722 (1990).

4 Resampling the transmission matrix in an aberration corrected Bessel mode basis

For any basis composed of a lattice of spots, the transmission matrix (TM) of a medium measured in such a basis will always be accompanied by some sampling crosstalk. For a hexagonal Airy spot basis sampled at the Rayleigh criterion (see Chapter 3), although nearest neighbors are chosen to have no overlap, the same cannot be said for second and further neighbors since the Airy spots have long tails. These nonzero overlap integrals between distant spots prevent the Airy basis from being completely orthogonal and therefore still mar the singular value statistics. In this regard, an alternate choice for resampling the light fields is to use a basis of Bessel modes of the first kind, which is complete and orthogonal on an infinite 2D-plane and on a disk since the modes are solutions of the circular infinite square well [1] and of a cylindrical waveguide [2]. This is a problem normally studied in quantum mechanics [3] and in fiber optics, but we can use the same approach of constructing an orthogonal basis to express the TM of an open 3D system. Such an exercise, to the best of our knowledge, has not been reported. Interestingly, the Bessel modes are also eigenstates of orbital angular momentum (OAM) [4] and, although it is not performed here, we note that a study of the OAM in terms of the TM could be facilitated if the latter is represented with Bessel modes.

In this chapter, we first describe the procedure of resampling the TM measured in a basis of Airy disk into one comprising of Bessel modes. Our resampling procedure implicitly corrects for system aberrations. Furthermore, we compare the performance of the two bases for the TM of a finite thickness of air. We also look at the differences with simulations to examine the influence of the setup alignment, measurement procedure and experimental noise. In the process, we show how the TM of such a thin slab of air is equivalent to that of a confocal cavity with finite mirrors, and that consequently its eigenvectors are related to the Fox-Li modes of the resonator [5,6].

4.1 Resampling procedure

In this section, we describe the procedure of resampling a TM measured in an Airy spot basis to an aberration-corrected basis of Bessel modes of the first kind. We prefer this resampling method to sampling the TM directly with Bessel input modes because it is hard to project the Bessel modes experimentally with high fidelity, especially the higher order ones containing high spatial frequencies. Any noise and aberration in the projected fields would destroy the orthogonality of the basis, and we would thereby not gain any significant advantage in minimizing sampling crosstalk. We also prefer resampling because we can correct for aberrations in the process.

In a basis of Airy spots, the spot-to-spot transmission matrix T_{ss} relates the input and output vectors \vec{x}_s and \vec{y}_s as

$$\vec{y}_s = T_{ss} \cdot \vec{x}_s. \quad (4.1)$$

To resample this matrix into a basis of Bessel modes of the first kind, we first have to define the circular region that will contain the Bessel modes. We choose a circle that is inscribed inside the hexagonal scan area (see Figure 3.4). In this way, we ensure that the entire circle is filled with spots that are scanned by the incident laser beam. In fact, we select a radius R that is half a hexagon-layer-thickness larger than the outermost layer so that the Airy spots belonging to this layer are contained entirely inside the circle. We then set the appropriate boundary conditions that the Bessel beams fall to zero at the circle. We also truncate them to zero outside the circle since we do not have any control or information of this area where we don't scan input spots. This effectively determines the field of view (FOV) of our system.

Once the disk of interest is fixed, we find all the integer-order J_n Bessel modes of the first kind that exist on the disk. A light field E can be separated in two polarization components E_H and E_V (see Chapter 3), and each component can subsequently be decomposed in a basis of Bessel modes as

$$\begin{aligned} E_{pol}(r) &= \sum_n a_n J_l \left(z_{l,n} \frac{r}{R} \right) \cos(l\varphi) & (l \geq 0) \\ &+ \sum_n b_n J_l \left(z_{l,n} \frac{r}{R} \right) \sin(-l\varphi) & (l < 0) \end{aligned}$$

where r and φ are polar coordinates, J_l is the Bessel mode of order l , $z_{l,n}$ is the n^{th} zero of the J_l Bessel function, and $a_n, b_n \in \mathbb{C}$ are the contributing coefficients of each Bessel term. The expression above can equivalently be expressed using complex notation by combining the cosine and sine terms, but we choose to use a real basis because it is computationally more efficient to calculate and store

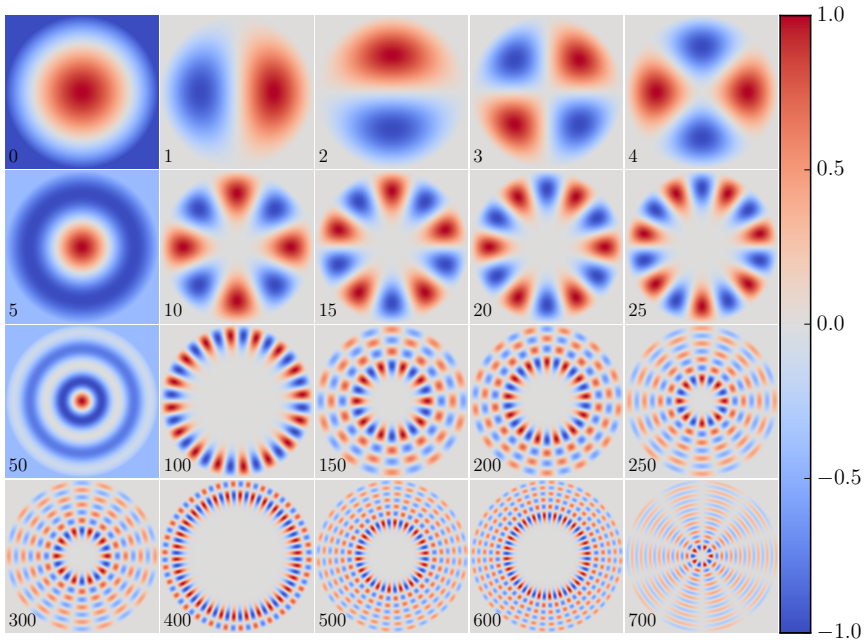


Figure 4.1: Some Bessel functions with their corresponding eigenvalue index (when ordered by the eigenvalue of the Laplacian) indicated at the bottom left. The color scale indicates the normalized amplitude.

the Bessel functions.

We sort the Bessel modes in ascending order based on the eigenvalue $\lambda = z_{n,l}^2$ of the Laplacian, which is equivalent to ordering them as a function of the radial zeros of the Bessel functions. A basis of dimension $2M$ is then formed by selecting the top M Bessel modes for 2 orthogonal polarizations H and V. The number M is taken as the number of Airy spots contained entirely inside the circle. A few Bessel functions are plotted in Figure 4.1. The low eigenvalue indices are more concentrated at the center of the circle, whereas the high ones live more on the edge. Also, as can be seen from indices (1, 2) and (3, 4), the Bessel modes of order $l > 0$ come in pairs, where the spatial profile is the same but they are rotated with respect to one another. These pairs, degenerate in λ , are modes that possess the same radial number n but opposite azimuthal numbers l .

Once the fields have been retrieved using digital holography, as explained in Section 3.B.3, they can directly be decomposed into the Bessel modes. Since the Bessel modes are orthogonal, the decomposition is performed by taking inner

products between the complex fields and the individual Bessel functions. This then yields a spot-to-Bessel transmission matrix T_{sb} . For each incident spot, the decomposition gives one column of T_{sb} . If N Airy spots are scanned for each polarization and there are M Bessel modes per polarization, the dimensions of T_{sb} are $(2M \times 2N)$. This can mathematically be expressed as

$$\vec{y}_b = T_{sb} \cdot \vec{x}_s, \quad (4.2)$$

where \vec{x}_s is still an input field described in an Airy spot basis and \vec{y}_b is a transmitted field in a Bessel basis.

However, we would like to have a TM in a Bessel-to-Bessel basis instead of in a spot-to-Bessel one. We consequently also resample the input Airy spot basis into Bessel modes. This is achieved using a resampling matrix R_{sb} such that $\vec{x}_b = R_{sb} \cdot \vec{x}_s$ [7]. Hence, we rewrite eq. (4.2) as

$$\vec{y}_b = T_{bb} \cdot \vec{x}_b, \quad (4.3)$$

with T_{bb} the TM in a Bessel-to-Bessel basis given by

$$T_{bb} = T_{sb} R_{sb}^{-1}. \quad (4.4)$$

The difficulty arises in finding the resampling matrix R_{sb} . This matrix could be calculated as $R_{sb} = \langle \vec{x}_s | \vec{x}_b \rangle$, but this would entail using theoretical Airy disks that do not contain the aberrations present in the optical setup. Fortunately, we solve the problem by studying the case of a TM where the incident and transmitted planes are the same, e.g. by focusing input spots on the surface of a microscope cover slide and imaging the same surface. In this situation, the incident field “is” the transmitted field, so $\vec{x}_b = \vec{y}_b$ and consequently $T_{bb} = \mathbb{1}$ and $T_{sb} = R_{sb}$. The resampling matrix could contain low singular values which blow up when computing its inverse. To prevent this from occurring, we compute a pseudoinverse using a Tikhonov regularization [8], which is a popular method when dealing with ill-posed problems. Given a complex matrix H , its singular value decomposition is $H = UDV^\dagger$, where U and V are unitary matrices and D is a diagonal matrix containing the singular values s_i . The Tikhonov regularized pseudoinverse of H is given by

$$H_{\text{Tikh}} = V D_{\text{Tikh}} U^\dagger, \quad (4.5)$$

where D_{Tikh} is a diagonal matrix with entries

$$D_{\text{Tikh},ii} = \frac{s_i}{s_i^2 + \alpha^2}, \quad (4.6)$$

with α the regularization parameter. We choose $\alpha^2 = 0.1$, which is approximately the $(\text{SNR})^{-1}$ in our TMs.

To recap, we can find the TM in a Bessel-to-Bessel basis by first computing the spot-to-Bessel matrix T_{sb} and then multiplying it on the right by R_{sb}^{-1} , which is computed only once in the case of a zero-thickness TM where the incident and transmission planes coincide. The T_{bb} matrix is square with dimensions $(2M \times 2M)$. By using the measured transmitted Airy spots in the resampling process, rather than the calculated spot functions, we not only resample the incident field but also correct for aberrations in the incident field optics.

4.2 Implementation for a zero-thickness reference

Some of the spurious features in the transmission statistics of a zero-thickness reference elucidated in the previous chapter, viz., the pedestal in the singular value histogram and the isotropic spreading of the eigenvalue phase, result from a partially overlapping basis of Airy spots. These effects should disappear if we represent the TM in an orthogonal basis of Bessel modes.

The way we perform the field measurements is exactly the same as described in Chapter 3, by scanning 18 hexagon layers containing a total of 919 points. However, when performing the analysis we select a circular region that is inscribed in the hexagon and the number of spots that lie completely in this circle is 778. Since we assume we are close to critical sampling, we choose 778 as the size of the Bessel basis per polarization component. Consequently the total number of Bessel modes is $2 \times 778 = 1556$. Theoretically, the number of modes of a slab-type sample should be approximately equal to $2\pi A/\lambda^2$, where A is the area of interest and λ is the wavelength of light [2,9]. In our optical setup where we use a 633 nm He-Ne laser, this translates to 2460 modes. However, we don't measure the theoretically predicted full TM because of a finite field of view and a limited numerical aperture of the microscope objectives on either side of the sample. The effective NA of our system is therefore $\sqrt{1556/2460} \approx 0.80$.

Once the transmitted fields have been retrieved, they are decomposed into the 778 Bessel modes and at first we obtain the 1556×1838 rectangular spot-to-Bessel TM, whose magnitude is illustrated in Fig. 4.2(a). In each polarization sub-matrix, every column corresponds to the complex coefficients of the Bessel decomposition for one incident Airy spot. As in the case of the TM in the spot-to-spot basis, the cross-polarization matrices have near-zero amplitude. In the co-polarization matrices, we observe that all Bessel modes contribute for each Airy spot on the hexagonal lattice. However, closer inspection reveals that the higher energy Bessel modes that live on the edge contribute less to the spots than the lower energy ones. The distribution of the corresponding

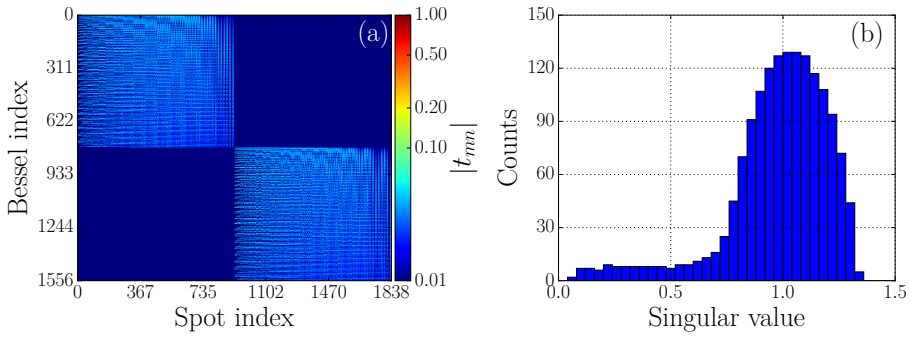


Figure 4.2: (a) Magnitude of the complete spot-to-Bessel TM (logarithmic color scale). (b) Corresponding singular value histogram.

singular values of the spot-to-Bessel TM is shown in Fig. 4.2(b). The histogram resembles the one for the spot-to-spot TM in Fig. 3.6(c), but here there is no pedestal on the right side of the peak. This demonstrates that using the Bessel mode basis eliminates the largest spurious singular values. The tail on the left side of the peak still persists, and the reason for this is that the low singular values result from the high order Bessel modes that contribute less. Truncating the number of modes in the basis would cut this tail, but this would result in an even lower effective NA. Therefore, we do not reduce the number of modes since the high modes still have a non-zero contribution. If there were a singular value peak at zero, that would definitely mean that the associated modes are

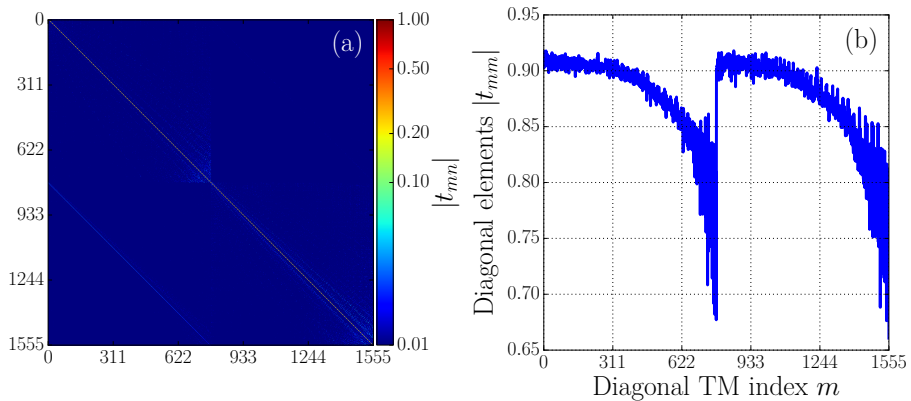


Figure 4.3: (a) Magnitude of the complete Bessel-to-Bessel TM (logarithmic color scale). (b) Magnitude of the diagonal elements $|t_{mm}|$ as a function of the index m .

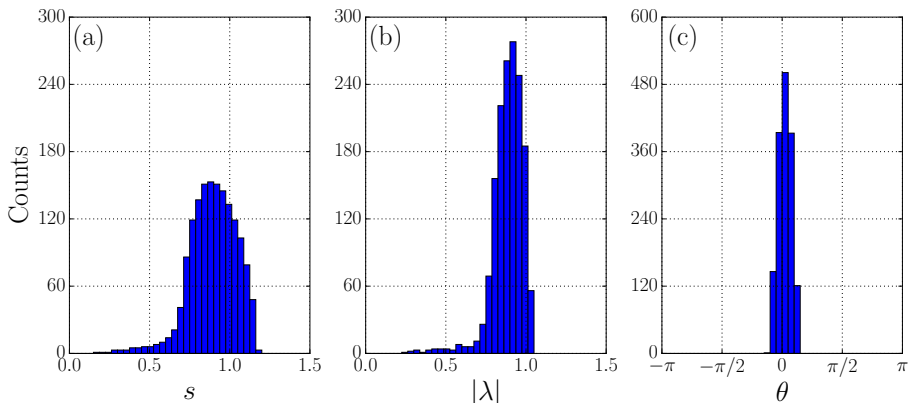


Figure 4.4: Histogram of the (a) singular values, (b) eigenvalue moduli and (c) eigenvalue phases of the complete Bessel-to-Bessel TM of a microscope cover glass.

redundant and we could remove them without lowering the effective NA.

The spot-to-Bessel TM is subsequently converted to a Bessel-to-Bessel TM by resampling the incident spots into a Bessel basis. Here, the Tikhonov regularized pseudoinverse is computed on an independently measured zero-thickness TM so that the noise in the singular vectors does not cancel out. The resampling yields a diagonal matrix containing some noise. The magnitudes of the elements of this Bessel-to-Bessel TM are depicted in Fig. 4.3(a). Here, we get rid of the off-diagonal lines that appeared when using the Airy basis (Fig. 3.5). The faint diagonal visible in the T_{VH} and not in the T_{HV} occurs because of the imperfect polarizing beamsplitter in the optical setup that reflects some stray light. In Fig. 4.3(b), where only the magnitudes of the diagonal elements are plotted, it is clear that the Bessel modes with a low index are more prominent than the higher ones, with the highest ones having an amplitude of about 0.7. The curve repeats itself because the behavior of the diagonal elements is the same for the T_{HH} and T_{VV} submatrices.

The other crucial statistics, viz. the singular values s and eigenvalues λ of the TM, are displayed in Fig. 4.4. We observe that the width of the singular value histogram is larger than that of the eigenvalue histogram. With the Bessel basis, we would expect the statistics of the singular values and eigenvalues to be identical according to eq. (3.17). However, due to the noise of the independently measured TM, T and T^\dagger are not exactly the same and, consequently, the width of the histograms in Fig. 4.4(a) and (b) differ. The slight tail on the left side of the peak occurs because of the smaller contribution of the high index Bessel modes that live mostly on the edge of the measured area. Moreover,

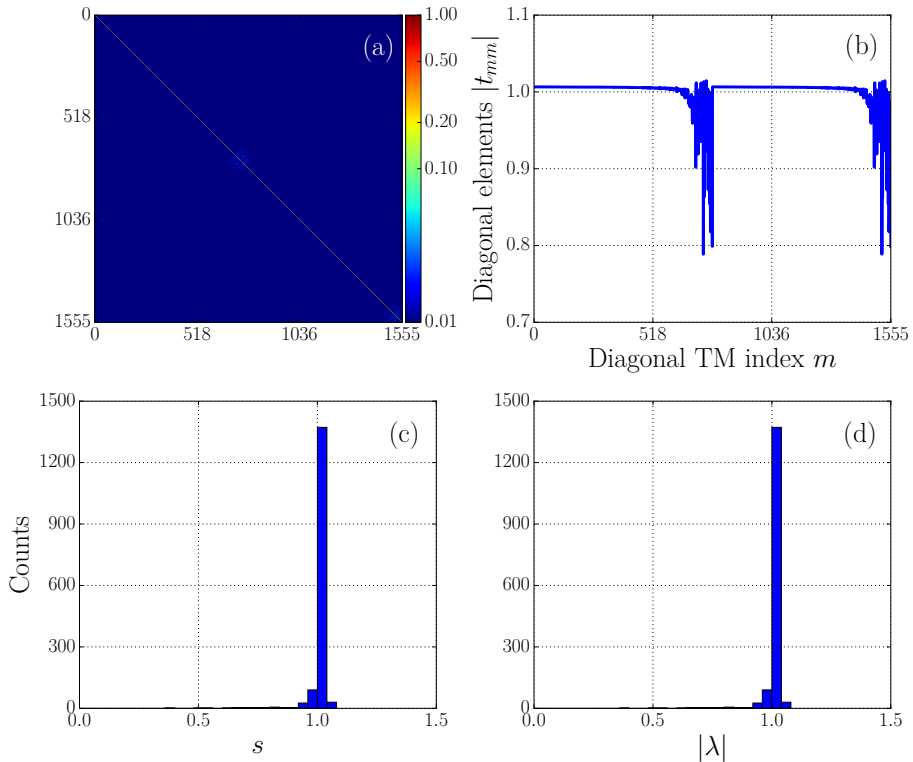


Figure 4.5: (a) Magnitude of TM elements, (b) magnitude of the diagonal elements, (c) singular value distribution and (d) eigenvalue modulus histogram of the simulated zero-thickness TM in the Bessel mode basis.

the major difference with the Airy basis is that the phases of the eigenvalues are not randomized anymore. The phase distribution shown in Fig. 4.4(c) is sharply peaked at 0, implying that the eigenvalues are almost completely real. Hence our resampling procedure, which uses the measured zero-thickness matrix, automatically corrects for the misalignment and aberrations of the optical setup.

The results above show that resampling the transmission matrix in a Bessel mode basis instead of an Airy spot basis removes spurious sampling effects and therefore yields better transport statistics of the sample. It effectively separates the physics of light propagation in the sample from the influence of the measurement and sampling procedure. The final statistics are therefore more accurately comparable to theory, such as random matrix theory [10].

To test our resampling procedure on numerical data, we implement it using

the model developed for the Airy spot basis in Chapter 3. The simulated TM and its statistics are plotted in Fig. 4.5. The matrix is close to being diagonal, as can be seen in (a) and (b), where the magnitude of all elements and only the diagonal ones are plotted respectively. We observe that as in the experimental case the magnitude of the diagonal elements drops off towards the end of each co-polarized submatrix. Therefore, it is not an experimental artefact but indeed an effect of the high index Bessel beams contributing less than lower index ones. However, the diagonal elements drop off less rapidly than in the experiment (Fig. 4.3(b)). Fig. 4.5(c) and (d) show that the singular values and modulus of the eigenvalues are peaked at 1 and nearly identical as expected. The peaks are much narrower in the simulations since the model is noise-free. The eigenvalue phases (not shown) are all zero.

From the good agreement between the experimental results (Fig. 4.4) and the simulated ones (Fig. 4.5), we conclude that the experimental TMs are measured accurately and processed correctly. This validates our method and we can proceed to use it to measure the TM of other samples.

4.3 Transmission eigenvectors of a thin slab of air

The next step is to measure the transmission matrix of a finite thickness of air because that is also relatively simple to simulate. However, an air layer is not a trivial sample because the transmitted fields are sensitive to aberrations of the incident Airy spots and experience diffraction loss due to the high NA of the microscope objectives. Deviations from numerical calculations could reveal any existing non-flatness of the fields and misalignment of the optical setup. The air TM also makes for an interesting study because in cylindrical coordinates its principal modes, which are the eigenvectors of the free space propagator, are Bessel modes. This makes it more relevant to study the eigenvectors and eigenvalues of the air matrix rather than its transmission channels, which only reveal the amount of loss encountered by an incident wave.

In this section, we compare the results for a TM measured in an Airy spot basis and a Bessel mode basis. To perform such a measurement, we move the 0.95-NA microscope objective backward as sketched in Fig. 4.6. The focusing and imaging planes are then separated by the desired thickness of the slab of air.

4.3.1 Airy spot basis

First, we consider the Airy spot basis. We measure the complete 1838×1838 TM (2 incoming and 2 outgoing polarizations) of different thicknesses of air and

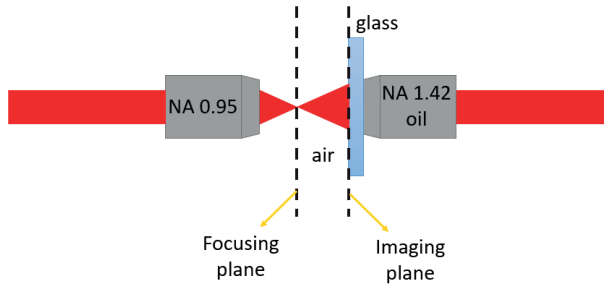


Figure 4.6: Configuration to measure the TM of a finite thickness of air. The 0.95-NA microscope objective is moved back so that the focusing and detection planes are separated by the desired thickness of air.

find interesting and counter-intuitive distributions of the calculated eigenvalues, plotted in Fig. 4.7 for air thicknesses varying from $0\ \mu\text{m}$ to $5\ \mu\text{m}$ in steps of $1\ \mu\text{m}$. There are two outstanding features that can be observed in these spectra. The first distinct feature is that as the thickness of the air slab increases, the eigenvalues start spiraling towards zero. The second feature is that there exists a nonuniform separation between the eigenvalues along the spiral. This becomes progressively more apparent as the air thickness increases.

We can compare the experimental results with the semi-analytical numerical model used earlier. To simulate non-zero thicknesses, the Airy beams are propagated using a Fourier space method [11] to the detection plane, after which the TM in the Airy basis is obtained in the same manner as in the experiment. The assumption here is that both objectives obey the Abbe sine condition [12], which means that they produce sharp images of objects along the optical axis as well as those that are off-axis. Although this assumption might not be entirely valid in our experiment, we can still compare the experimental results to this simple model and see whether there are any similarities.

The complex eigenvalue spectra resulting from the simulation are plotted in Fig. 4.8, and we do observe some stark differences with the experimental ones. In the zero-thickness case, the eigenvalues are all real unlike the random phases observed in the experiment. As discussed in Section 4.2, the randomization is attributed to wavefront aberrations. This major difference for a zero-thickness medium affects the non-zero thicknesses as well, with the spiral evolution hard to compare because of the initial phase distribution and the subsequent spread of amplitudes. Nevertheless, a spiral can still be seen in both the experiment and the simulation. The eigenvalue outliers in the simulation stem from small off-diagonal elements of the TM that appear due to a truncation of the long-tailed Airy fields.

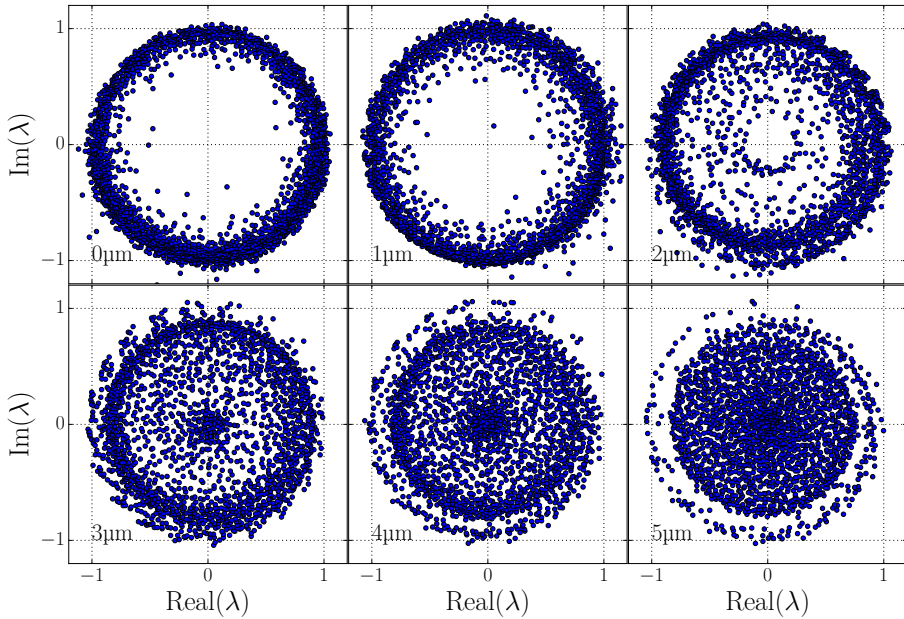


Figure 4.7: Complex eigenvalue spectra of the 1838×1838 complete air TM of thicknesses varying from 0-5 μm in steps of 1 μm .

To understand these salient galaxy-like characteristics better, it is instructive to look at the corresponding eigenvectors. Since propagation of light through air maintains polarization, it is sufficient to look at the eigenvectors of just one submatrix of the complete experimental TM with the same incoming and outgoing polarization. The eigenvalue spectrum and the eigenstates associated to the highest few eigenvalues for an air thickness of 5 μm are plotted in Fig. 4.9. Their spatial profiles are obtained digitally by superposing the transmitted field responses of the incident Airy spots weighted by the appropriate components of the column eigenvectors.

The eigenvector corresponding to the highest eigenvalue is a single spot (Fig. 4.9(b)). This is the fundamental mode of the system. The next two highest eigenvalues are grouped together and the spatial profiles of their eigenvectors are two lobes with a central node (Fig. 4.9(c-d)). The only difference in their spatial profiles is that they have a nearly orthogonal orientation with respect to each other. We see the formation of a trend, with the next three eigenvalues clubbed together (Fig. 4.9(e-g)). Their eigenwaves have three lobes, two nodes and have an approximate 60° orientation with respect to each other.

The modes illustrated in Fig. 4.9 seem to indicate that they are the first few of a larger family of modes. Higher order modes, some of which are depicted

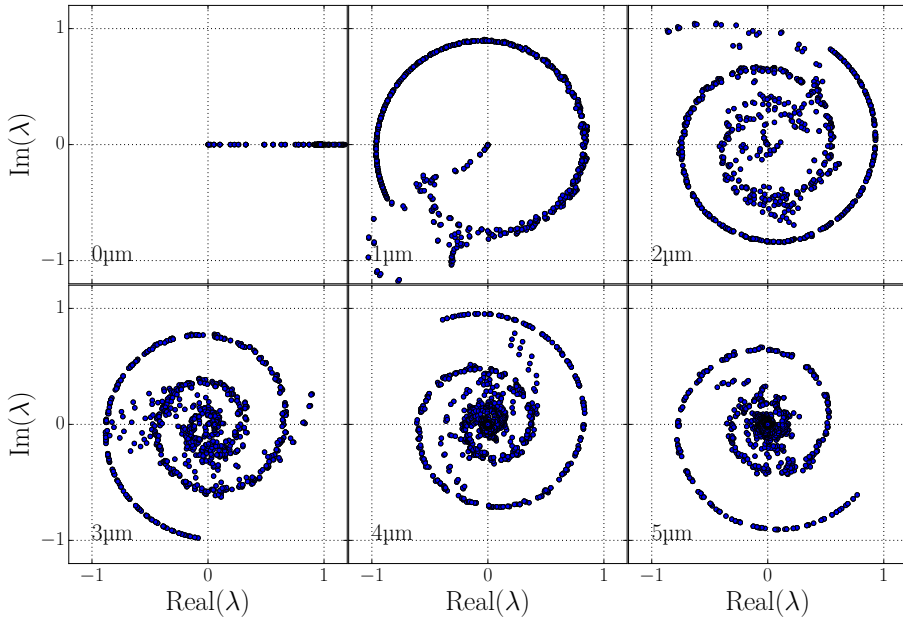


Figure 4.8: Simulated complex eigenvalue spectra of the 1838×1838 complete air TM for various air thicknesses.

in Fig. 4.10, have a larger spatial profile than the first few orders and therefore distortions in their symmetry are more evident. It is in fact observed that the higher the mode order, the more noisy the profile. For some of the highest orders (not plotted here), their spatial profiles are not distinguishable as they are drowned out by the experimental noise.

The family of modes found from the TM of an air slab with a thickness of $5 \mu\text{m}$ are neither Hermite-Gaussian nor Laguerre-Gaussian because all modes don't possess rectangular or circular symmetry respectively. The modes closely match a continuous transition between Laguerre-Gaussian and Hermite-Gaussian modes, known as Ince-Gaussian modes [13, 14]. These modes form a complete set of modes that fulfill the paraxial wave equation and exhibit inherent elliptic symmetry. Additionally, they are the eigenmodes of an astigmatic cavity [14].

The Ince-Gaussian beams have certain properties which explain the spiraling eigenvalue plots. First, they possess a Gouy phase which is a function of the mode order. This means that different modes experience a different phase shift as they propagate through air. We understand therefore the bunching of the eigenvalues of the same order. Ideally, degenerate modes of the same order must share the same eigenvalue. However, although we do observe the bunching of the experimental eigenvalues in Fig. 4.9, they do not overlap in the complex plane.

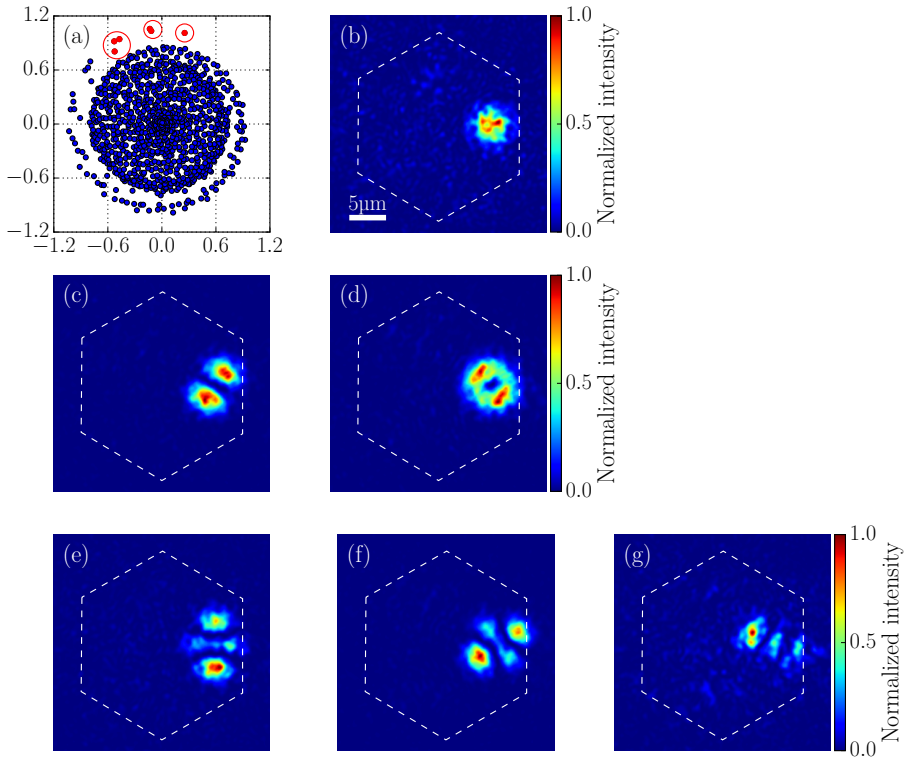


Figure 4.9: (a) Complex eigenvalue spectrum for the T_{HH} sub-matrix of a 5 μm -thick air layer. The x - and y -axes represent the real and imaginary axes respectively. The eigenstates of the eigenvalues highlighted in red are plotted in (b-g). Normalized intensity of the (b) fundamental, (c,d) first order and (e-g) second order eigenvectors. The different orders are encircled in (a). The dashed hexagon in the eigenvector images demarcates the TM measurement area. All intensity images have the same scale bar.

On the other hand, the eigenvalues are very close together in the simulation. We conclude that aberrations or other imperfections lift the degeneracy of the experimental eigenvalues.

The second relevant property of the Ince-Gaussian beams is that the spatial profile of the modes grows in size as the mode order increases. Consequently, for large modes, some part of their profile falls outside the region where the TM is measured. This is clearly visible in Fig. 4.10, where the spatial profile of some higher order modes spills over the delineated hexagonal measurement area. The extent that crosses the boundary is not taken into account when generating the

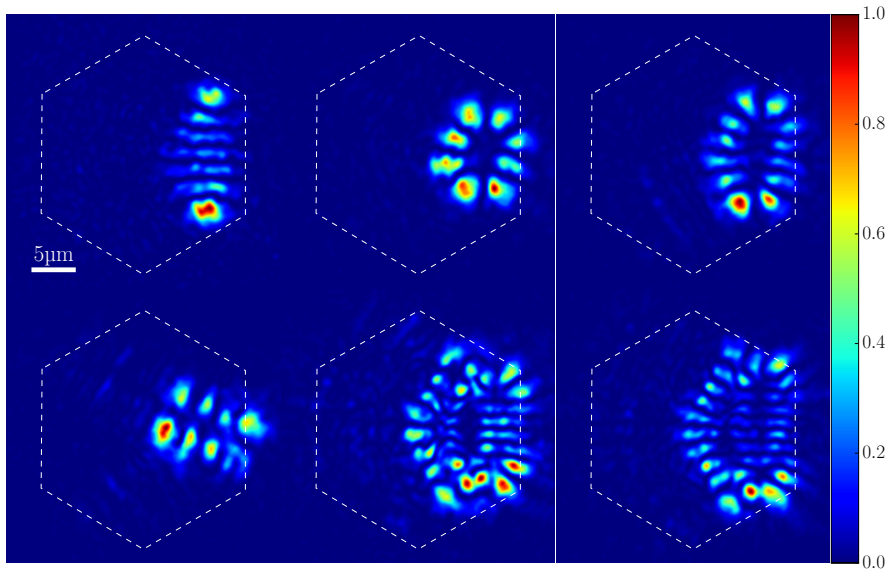


Figure 4.10: Normalized intensity of selected higher order Ince-Gaussian eigenstates of a $5 \mu\text{m}$ air TM. The dashed hexagons represent the borders of the measurement area. The scale bar applies to all figures.

TM, and its information is consequently lost. This loss in turn is translated as a reduced amplitude of the eigenvalue. Hence, the eigenvalue amplitude decreases as the mode order increases and thereby elucidates the inward spiraling of eigenvalues towards zero. Furthermore, an increased thickness of the air slab entails a larger propagation distance and thereby a more expanded spatial profile. This explains why the eigenvalue plots of larger air slabs experience more loss and spiral more quickly to zero than smaller thicknesses (Fig. 4.7). Since a misaligned setup will endure more losses than an aligned one, the rate at which the eigenvalues spiral towards zero is an indicator of the alignment and aberrations of the optical setup.

There are a couple of other points to note about the complex eigenvalue plot. The direction of rotation of the spiral is simply a consequence of the phase convention that is used when recovering the light field using digital holography. If the sign of the phase is flipped, the spiral will spin the other way. The second remark is that all the modes that are displayed in Fig. 4.9 and Fig. 4.10 are off-centered and lie on the right side of the measured area. This is caused by the asymmetry in the aberrations of the optical system.

The numerical eigenvectors of a zero thickness air slab are calculated and some

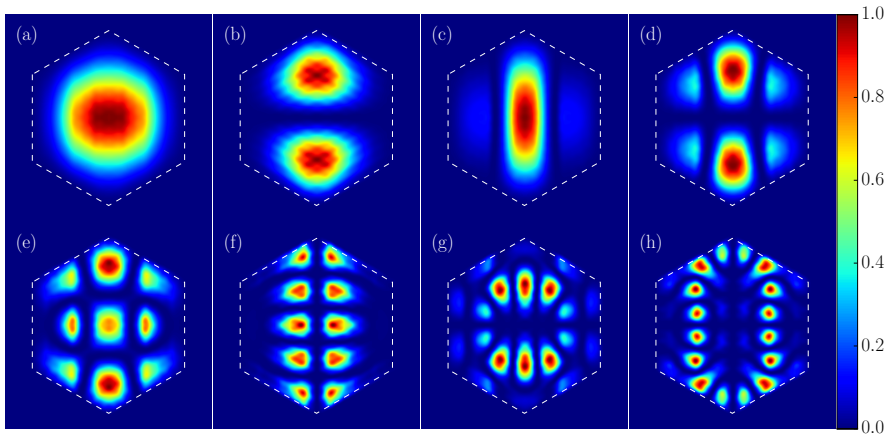


Figure 4.11: Normalized intensity profile of some simulated eigenstates of the T_{HH} submatrix of a zero thickness air TM in the Airy spot basis. (a) Fundamental mode. (b, c) First and second order modes. (d-h) Some higher order modes. The dashed hexagon represents the area encompassing the incident focused fields.

of them are shown in Fig. 4.11¹. The fundamental mode (a), first (b) and second order modes (c) resemble in shape to the ones measured in our experiment. The higher order modes (d-h) also agree well with our measurements and exhibit elliptical symmetry. However, they occupy the entire hexagon in the simulation while they are restricted to one side in the experiment. The reason for this is the absence of aberrations in the numerical simulation.

4.3.2 Analogy with Fox-Li modes of a cavity with finite mirrors

The family of modes found in our system is reminiscent of the resonant modes inside a laser cavity [15]. In fact the Ince-Gaussian modes have experimentally been found in a resonator where the symmetry was intentionally broken by shifting the output coupler sideways [16]. The other interesting remark about our spiral eigenvalue plot is that a similar plot was first found numerically by Cochran and Hinds [17] (see Fig. 4.12) for the eigenvalues of the Fox-Li operator to compute the modes in a cavity with finite mirrors [5]. The mathematical analysis of the spiral shape is still an area of active research as there has been recent interest in studying approximations of the eigenvalue spectrum of the

¹The thickness is chosen as zero because the modes are best visualized for this thickness. For higher thicknesses, the profiles of the modes don't change by definition of eigenvectors, but because of the effects of the long-tailed Airy fields in the simulations, they are more distorted.

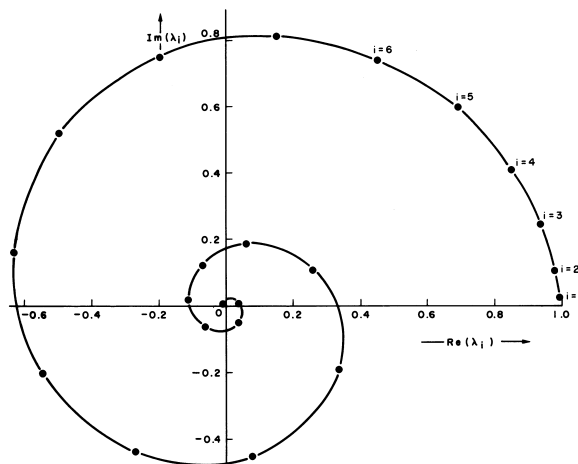


Figure 4.12: Eigenvalues of the Fox-Li operator for computing the modes in a cavity with finite mirror size. Figure reproduced from the paper by Cochran and Hinds [17].

Fox-Li operator [6]. We therefore explore the analogy between the TM setup and the Fox-Li modes of an asymmetric cavity.

To make the analogy between a TM system and a cavity more concrete, let us consider a confocal cavity as sketched in Fig. 4.13. In a confocal cavity, the field on the curved surface of Mirror 2 is the Fourier transform of the field on the surface of Mirror 1, and vice versa [18]. Mirror 1 can then be treated like the “real” plane and Mirror 2 as the “Fourier” plane. Since the mirrors are finite in size, Mirror 1 acts like a real space filter and Mirror 2 as a Fourier filter because we have no access to fields that miss the mirrors. The analogy with the TM setup now becomes more direct because in that case too, there is a real space filter given by the finite field of view and a Fourier space filter given by the finite numerical aperture of the microscope objectives.

We can in fact make a direct relation between the transmission operator and the Fox-Li operator. The transmission operator \hat{T} can be expressed as

$$\hat{T} = T_2 T_{\text{air}} T_1, \quad (4.7)$$

where T_1 and T_2 are filtering operators by objectives 1 and 2 respectively. The eigenvectors \mathbf{v} of \hat{T} therefore satisfy the eigenvalue equation

$$T_2 T_{\text{air}} T_1 \mathbf{v} = \lambda \mathbf{v} \quad (4.8)$$

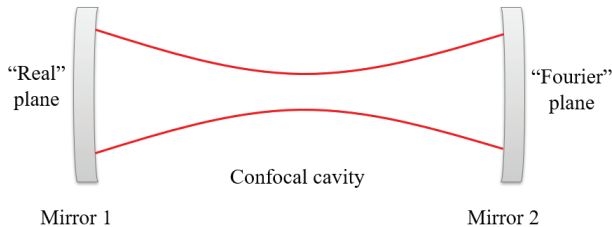


Figure 4.13: Confocal cavity. Mirror 1 acts as the “real” plane and Mirror 2 acts as the “Fourier” plane. The red lines correspond to the outline of a resonant beam in the cavity.

with λ the eigenvalue. This leads to

$$(T_2 T_{\text{air}} T_1) (T_2 T_{\text{air}} T_1) \mathbf{v} = \lambda^2 \mathbf{v}. \quad (4.9)$$

If we introduce $\mathbf{w} = T_1 \mathbf{v}$ and multiply both sides of the equation by T_1 from the left, we have

$$(T_1 T_2 T_{\text{air}}) (T_1 T_2 T_{\text{air}}) \mathbf{w} = \lambda^2 \mathbf{w}. \quad (4.10)$$

Renaming $T_1 T_2 = M$ and $\lambda^2 = \alpha$, we can simplify the physics of the transmission operator to

$$(M T_{\text{air}}) (M T_{\text{air}}) \mathbf{w} = \alpha \mathbf{w}. \quad (\text{transmission modes}) \quad (4.11)$$

On the other hand, in the case of the confocal cavity, if we describe Mirrors 1 and 2 as the operators M_1 and M_2 , the eigenvectors \mathbf{w} for one round trip of the cavity with eigenvalue α obey

$$(M_1 T_{\text{air}}^{21}) (M_2 T_{\text{air}}^{12}) \mathbf{w} = \alpha \mathbf{w}, \quad (\text{Fox-Li modes}) \quad (4.12)$$

where T_{air}^{12} and T_{air}^{21} represents propagation through air from Mirror 1 \rightarrow 2 and from Mirror 2 \rightarrow 1 respectively. For air we have $T_{\text{air}}^{12} = T_{\text{air}}^{21} = T_{\text{air}}$, and by comparing eqs. (4.11) and (4.12), we notice that if $M_1 = M_2 = M$ the transmission and Fox-Li eigenmodes satisfy identical equations and consequently experience similar physics. In other words, predictions and experimental observations made from the TM T of any medium that fulfils the reciprocity relation $T^{12} = T^{21}$ can be mapped onto a confocal cavity with identical and possibly imperfect mirrors filled with the same medium; and vice versa. For example, given the principal modes of an optical fiber [19,20], it is possible to construct a confocal resonator that has the exact same mode structure.

The process of computing the eigenmodes between the mirrors in the res-

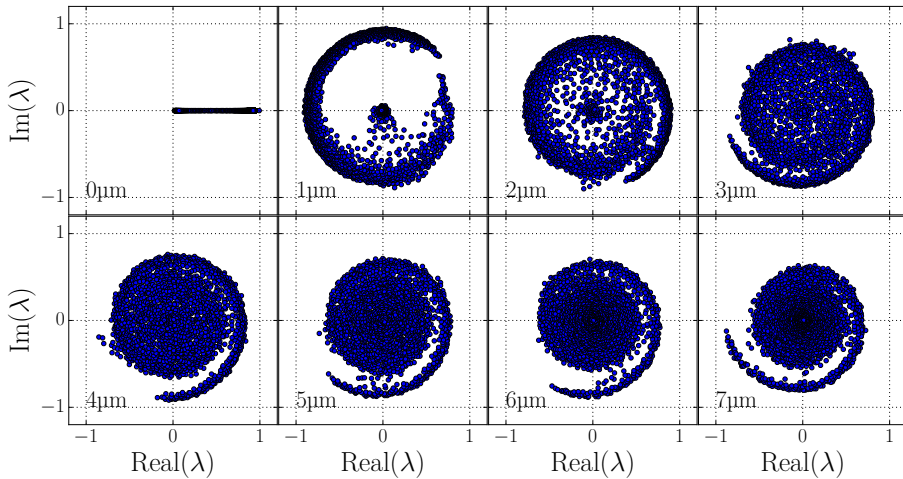


Figure 4.14: Complex eigenvalue spectra of the 1556×1556 complete experimental air TM in the Bessel mode basis. The air thicknesses range from 0-7 μm in steps of 1 μm .

onator is similar to calculating the eigenstates of the TM. Additionally, the mode at the end of N round trips is accompanied with an eigenvalue α^N . Since we have $0 \leq |\alpha| \leq 1$ without a gain medium in the cavity, the eigenvectors with smaller eigenvalues disappear more rapidly as the number of round trips N increases. The loss encountered for every round trip in the cavity is attributed to higher order modes more than lower order ones. In this regard, the cavity is similar to the TM setup where high order modes fall outside the region of interest. With a greater air slab thickness, the high order modes rapidly obtain very small eigenvalues and only the low order modes survive. The choice of thickness of the air slab is thereby a suitable method to achieve mode filtering.

4.3.3 Bessel mode basis

The illumination and imaging part of our experimental setup is ideally cylindrically symmetric because we have microscope objectives with circular apertures. We know that the eigenvectors of propagation in free space of a cylindrically symmetric system, e.g., an optical fiber, are the Bessel modes [2]. Therefore, we study the eigenwaves of the air matrix in a Bessel mode basis². As in the

²We note that the resampling procedure is not a unitary basis transformation. A unitary transformation leaves the eigenvalues strictly unmodified. Instead, our resampling procedure removes some optical aberrations and reduces the size of the matrix. It is therefore a non-unitary and lossy procedure.

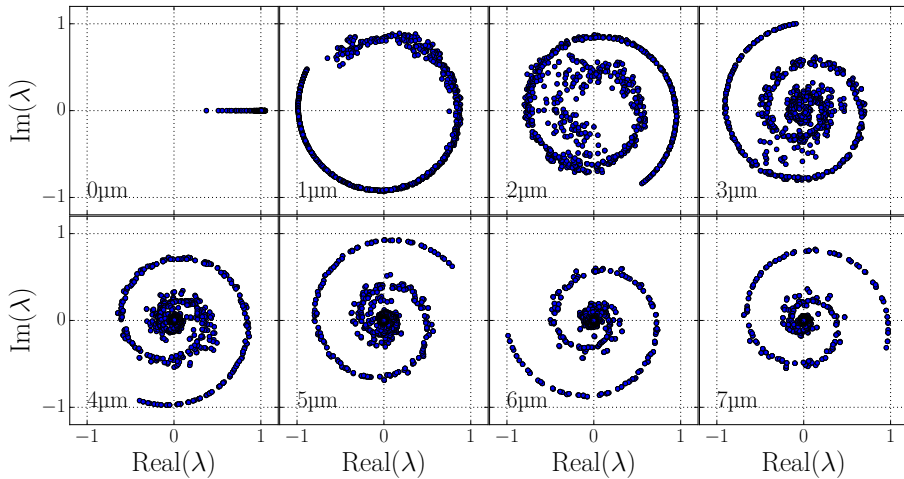


Figure 4.15: Evolution of the simulated eigenvalue spectra of the TM in the Bessel basis as a function of the thickness of the air layer, indicated at the bottom left corner of each subplot.

previous section, we use 778 Bessel functions per polarization, resulting in a total of 1556 modes.

The eigenvalue spectra for thicknesses up to $7\ \mu\text{m}$ are plotted in Fig. 4.14. Unlike the eigenwaves in the Airy basis, the eigenvalues are less bunched and the center of the spiral is filled more uniformly for larger thicknesses. The evolution of the spiral is also more evident since the phases are initially zero and then gradually spread out as the modes propagate through air.

We can compare these spirals with simulated ones, plotted in Fig. 4.15, where the thicknesses range from 0 to $7\ \mu\text{m}$ in steps of $1\ \mu\text{m}$. As in the experiment, the eigenvalues are initially real and then spiral inward gradually with increasing thickness. The spirals here begin at different points because the modes pick up a global phase $\phi = -2\pi d/\lambda$ depending on the distance d they travel through air³. This is not the case for the experimental matrices because those matrices are measured at different times and their global phase is random due to phase drifts. The eigenvalues at the inner end of the spiral, corresponding to the higher order modes, are noisier than those at the start of the spiral. This confirms that the high order eigenvectors living primarily on the boundaries of the defined area suffer from edge effects and losses. We note that the simulated eigenvectors are similar in both bases. They would be identical if both bases were complete and orthogonal, but we have shown in Chapter 3 that the spot basis is not exactly

³The minus sign originates from our phase convention $e^{-i\phi}$ for the argument of the complex field.

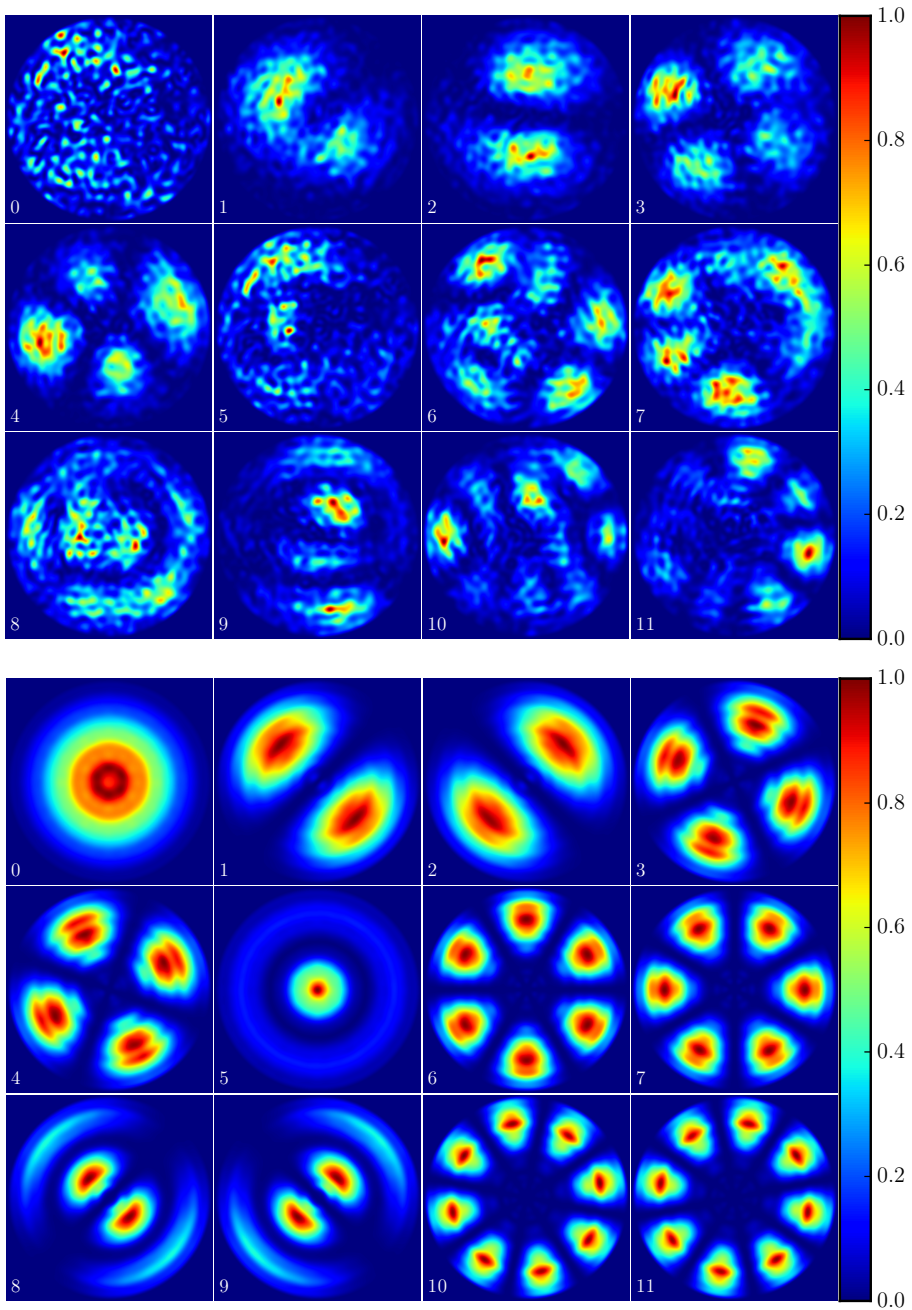


Figure 4.16: Normalized intensity of the experimental (top) and simulated (bottom) eigenvectors with the largest eigenvalues of the T_{HH} submatrix for a 5 μm -thick air layer. The eigenvectors correspond to the top 12 eigenvalues with the index indicated at the bottom left corner of every subplot.

orthogonal.

It is again insightful to look into the corresponding eigenstates. For the zero-thickness case, the TM in the Bessel basis is nearly diagonal. Hence, the eigenvectors must be Bessel modes as a consequence of the TM construction procedure. However, with increasing thickness, the TMs are not solely diagonal anymore and this implies that the Bessel modes start mixing. The intensity of the experimental and simulated eigenvectors associated to the highest eigenvalues for an air slab of $5\ \mu\text{m}$ are depicted in Fig. 4.16. It is noteworthy that in the experimental case, the TM in the Bessel basis is constructed from the same data set as the TM in the Airy basis in Section 4.3.1. The numerical eigenvectors in the Bessel basis are, unsurprisingly, Bessel modes. It is clear that the experimental ones resemble the simulations but are noisy and distorted. The higher order modes (not shown) are affected by mode mixing and loss (low eigenvalues) and can't be recognized anymore. Nonetheless, the main contrast with the Airy basis is that we don't observe any Ince-Gaussian modes. This is crucial because the real principal modes of air are the Bessel modes, and the TM in this basis does provide these states. The other notable feature is that the eigenmodes here fill the entire measurement area and are centered whereas those in the spot basis occupy only a fraction of the area and are located to one side.

It is still important to note that the TM in the Airy spot basis is useful. First, it is more straightforward to obtain and yet does not yield wildly deviating statistics. Second, it accounts for system imperfections and should consequently not be discarded. It is in fact meritorious to use such a TM and its Tikhonov inverse for imaging and projecting fields through the setup because misalignment has already been taken care of [21].

4.4 Conclusion

We performed TM measurements in a Bessel mode basis for two known reference systems: a zero-thickness medium and a thin slab of air. The results obtained for the TM of a zero-thickness cover slide are in good agreement with numerical calculations and hence validate the resampling procedure.

Furthermore, when using an Airy basis, we have shown that the measurement of the TM of a finite thickness of air is an excellent way to gauge the accuracy and precision of a TM measurement and of misalignment in the optical setup. Moreover, we found that the resulting transmission eigenvectors are the Ince-Gaussian modes and they possess eigenvalues that spiral inwards on the complex plane. The spiral shape was explained by the different loss experienced by individual modes of the system. We observed that the spiral decays more rapidly

towards zero for greater propagation distances in air, effectively making the air thickness a suitable parameter to filter out higher order modes. Finally, we presented a direct analogy of the transmission eigenvectors of air with the Fox-Li modes of a lossy confocal cavity with finite mirrors. This demonstrates the mathematical link between cavity physics and a transmission matrix approach.

Finally we concluded that the TM in the aberration-corrected Bessel basis decouples the eigenmodes of the entire optical system from those of the sample, and this is indispensable when attempting to understand the physics of transmission channels.

Bibliography

- [1] R. W. Robinett, “Quantum mechanics of the two-dimensional circular billiard plus baffle system and half-integral angular momentum,” *European Journal of Physics* **24**, 231–243 (2003).
- [2] B. Saleh and M. Teich, *Fundamentals of Photonics*, Wiley Series in Pure and Applied Optics (Wiley, 2007).
- [3] S. Janke, “Solving the Schrödinger equation for infinite potential wells,” Ph.D. thesis (2017).
- [4] S. Franke-Arnold and N. Radwell, “Light served with a twist,” *Opt. Photon. News* **28**, 28–35 (2017).
- [5] A. G. Fox and T. Li, “Resonant modes in a maser interferometer,” *The Bell System Technical Journal* **40**, 453–488 (1961).
- [6] A. Böttcher, H. Brunner, A. Iserles, and S. P. Nørsett, “On the singular values and eigenvalues of the Fox–Li and related operators,” *New York J. Math* **16**, 539–561 (2010).
- [7] Y. C. Eldar, *Sampling Theory: Beyond Bandlimited Systems* (Cambridge University Press, 2015).
- [8] A. N. Tikhonov, “Solution of incorrectly formulated problems and the regularization method.” *Sov. Math., Dokl.* **5**, 1035–1038 (1963).
- [9] A. Mosk, A. Legendijk, G. Lerosey, and M. Fink, “Controlling waves in space and time for imaging and focusing in complex media,” *Nature photonics* **6**, 283–292 (2012).
- [10] C. W. J. Beenakker, “Random-matrix theory of quantum transport,” *Rev. Mod. Phys.* **69**, 731–808 (1997).
- [11] J. Goodman, *Statistical Optics*, A Wiley-Interscience publication (Wiley, 1985).
- [12] E. Abbe Hon., “VII.—On the estimation of aperture in the microscope.” *Journal of the Royal Microscopical Society* **1**, 388–423 (1881).
- [13] M. A. Bandres and J. C. Gutiérrez-Vega, “Ince–Gaussian beams,” *Opt. Lett.* **29**, 144–146 (2004).
- [14] M. A. Bandres and J. C. Gutiérrez-Vega, “Ince–Gaussian modes of the paraxial wave equation and stable resonators,” *J. Opt. Soc. Am. A* **21**, 873–880 (2004).
- [15] H. Kogelnik and T. Li, “Laser beams and resonators,” *Appl. Opt.* **5**, 1550–1567 (1966).
- [16] U. T. Schwarz, M. A. Bandres, and J. C. Gutiérrez-Vega, “Observation of Ince–Gaussian modes in stable resonators,” *Opt. Lett.* **29**, 1870–1872 (2004).
- [17] J. A. Cochran and E. W. Hinds, “Eigensystems associated with the complex-symmetric kernels of laser theory,” *SIAM Journal on Applied*

- Mathematics **26**, 776–786 (1974).
- [18] G. D. Boyd and H. Kogelnik, “Generalized confocal resonator theory,” *The Bell System Technical Journal* **41**, 1347–1369 (1962).
- [19] S. Fan and J. M. Kahn, “Principal modes in multimode waveguides,” *Opt. Lett.* **30**, 135–137 (2005).
- [20] W. Xiong, P. Ambichl, Y. Bromberg, B. Redding, S. Rotter, and H. Cao, “Principal modes in multimode fibers: exploring the crossover from weak to strong mode coupling,” *Opt. Express* **25**, 2709–2724 (2017).
- [21] S. Popoff, G. Lerosey, M. Fink, A. C. Boccara, and S. Gigan, “Image transmission through an opaque material,” *Nature Communications* **1**, 81 (2010).

5 Mesoscopic correlations in transmission matrices of strongly scattering media

In physics, we usually classify nature in the macroscopic and the microscopic realm. The macroscopic world deals with objects we can see with our eyes, while the microscopic world, as its name suggests, describes matter at the microscopic or atomic level. Mesoscopic physics is the field that bridges these two worlds and where microscopic effects or fluctuations are noticeable in the macroscopic properties of the object. Specifically, in mesoscopic wave physics, we consider length scales which are longer than the transport mean free path and shorter than the coherence length [1].

Light transport in complex media exhibits mesoscopic correlations and is therefore a hot topic of current research [2–18]. The transmission channels of a multiple scattering medium are the building blocks for light transport in the medium and lie therefore at the heart of mesoscopic phenomena. Since the singular values of the transmission operator (TO) represent the transmission coefficients of the individual channels, measurements of its matrix representation, the transmission matrix (TM), enable the exploration of the distribution of the transmission channels [19–21].

One quantity that exhibits mesoscopic fluctuations is the dimensionless conductance of a medium, which is the analogue of electrical conductance in mesoscopic wires [1, 22–26]. The optical signatures of these universal fluctuations have first been observed experimentally by Scheffold and Maret [27]. Fluctuations of the dimensionless conductance are also reflected in the speckle intensity statistics, which deviate from a negative exponential law [1]. The deviation is stronger when the incident wave couples to fewer transmission channels, and this has recently been observed in optical and microwave experiments [28–31]. Since every channel of the TO of a medium is orthogonal by definition to the other channels, this raises the research question as to what occurs to the dimensionless conductance when an incident field couples to a single channel of the medium, analogous to an Anderson-localized system that supports only one mode [31–33]. To answer such a question experimentally, the channels of the

measured TM, which is always a partial representation of the TO [34,35], must be an accurate representation of the channels of the TO. It is therefore crucial that the largest possible fraction of the TM must be measured precisely and accurately without inducing spurious correlations from the optical system or the sampling method. This challenge was tackled extensively in Chapters 3 and 4.

In this chapter we aim to explore the statistics of individual channels by measuring the transmission matrices of strongly scattering media, consisting of zinc oxide nanoparticles, where the transport mean free path is comparable to the wavelength of the incident light field. We gauge the quality of the experimental distribution of the singular values by comparing it to the predicted one for a multiple scattering slab waveguide, which is a bimodal distribution known as the Dorokhov-Mello-Pereyra-Kumar (DMPK) curve [36,37]. We then investigate the speckle statistics of the individual channels to study whether they show signs of mesoscopic correlations.

5.1 Methods

5.1.1 Sample preparation

The samples used in this chapter are thin layers of zinc oxide (ZnO) nanoparticles with a diameter of 90-200 nm. The recipe to prepare them is taken from the PhD thesis of Vellekoop [38]. The nanoparticles, obtained commercially, are first diluted in distilled water (2.5 g ZnO in 8 mL H₂O). They are then mounted on a rotating vial holder and left to mix overnight, resulting in a homogeneous white solution. The liquid is subsequently poured into a spray gun and sprayed by hand on a standard microscope cover glass that has previously been plasma-cleaned for a few minutes. The layer is then left to dry for a day so that the water evaporates.

The thickness of the sample depends on the duration of the spraying process. Moreover, since the spraying is performed by hand, the thickness is not uniform and varies. To make the surface flat to within a particle size of 200 nm, we shave the sample using the doctor blade technique [39], where a razor blade mounted at an angle on a 3D stage is moved horizontally across the substrate surface. This gives us a constant thickness within our field of view, which is around 30 μm \times 30 μm . Nonetheless, since the blade is not perfectly parallel to the glass substrate, we obtain a slow thickness gradient along the sample, as depicted in the photograph in Fig. 5.1. This allows us to identify several ZnO thicknesses on the same physical sample.

The scattering mean free path of similarly fabricated samples lies between 500-900 nm [40], which is comparable to the wavelength of 633 nm of our He-Ne

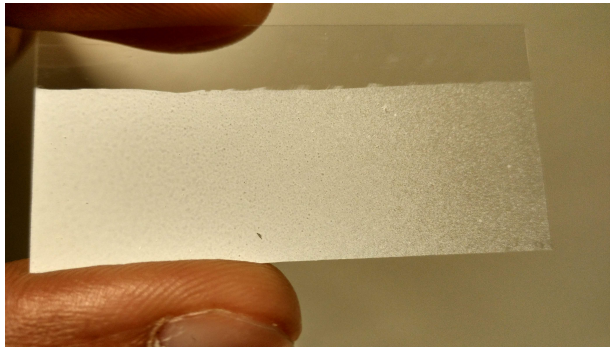


Figure 5.1: Photograph of a typical ZnO sample.

laser. Moreover, the scattering layer is isotropic and the ensemble-averaged statistics of such samples can be studied with diffusion theory. Since the sample is formed of ZnO nanoparticles with a certain filling fraction in air, we can describe it as an effective medium constituting of ZnO and air with an effective refractive index n_{eff} . The effective refractive index of these samples is about $n_{\text{eff}} = 1.4$ [41], resulting from a nearly equal filling ratio between ZnO nanoparticles with a refractive index of about 2 and air with a refractive of 1. The mean transmission through such samples is given by

$$\langle \mathcal{T} \rangle = \frac{z_i + z_{e1}}{L + z_{e1} + z_{e2}}, \quad (5.1)$$

where L is the sample thickness, z_i is the injection depth and z_{e1} and z_{e2} are the extrapolation lengths on the front and back surface of the sample, respectively. For our ZnO samples with $n_{\text{eff}} = 1.4$, the reported values for the extrapolation lengths are $z_{e1} = 1.96\ell_t$ and $z_{e2} = 0.68\ell_t$, and the injection depth for a NA of 0.95 of the microscope objective is calculated to be $z_i = 0.87\ell_t$, with $\ell_t = 700 \pm 200$ nm the transport mean free path [42]. In this chapter, we use a sample with a thickness $L = 10.1 \pm 0.2 \mu\text{m}$, corresponding to an average transmission $\langle \mathcal{T} \rangle = 0.166 \pm 0.024$ from the air to the glass side. The thickness is measured optically by focusing the objectives on the front and back surface of the sample according to the auto-focusing procedure outlined in Section 3.B.1.

5.1.2 TM measurement

We measure the TM of a ZnO sample by first sampling Airy disks on a hexagonal lattice at the Rayleigh criterion (Chapter 3) and then resampling the spot basis in a Bessel mode basis (Chapter 4). We choose the Bessel mode basis since it is almost perfectly orthogonal and complete on a finite circular area. In this way,

we minimize spurious sampling crosstalk and retrieve accurate statistics of the transport physics of the sample. All four polarization components of the TM are measured, viz., T_{HH} , T_{HV} , T_{VH} and T_{VV} , where H and V stand for horizontally and vertically polarized light in the objective's pupil respectively and the order of the letters indicate the incident and transmitted polarization component. The dimension of the individual submatrices is 778×778 and that of the complete TM is therefore 1556×1556 . We choose the TM to be square even though the NA of our objectives is not equal because we would like to interpret our results in the light of the reference case of a clear sample, where we carefully suppressed sampling crosstalk (Chapters 3, 4). Furthermore, the objectives might not fulfil the Abbe sine condition for higher spatial frequencies and could thus introduce spurious correlations. The individual polarization submatrices are combined in the following way to form the polarization-complete TM [43]

$$T = \begin{pmatrix} T_{HH} & T_{VH} \\ T_{HV} & T_{VV} \end{pmatrix}.$$

The outstanding features of our investigation is that we *combine* high numerical aperture (NA), a complete polarization set, systematic sampling (using a clear reference), a well-defined strongly scattering medium, low noise and phase stability in our TM measurement procedure. Hence we obtain a faithful representation of the statistics of the TO.

5.2 Singular value distribution

The singular values of the TM of a sample correspond to the transmittance of its transmission channels, and hence we can study the distribution of the channels by looking at the statistics of the singular values. The singular value histograms of the individual polarization submatrices of a ZnO sample with a thickness of $10.1 \pm 0.2 \mu\text{m}$ are shown in Fig. 5.2. The singular values are normalized with respect to the average transmission through a zero-thickness sample (see Section 3.4). The distribution for the co- and cross-polarized sub-matrices look alike, indicating that the polarization of the initial state is completely randomized. This is as expected since the transmission channels undergo multiple scattering events given that the sample is close to 15 mean free paths in thickness. Furthermore, we find a large number of closed transmission channels with singular values close to zero. The probability of finding channels with higher transmission decreases more or less linearly with increasing singular values up to 0.55. This corresponds to a maximum transmittance of about 0.3, which is nearly twice as large as the mean transmittance $\langle \mathcal{T} \rangle = 0.166$ of the sample. This is quite remarkable since $\langle \mathcal{T} \rangle$ includes both transmitted polarizations.

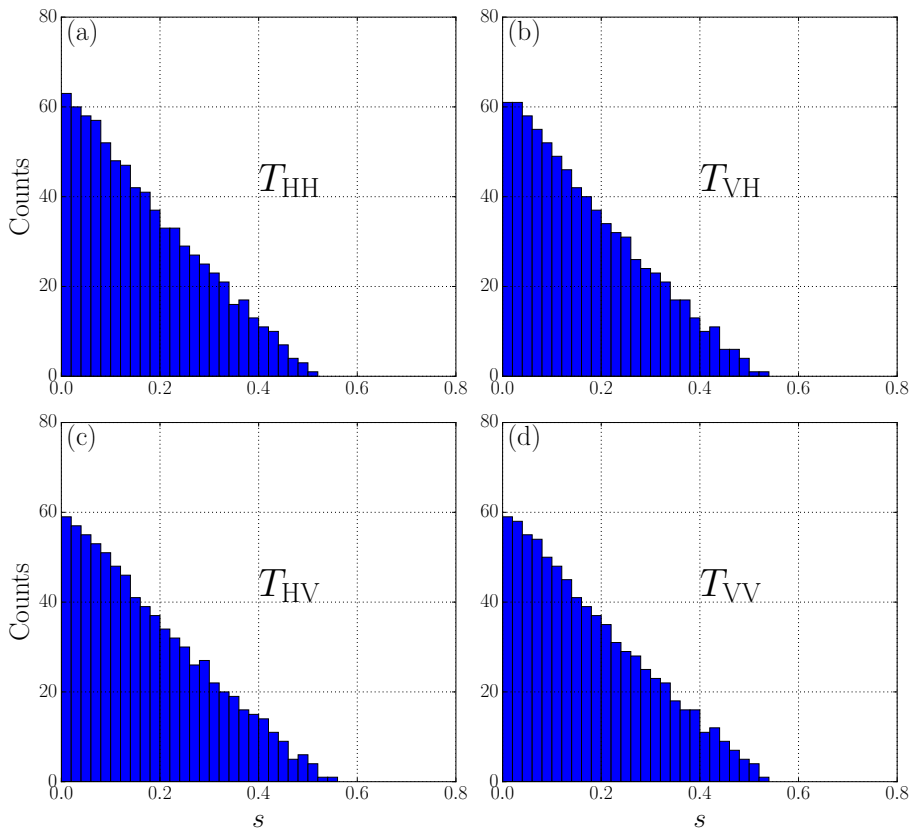


Figure 5.2: Singular value histograms of the (a) T_{HH} , (b) T_{VH} , (c) T_{HV} and (d) T_{VV} submatrices of the TM of a ZnO sample.

Next, we study the transmission statistics of the complete TM containing all its polarization submatrices, with the main results summarized in Fig. 5.3. In Fig. 5.3(a), we notice that the distribution of the complete TM is more convex than those of the polarization submatrices. We also observe that the maximum singular value is 0.7 and larger for the combined matrix than the value 0.55 observed for the individual matrices. The same data is visualized as a transmittance distribution in Fig. 5.3(b), where the histogram of the squared singular values s^2 is plotted. The transmittance represents the intensity transmitted through the sample by the different channels. The dashed line represents the theoretical threshold of $2/3$ above which transmission channels are conventionally referred to as “open” (see Section 2.4). However, we don’t observe any transmittance close to that threshold since we measure experimentally only a fraction of the true complete TM and also do this for a relatively thick sam-

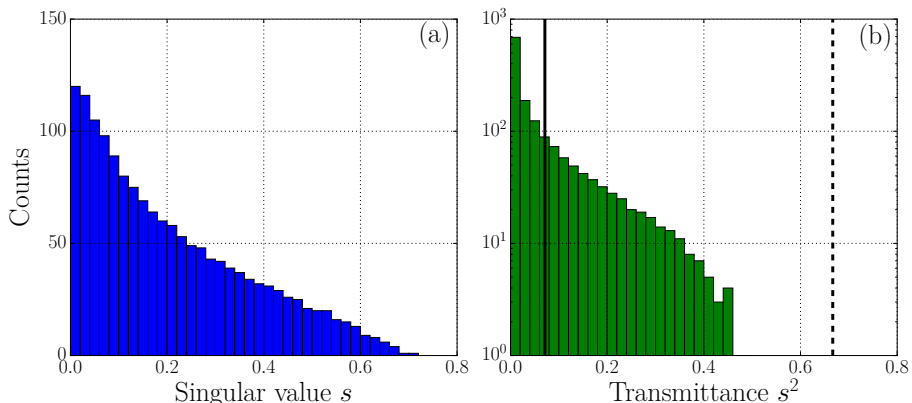


Figure 5.3: (a) Singular value s and (b) transmittance s^2 histograms of the complete TM of the ZnO sample. The dashed vertical line is the theoretical transmittance of $2/3$ above which transmission channels can be called open. The solid line indicates the average transmittance of the measured TM.

ple where we encounter more losses than for a thin layer. The distribution ends abruptly and the highest transmitting channels that we find have a transmittance of 46%, which is almost three times as transmissive as the predicted average $\langle \mathcal{T} \rangle = 0.166$.

Our goal is to obtain accurate statistics from measured TMs that are large enough so that we can observe mesoscopic effects. We do not optimize the transmitted intensity per se but, as a figure of merit, we still compare our transmission to values reported in literature. Our maximum transmission of 46% retrieved from the TM data is smaller than the value of 65% observed by Yu *et al.* [35] for a sample with a similar thickness. To the best of our knowledge, that is the largest transmittance value ever reported through a strongly scattering medium. However, sampling crosstalk was not dealt with explicitly in that work, whereas we have shown that our data minimizes the influence of the sampling procedure (Chapters 3 and 4). Our observed transmittance of 46% is higher than some other reported values in literature, such as 31% by Vellekoop [40], 18% by Popoff [44] and 39% by Yilmaz [17], to name a few. The convincing feature of these latter values is that they were the actual measured transmittance by projecting light through the medium.

The average transmittance obtained from the measured TM is $\langle \mathcal{T} \rangle = 0.071$. This is smaller than the predicted transmittance of $\langle \mathcal{T} \rangle = 0.166$ because we only measure a partial TM, so that the detected transmission scales as $(\text{NA})^2$. As explained in Section 3.3.3, we digitally filter the transmitted fields in Fourier

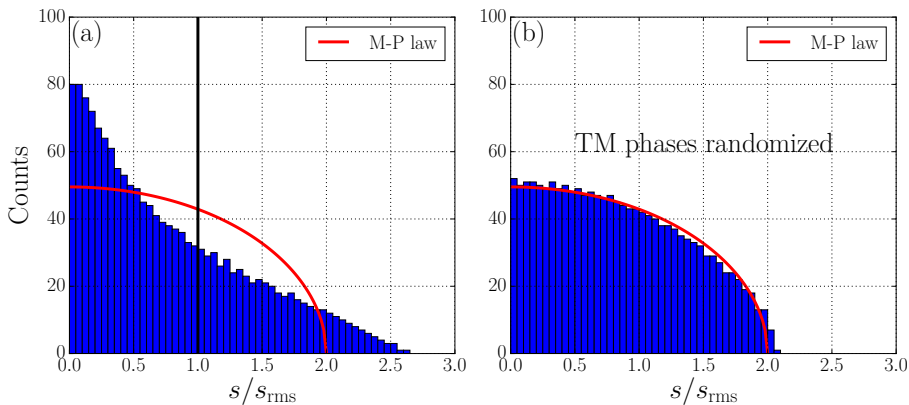


Figure 5.4: (a) Singular value distribution normalized to the RMS value and (b) for the phases of the TM elements randomized. The Marchenko-Pastur curve for an uncorrelated random Gaussian matrix is plotted in red. The vertical line indicates the normalized RMS singular value.

space to a slight overestimation of $\text{NA} = 1$. However, we use oil immersion with a refractive index of 1.5 on the detection side, so the effective filtering fraction reduces to $1/1.5^2 = 0.44$. Therefore, with our optical setup and digital filtering, we would expect to measure an average transmittance of $0.166/1.5^2 = 0.074$ which, within the uncertainties, agrees extremely well to the value of 0.071 found in our experiment.

As a measure of the accuracy of our TM, we look for mesoscopic correlations in the singular value distribution of the ZnO sample. In Fig. 5.4(a), we normalize the singular values with respect to their RMS value and simultaneously plot the Marchenko-Pastur (M-P) curve associated to an uncorrelated Gaussian random matrix. The clear deviation from the M-P law provides convincing evidence that we do indeed measure correlations in the TM. We note that most channels (68%) in our optically dense medium lie to the left of the RMS singular value, while only a few (32%) transmit more than the RMS value. In fact, we find channels with singular values 2.64 times greater than the RMS, corresponding to a transmittance enhancement of $2.64^2 \approx 7.0$. This shows that we successfully find a few highly transmitting channels that transport significantly more light through the sample than the majority of channels. To test whether the correlations stem from amplitude or phase correlations, we plot in Fig. 5.4(b) the singular value histogram after randomizing the phases of the TM elements. We observe that the distribution agrees well with the M-P law, indicating that the correlations lie within the phases of the TM elements and

that we are successfully able to detect them in our experiment.

5.2.1 Comparison with a filtered DMPK model

Since our measured singular value distribution shows signs of mesoscopic correlations, we compare it to a similar distribution predicted by transport theory. Given that we only measure a partial TM, our distribution should correspond to that predicted for a filtered DMPK matrix [34]. As found in Section 3.3, the effective NA of our system is 0.80. With the argument provided above, the filtering fraction further reduces by a factor of 1.5^2 to $0.80^2/1.5^2 = 0.28$ because of the refractive index $n = 1.5$ of the immersion oil. This is then the approximate fraction of the complete matrix that we record. Thus, we first numerically generate a large square matrix with DMPK statistics using a mean transmittance of $\langle \mathcal{T} \rangle = 0.166$, which is the predicted value by diffusion theory for a sample of thickness $10.1 \mu\text{m}$. We desire the filtered matrix to match the experimental matrix dimension of 1556×1556 , hence the size of the original DMPK matrix is 5535×5535 .

The singular value distribution of the resulting filtered TM is plotted in Fig. 5.5. We observe that apart from the extended tail beyond $s = 2.35$ of the experimental histogram, the measured and modeled distributions are in excellent agreement. In our simplistic model, we reduce the size of T_{DMPK} in a random way, which is not the case in the experiment where the reduced measured matrix is due to the absence of fields that fall outside the FOV and high- k fields that lie beyond the NA. According to a recent study by Yilmaz, open channels are more confined in space than closed ones [17], suggesting that we do measure a larger number of open channels than predicted by our model. This is a plausible explanation for the longer tail in the experimental singular value distribution. A better numerical model would be a full 3D simulation of wave propagation inside a scattering sample with the same physical parameters, but this is numerically expensive and currently an open problem.

In summary, we clearly observe mesoscopic correlations in the singular values of our partial TM of a $10 \mu\text{m}$ -thick ZnO layer even though we measure only an estimated fraction of 28% of the complete matrix. It is remarkable that we find open channels that exhibit close to 50% intensity transmission with respect to air given that they pass through a strongly scattering medium of about 15 mean free paths in thickness. We also conclude that the maximum absolute transmittance we report here is one of the highest compared to values found for similar optical thickness samples in literature.

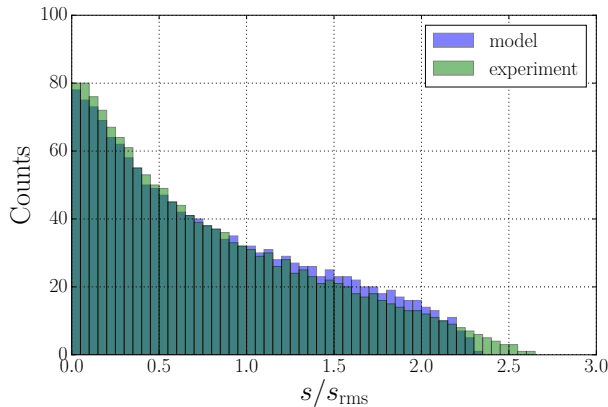


Figure 5.5: Comparison of the measured singular value distribution with a numerically modeled filtered DMPK distribution. The singular values s are normalized to the RMS value s_{rms} .

5.3 Properties of individual transmission channels

In this section we explore the properties of individual transmission channels. First, we present the spatial profiles of open, closed and average channels and compare them to the profile of a random incident wave. We look at their speckle statistics and investigate whether they show signs of mesoscopic fluctuations. Finally, we study what occurs to the spatial intensity statistics if we isolate and inject individual channels of the measured TM through the medium.

5.3.1 Spatial profile

We investigate the transmitted spatial profiles of the individual channels by simulating an experimental projection [5]. As the TM is measured in the Bessel mode basis, the transmission channels we calculate are column vectors whose elements indicate the contribution of the individual Bessel modes. The transmitted channel is digitally propagated through the scattering medium by multiplying the vector with the same TM¹. Subsequently, the spatial profiles of the channels are obtained by a superposition of the 2D Bessel modes with the appropriate coefficients of the transmitted channel.

Fig. 5.6 depicts the outgoing intensity profiles of the most open and closed channels, of a channel associated with the RMS singular value, and of a random incident wave. The total transmitted intensity is found by summing the

¹Ideally, to simulate a true experimental projection, one would like to use an independently measured TM so that the experimental noise is not canceled out. However such a TM was not measured for the data presented here.

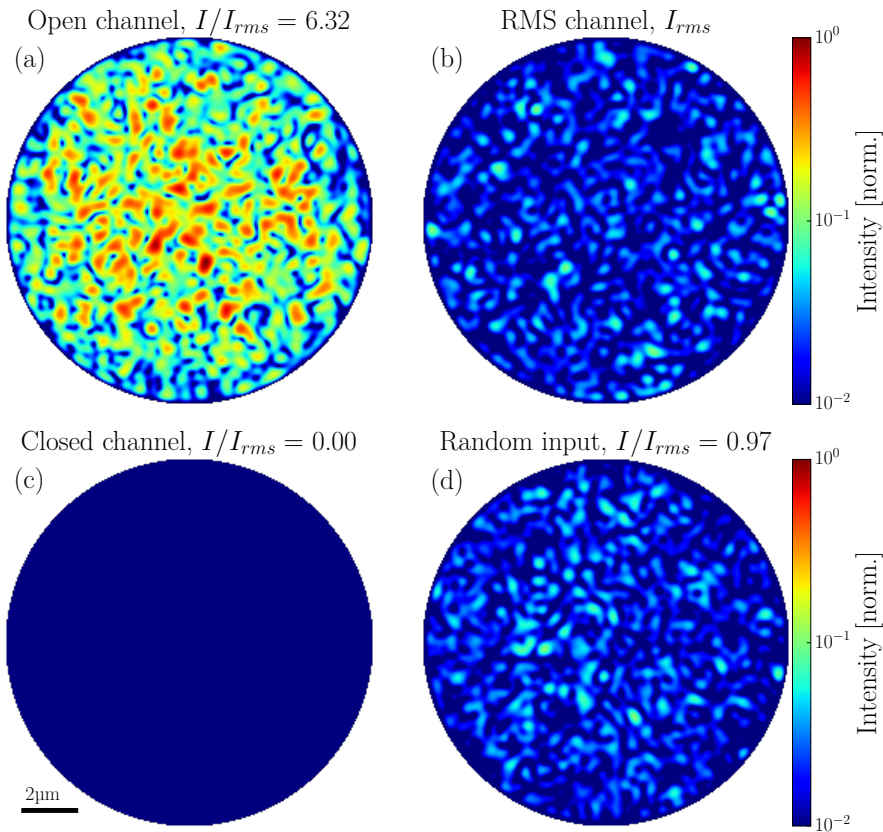


Figure 5.6: Spatial intensity profiles of (a) the most open transmission channel, (b) the RMS channel, (c) the most closed channel and (d) a random incident field transmitted through our ZnO sample. The intensity of all channels is normalized to the maximum of the open channel and is plotted on a logarithmic color scale. The total intensity ratio with respect to the RMS channel is mentioned at the top of each subplot.

values of all pixels. The open channel clearly stands out from the others as it transmits the most light and is 6.32 times brighter than the RMS channel. This is smaller than the value of 7 claimed from the singular value histogram in the previous section because here we use all available pixels whereas the histogram uses a sampled version of the 2D image, viz., a vector of Bessel modes. If the sampling were ideal, there would be no loss of information and the two values would coincide. However, we do not filter in Fourier space perfectly and hence do not fulfil the sampling theorem exactly. We therefore observe a lower value of

the transmitted intensity, which is a closer estimate of the value we would have observed in an actual experiment. Compared to the open channel, the closed channel does not transmit any light as is observed by the lack of noticeable bright spots in its spatial profile. A random incident field transmits approximately the same amount of intensity ($I/I_{\text{rms}} = 0.97$) as the RMS channel and looks similar to it.

The open channel is the only one among the plotted intensity profiles that seems to possess a spatial envelope that is different from the aperture. This observation could be linked to recently published work [17] which reports that open channels have a smaller inverse participation ratio (IPR) – which the authors interpret as a measure of the width of the envelope – than less transmissive channels. This could explain the apparent absence of an envelope in the spatial profiles of the other patterns in Fig. 5.6(b-d). Apart from the different brightness and envelope effect, there doesn't seem to be any other visibly special feature in the spatial profiles of the channels as they resemble speckle patterns.

5.3.2 Intensity statistics

To test whether the transmission channels are speckle-like, we compare their intensity statistics with that of a speckle. A characteristic property of a fully developed speckle is that the distribution of its intensities in any one of its polarization components obeys negative exponential statistics [45],

$$P(I) = \frac{1}{\bar{I}} \exp\left(-\frac{I}{\bar{I}}\right), \quad (5.2)$$

where $P(I)$ is the probability of intensity I and \bar{I} is the mean intensity in that polarization component. However, it has been shown that mesoscopic effects in a strongly scattering 3D medium modify the speckle intensity distribution to [1, 22–24]

$$P(I) = \frac{1}{\bar{I}} \exp\left(-\frac{I}{\bar{I}}\right) \left\{ 1 + \frac{1}{3g} \left[\left(-\frac{I}{\bar{I}}\right)^2 - 4\left(-\frac{I}{\bar{I}}\right) + 2 \right] \right\}, \quad (5.3)$$

where g is the dimensionless conductance, which is equal to the sum of the transmittances s^2 of the N transmission channels that an incident wave can couple to,

$$g = \sum_n^N s_n^2 = N \langle \mathcal{T} \rangle, \quad (5.4)$$

with $\langle \mathcal{T} \rangle$ the ensemble averaged intensity transmission through the medium. In an open 3D slab-type medium, g depends on the shape and size of the

incident wave [46–48]. It is clear to see from eq. (5.3) that when g is large, the probability density function reduces to the simple exponential decay function in eq. (5.2). We also note that the second term in the curly braces starts playing a prominent role for large intensities I . Moreover, the dimensionless conductance is approximately equal to the number N_{eff} of effectively “open” channels, i.e., $g \approx N_{\text{eff}}$ [25, 26]. Thus, media with a few open channels show more deviations from the negative exponential law than media with a large number of open channels.

We note that g counts the channels of the TO that the incident wave couples to. This may be different from the number of singular vectors of the TM if the TM undersamples the TO, which is the case in optical experiments [34]. The first experimental evidence for universal conductance fluctuations in the transmission of light was shown by Scheffold and Maret [27]. Observations of deviations from eq. (5.2) have previously been reported in waveguides [30, 31] and for anisotropic [28] and isotropic [29] 3D diffuse media. In both cases of the 3D disordered samples, the transmitted speckle intensity distribution was studied for a focused incident field. When the incident beam was focused on the sample surface, it could couple to only a few channels and hence g was small enough for statistics described by eq. (5.3) to appear. However, for an out-of-focus configuration where the available channels N is large, the mesoscopic effects were not detected. For the isotropic medium, similar to the one in our case, a value of $g = 35 \pm 4$ was measured for a sample of thickness 11 μm .

We conclude from the results in Refs. [28] and [29] that to observe a reduced value of g without changing the thickness of the sample, an incident wave must couple to fewer channels. This raises the question as to what the effective dimensionless conductance g of a single channel is. This can be studied by sending a single transmission channel itself as the incident field, using eq. (5.3) to find g from the intensity statistics. By definition, the channels are orthogonal and therefore the incident intensity will be transported through the medium in that single channel.

We investigate at first the probability density function of the intensity statistics of the most open channel, a channel with a transmittance equal to the RMS, and a random incident field. We don’t study the single most closed channel because the transmitted intensity is too low compared to the noise to conduct a meaningful analysis. To normalize to the average envelope function of the transmitted speckle patterns, we digitally send 200 different random fields through the measured TM and take the averaged intensity image in each separate polarization component. The spatial profiles of the channels are then divided pixel by pixel with the average intensity profile before studying the distribution of the intensities.

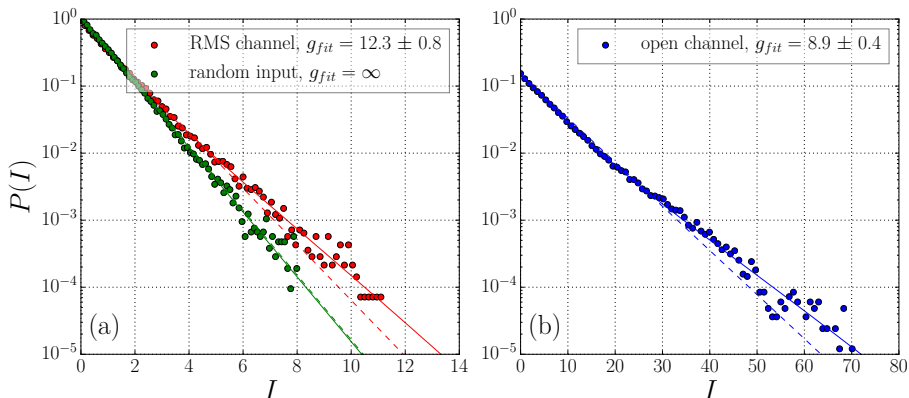


Figure 5.7: Normalized probability density function of the spatial intensity statistics of (a) the RMS channel and a random incident field, and (b) the most open transmission channel transmitted through the ZnO sample. The intensity probability is plotted on a logarithmic scale. The dashed lines are exponential curves given by eq. (5.2) and the solid lines are fits of eq. (5.3) with g as the free parameter.

The histograms in Fig. 5.7 are the sum of the distributions in the horizontal and vertical polarization components, thereby giving us better statistics. We plot eq. (5.2) representing negative exponential statistics (dashed lines) and fit the intensity distributions of these fields with eq. (5.3) (solid lines) with the dimensionless conductance g as the free parameter. We observe that the random input in Fig. 5.7(a) is nearly identical with the simple exponential decay as we cannot distinguish between the dashed and solid lines. In this case, the dimensionless conductance is effectively $g = \infty$. This is equivalent to the out-of-focus experiments performed by Strudley *et al.* [28,29] since the random field is composed of several channels and hence g is large. On the other hand, the RMS channel with nearly identical transmittance markedly deviates from normal speckle statistics for higher intensities, and the fit yields $g = 12.3 \pm 0.8$. This shows that the speckle of a channel of the TM has different statistics than that of a random incident field. We corroborate this by finding the same kind of deviation for the most open channel in Fig. 5.7(b), where the fit gives $g = 8.9 \pm 0.4$.

The g values of average transmission channels and open channels are comparable to each other ($g \approx 10$) even though the transmittances differ by a factor greater than 6. We conjecture therefore that one channel of the experimental TM is composed of a small number of channels, likely around 10, of the TO. Moreover, the fit function is an approximation that is valid for $g \gg 1$. We

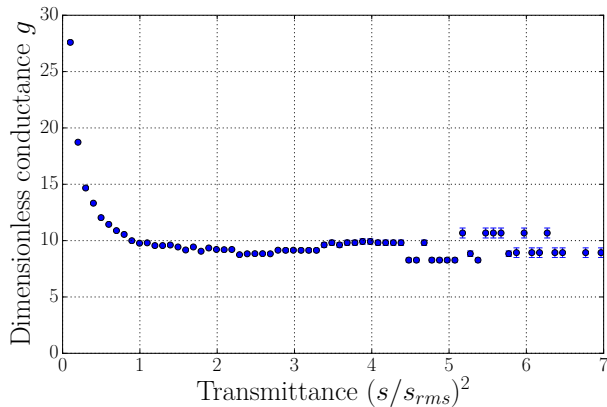


Figure 5.8: Dimensionless conductance g as a function of the normalized channel transmittance $(s/s_{rms})^2$. The channels with similar transmittance are binned together.

note that the values we find are much smaller than $g = 35$ reported for a similar isotropic ZnO sample in Ref. [29], indicating that we successfully couple to fewer open channels of the TO.

We extend the same analysis to all transmission channels, but as individual ones could have wildly fluctuating statistics that could affect the fits, we bin channels with similar transmittances and perform the fit for their combined intensity distributions. The results are displayed in Fig. 5.8 and we notice that all channels with a normalized transmittance greater than 1 have an approximately constant dimensionless conductance $g \approx 9$. Apparently every channel of our partial TM is composed of approximately 9 open channels of the TO. Below a normalized transmittance of 1, the value of g shoots up and we believe there are two main factors which contribute to this. First, part of the rise seems physical since the density of channels at low transmittances is high, as shown in Fig. 5.4(a), making it easier for the single experimental channel to couple to many channels of the TO with similar transmittance. Second, the signal-to-noise ratio falls and the noisy channels are redistributed among a larger number of TO channels.

Next, we investigate the effect of having multiple channels at the input. To this end, we create an incident field as an equal superposition of N different channels of the TM, each with an arbitrary global phase. We find the average intensity distribution for 50 different realizations of the superposition of N different channels, and then retrieve the conductance g by performing a fit. We

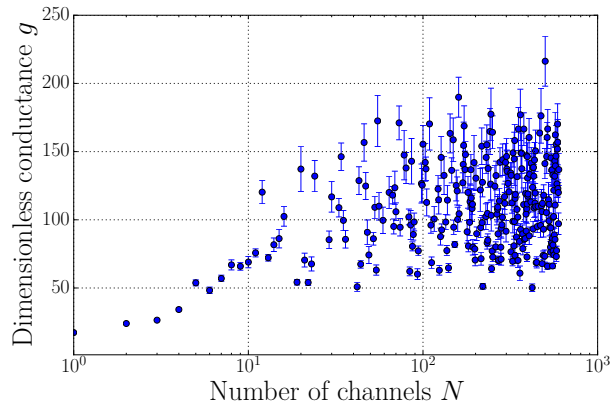


Figure 5.9: Dimensionless conductance g as a function of the number of channels N contained in the input field. Each channel has an equal weight in the superposition but with an arbitrary global phase. Every data point is the result of 50 random realizations of the combination of the corresponding number of channels N . The error bars result from the fit to eq. (5.3).

perform this for N going from 1 to 600 and plot the results in Fig. 5.9². We notice that for $N < 100$, g grows with increasing N and then saturates. The initial growth is the expected behavior as g , which is effectively the number of open channels an incident field couples to, increases with greater N . However, the number of open channels in the sample given by eq. (5.4) is estimated to lie between 100 and 150. Therefore, once N reaches about 100, the dimensionless conductance g saturates around that value. It should be noted that for the fit, it is hard to distinguish between $g \approx 100$ and $g = \infty$. Hence, there is a wider spread and larger fitting errors for $N > 100$. Nonetheless, we conclude that g increases when the initial field is composed of more transmission channels until it saturates at the effective number of open channels in the sample. Additionally, we infer that the measured value of g could be associated to a superposition of channels of the TO.

5.4 Conclusion

In this chapter, we investigated the TM of isotropic strongly scattering media of ZnO nanoparticles and found effects of strong mesoscopic correlations in their singular value spectrum. The “open” transmission channels for a 10 μm -thick

²The data points with an error estimate resulting from the fit greater than 20 are not shown on the plots.

sample were more than 6 times more transmissive than an average channel. The spatial profiles of the transmitted speckles showed signs of deviation from a negative exponential function in contrast to the transmission of random inputs or the superposition of a large number of channels. This indicates that probing the speckle intensity distribution of individual channels may be an effective way to explore mesoscopic correlations in complex media.

Bibliography

- [1] M. C. W. van Rossum and T. M. Nieuwenhuizen, “Multiple scattering of classical waves: microscopy, mesoscopy, and diffusion,” *Rev. Mod. Phys.* **71**, 313–371 (1999).
- [2] I. M. Vellekoop and A. P. Mosk, “Universal optimal transmission of light through disordered materials,” *Phys. Rev. Lett.* **101**, 120601 (2008).
- [3] Z. Shi and A. Z. Genack, “Transmission eigenvalues and the bare conductance in the crossover to Anderson localization,” *Phys. Rev. Lett.* **108**, 043901 (2012).
- [4] M. Davy, Z. Shi, J. Wang, and A. Z. Genack, “Transmission statistics and focusing in single disordered samples,” *Opt. Express* **21**, 10367–10375 (2013).
- [5] B. Gérardin, J. Laurent, A. Derode, C. Prada, and A. Aubry, “Full transmission and reflection of waves propagating through a maze of disorder,” *Phys. Rev. Lett.* **113**, 173901 (2014).
- [6] X. Hao, L. Martin-Rouault, and M. Cui, “A self-adaptive method for creating high efficiency communication channels through random scattering media,” *Sci. Rep.* **4** (2014).
- [7] S. F. Liew, S. M. Popoff, A. P. Mosk, W. L. Vos, and H. Cao, “Transmission channels for light in absorbing random media: From diffusive to ballistic-like transport,” *Phys. Rev. B* **89**, 224202 (2014).
- [8] M. Kim, W. Choi, C. Yoon, G. H. Kim, S. hyun Kim, G.-R. Yi, Q.-H. Park, and W. Choi, “Exploring anti-reflection modes in disordered media,” *Optics Express* **23**, 12740 (2015).
- [9] M. Davy, Z. Shi, J. Park, C. Tian, and A. Z. Genack, “Universal structure of transmission eigenchannels inside opaque media,” *Nature Communications* **6** (2015).
- [10] A. Daniel, L. Liberman, and Y. Silberberg, “Wavefront shaping for glare reduction,” *Optica* **3**, 1104–1106 (2016).
- [11] D. Akbulut, T. Strudley, J. Bertolotti, E. P. A. M. Bakkers, A. Lagendijk, O. L. Muskens, W. L. Vos, and A. P. Mosk, “Optical transmission matrix as a probe of the photonic strength,” *Phys. Rev. A* **94**, 043817 (2016).
- [12] C. W. Hsu, S. F. Liew, A. Goetschy, H. Cao, and A. D. Stone, “Correlation-enhanced control of wave focusing in disordered media,” *Nature Physics* **13**, 497–502 (2017).
- [13] P. Hong, O. S. Ojambati, A. Lagendijk, A. P. Mosk, and W. L. Vos, “Three-dimensional spatially resolved optical energy density enhanced by wavefront shaping,” *Optica* **5**, 844–849 (2018).
- [14] S. Rotter and S. Gigan, “Light fields in complex media: Mesoscopic scattering meets wave control,” *Rev. Mod. Phys.* **89**, 015005 (2017).

- [15] P. Fang, C. Tian, L. Zhao, Y. P. Bliokh, V. Freilikher, and F. Nori, “Universality of eigenchannel structures in dimensional crossover,” *Phys. Rev. B* **99**, 094202 (2019).
- [16] H. Yilmaz, C. W. Hsu, A. Goetschy, S. Bittner, S. Rotter, A. Yamilov, and H. Cao, “Angular memory effect of transmission eigenchannels,” *Phys. Rev. Lett.* **123**, 203901 (2019).
- [17] H. Yilmaz, C. W. Hsu, A. Yamilov, and H. Cao, “Transverse localization of transmission eigenchannels,” *Nature Photonics* **13**, 352–358 (2019).
- [18] D. A. B. Miller, “Waves, modes, communications, and optics: a tutorial,” *Adv. Opt. Photon.* **11**, 679–825 (2019).
- [19] E. N. Economou and C. M. Soukoulis, “Static conductance and scaling theory of localization in one dimension,” *Phys. Rev. Lett.* **46**, 618–621 (1981).
- [20] D. S. Fisher and P. A. Lee, “Relation between conductivity and transmission matrix,” *Phys. Rev. B* **23**, 6851–6854 (1981).
- [21] J. Pendry, A. MacKinnon, and A. Pretre, “Maximal fluctuations — a new phenomenon in disordered systems,” *Physica A: Statistical Mechanics and its Applications* **168**, 400–407 (1990).
- [22] N. Shnerb and M. Kaveh, “Non-Rayleigh statistics of waves in random systems,” *Phys. Rev. B* **43**, 1279–1282 (1991).
- [23] T. M. Nieuwenhuizen and M. C. W. van Rossum, “Intensity distributions of waves transmitted through a multiple scattering medium,” *Phys. Rev. Lett.* **74**, 2674–2677 (1995).
- [24] E. Kogan, M. Kaveh, R. Baumgartner, and R. Berkovits, “Statistics of waves propagating in a random medium,” *Phys. Rev. B* **48**, 9404–9410 (1993).
- [25] O. Dorokhov, “On the coexistence of localized and extended electronic states in the metallic phase,” *Solid State Communications* **51**, 381 – 384 (1984).
- [26] Y. Imry, “Active transmission channels and universal conductance fluctuations,” *Europhysics Letters (EPL)* **1**, 249–256 (1986).
- [27] F. Scheffold and G. Maret, “Universal conductance fluctuations of light,” *Phys. Rev. Lett.* **81**, 5800–5803 (1998).
- [28] T. Strudley, T. Zehender, C. Blejean, E. P. A. M. Bakkers, and O. L. Muskens, “Mesoscopic light transport by very strong collective multiple scattering in nanowire mats,” *Nature Photonics* **7**, 413 (2013).
- [29] T. Strudley, D. Akbulut, W. L. Vos, A. Lagendijk, A. P. Mosk, and O. L. Muskens, “Observation of intensity statistics of light transmitted through 3D random media,” *Opt. Lett.* **39**, 6347–6350 (2014).
- [30] M. Stoytchev and A. Z. Genack, “Observations of non-Rayleigh statistics

- in the approach to photon localization,” *Opt. Lett.* **24**, 262–264 (1999).
- [31] A. Peña, A. Girschik, F. Libisch, S. Rotter, and A. A. Chabanov, “The single-channel regime of transport through random media,” *Nature Communications* **5**, 3488 (2014).
- [32] P. W. Anderson, “Absence of diffusion in certain random lattices,” *Phys. Rev.* **109**, 1492–1505 (1958).
- [33] A. Lagendijk, B. Van Tiggelen, and D. S. Wiersma, “Fifty years of anderson localization,” *Phys. Today* **62**, 24–29 (2009).
- [34] A. Goetschy and A. D. Stone, “Filtering random matrices: The effect of incomplete channel control in multiple scattering,” *Phys. Rev. Lett.* **111**, 063901 (2013).
- [35] H. Yu, T. R. Hillman, W. Choi, J. O. Lee, M. S. Feld, R. R. Dasari, and Y. Park, “Measuring large optical transmission matrices of disordered media,” *Phys. Rev. Lett.* **111**, 153902 (2013).
- [36] P. Mello, P. Pereyra, and N. Kumar, “Macroscopic approach to multichannel disordered conductors,” *Annals of Physics* **181**, 290 – 317 (1988).
- [37] T. Martin and R. Landauer, “Wave-packet approach to noise in multichannel mesoscopic systems,” *Phys. Rev. B* **45**, 1742–1755 (1992).
- [38] I. Vellekoop, “Controlling the propagation of light in disordered scattering media,” Ph.D. thesis, University of Twente (2008).
- [39] H. Yang and P. Jiang, “Large-scale colloidal self-assembly by doctor blade coating,” *Langmuir* **26**, 13173–13182 (2010). PMID: 20695556.
- [40] I. M. Vellekoop, E. G. van Putten, A. Lagendijk, and A. P. Mosk, “Demixing light paths inside disordered metamaterials,” *Opt. Express* **16**, 67–80 (2008).
- [41] E. G. van Putten, “Disorder-enhanced imaging with spatially controlled light,” Ph.D thesis, University of Twente (2011).
- [42] D. Akbulut, “Measurements of strong correlations in the transport of light through strongly scattering materials,” Ph.D thesis, University of Twente (2013).
- [43] S. Tripathi, R. Paxman, T. Bifano, and K. C. Toussaint, “Vector transmission matrix for the polarization behavior of light propagation in highly scattering media,” *Opt. Express* **20**, 16067–16076 (2012).
- [44] S. M. Popoff, A. Goetschy, S. F. Liew, A. D. Stone, and H. Cao, “Coherent control of total transmission of light through disordered media,” *Phys. Rev. Lett.* **112**, 133903 (2014).
- [45] J. Goodman, *Statistical Optics*, A Wiley-Interscience publication (Wiley, 1985).
- [46] R. Pnini and B. Shapiro, “Fluctuations in transmission of waves through disordered slabs,” *Phys. Rev. B* **39**, 6986–6994 (1989).

- [47] F. Scheffold, W. Härtl, G. Maret, and E. Matijević, “Observation of long-range correlations in temporal intensity fluctuations of light,” *Phys. Rev. B* **56**, 10942–10952 (1997).
- [48] J. F. de Boer, M. P. van Albada, and A. Lagendijk, “Transmission and intensity correlations in wave propagation through random media,” *Phys. Rev. B* **45**, 658–666 (1992).

6 Scattering invariant modes¹

Light transmitted through a multiple scattering material is strongly distorted. Nonetheless, the advent of optical wavefront shaping techniques developed since the first demonstration of focusing light through such media [1] has made it possible to control the transmission of scattered light [2,3]. Furthermore, it has been shown by Popoff *et al.* that measured transmission matrices can be used to faithfully recover images propagated through diffuse media [4]. However, so far, successful imaging techniques rely mostly on ballistic light even though it is strongly attenuated for thick media. We therefore ask ourselves whether the TM can be used to find fields that behave like ballistic light and transmit as if the material were transparent. Nevertheless, since the TM only deals with external waves, it does not provide any knowledge of what happens to these waves inside the medium.

In this chapter, we show a way of finding such scattering invariant modes (SIMs) that seem to avoid the scatterers in a strong scattering medium. These fields are transmitted with the same spatial profile through a scattering medium as through air. Hence, apart from a possible global amplitude and phase scaling, the material is effectively invisible for these remarkable SIMs.

We find these waves experimentally by first measuring the transmission matrices of air and a scattering medium, after which we use them to numerically solve an eigenvalue equation. We then project these fields through air and the scattering sample using digital holography and show that their spatial profiles exhibit high similarity². Finally, we investigate the physical properties of the SIMs and study whether they indeed avoid scatterers in a sparse scattering sample.

6.1 Definition

When a SIM \tilde{E}_{in} is projected through air, it diffracts and emerges as the transmitted field $\tilde{E}_{\text{out}} = T_{\text{air}}\tilde{E}_{\text{in}}$, where T_{air} is the transmission matrix of air. When it is incident on a scattering medium instead, the transmitted field is $\alpha\tilde{E}_{\text{out}}$,

¹The results in this chapter will be presented in a forthcoming publication: P. Pai, J. Bosch, M. Kühmayer, S. Rotter and A. P. Mosk (in preparation)

²The work presented in Sections 6.2 and 6.3 is performed in collaboration with my colleague Jeroen Bosch using the apparatus constructed by him. Email: j.bosch@uu.nl

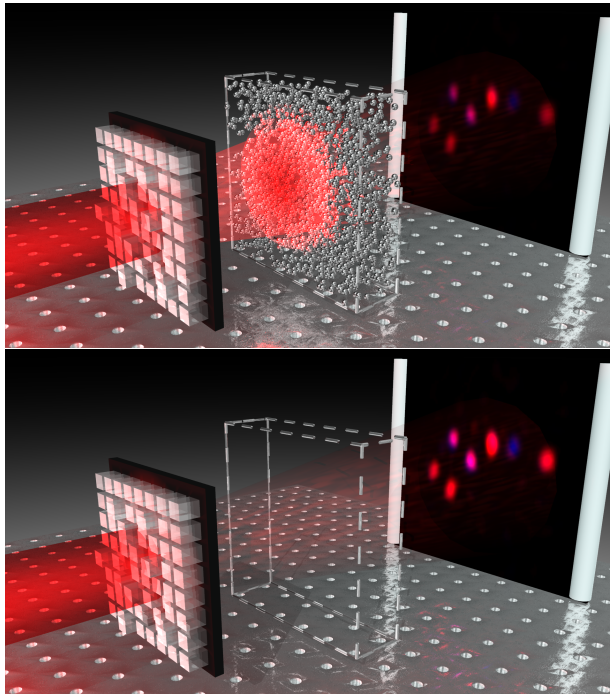


Figure 6.1: Cartoon of a SIM \tilde{E}_{in} propagating through a scattering layer (top) and an air layer (bottom). The spatial profile of the outgoing field \tilde{E}_{out} is the same through both materials. The only difference is that there is a global scale factor α between them. [5]

where α is a complex constant which we designate as the eigenvalue corresponding to the SIM. The reason for the eigenvalue α is that as the wave propagates through the scattering sample, some of the light is reflected and the amplitude of the transmitted light is smaller than in the case of air. A global phase is also contained within α . Although there is a global amplitude and phase difference, by definition the shape of the spatial profile of both transmitted fields is exactly the same, as depicted in Fig. 6.1. It is important to note that SIMs are specific to the individual realization of the scattering sample and therefore not translation invariant. However, this restriction does not apply in air since it is a translation invariant medium.

Theoretically, one finds these special waves by using the transmission matrix T of both media. The two transmitted fields have the same spatial profile, so we can equate them and write

$$T_s \tilde{E}_n = \alpha_n T_{\text{air}} \tilde{E}_n, \quad (6.1)$$

where T_s and T_{air} are the transmission matrices of the scattering layer and of air respectively, and α_n is a global complex constant. This is a generalized eigenvalue equation, and therefore its solutions \tilde{E}_n are called generalized eigenvectors with generalized eigenvalues α_n .

The generalized eigenvalue equation (6.1) above can be solved exactly, but for that either T_s or T_{air} has to be inverted. Unfortunately, T_s is a singular matrix that does not possess an exact inverse. The air matrix T_{air} is unitary in theory, but in an experiment it becomes ill-conditioned and contains a few near-zero singular values due to diffraction and imperfections in the TM measurement. These singular values then cause unwanted numerical instabilities when inverting the matrix [6, 7]. However, for small thicknesses of air as is the case in our configuration, most singular values are close to 1 but a few are very small (see Chapter 4). Thus we can multiply by T_{air}^\dagger on both sides of eq. (6.1) to obtain a stable approximation of the generalized eigenvalue equation

$$T_{\text{air}}^\dagger T_s \tilde{E}_n = \alpha_n \tilde{E}_n. \quad (6.2)$$

The problem then is reduced to a standard eigenvalue equation, where the SIMs \tilde{E}_n are the eigenvectors of the matrix $T_{\text{gen}} = T_{\text{air}}^\dagger T_s$ and the α_n are its eigenvalues. This matrix is not normal, i.e., it does not commute with its Hermitian conjugate, and as a result the SIMs do not in general form an orthogonal basis.

6.2 Experimental determination of SIMs

To find the SIMs of a scattering sample with respect to air, one has to know the TMs of the two media. In this section, we experimentally measure the TMs of a sample of zinc oxide (ZnO) nanoparticles and the same thickness of air and consequently determine the SIMs. The measurements in this section and the next are performed on an apparatus that can measure TMs and project SIMs using digital micromirror device (DMD) based amplitude and phase modulation [8]. The measurement method is the same as the one detailed in Chapter 3.

The scattering invariant modes and corresponding eigenvalues are calculated from measured TMs of air and the scattering medium. Using a frequency tunable laser (New Focus Velocity TLB-6712) at a wavelength of $\lambda = 771$ nm, the transmission matrix is measured in a basis of k -vectors, where we sample the input k -vectors (instead of focused spots) on a hexagonal grid to maximize the sampling density. A holographic projection system, consisting of a digital micromirror device (DMD, Vialux V-9600), is used to project plane waves for measuring the transmission matrix. Our holographic projection performs phase and amplitude modulation with Lee holography [9] and simultaneously controls

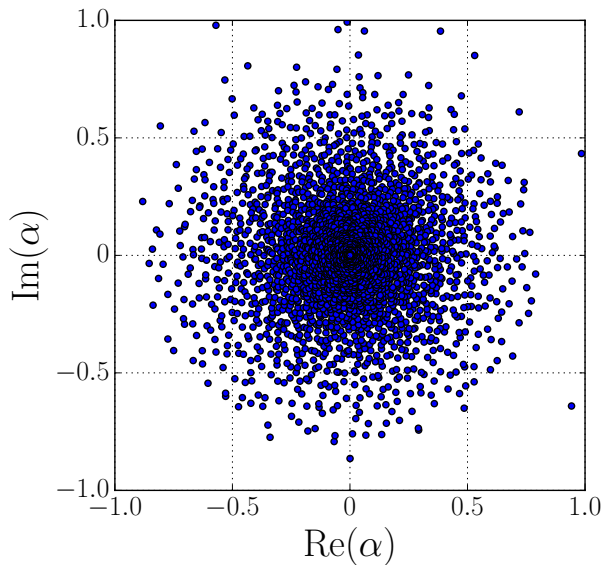


Figure 6.2: Complex eigenvalue spectrum of a layer of ZnO and air. The horizontal and vertical axes represent the real and imaginary parts of the eigenvalues. [5]

both the horizontal and the vertical polarization component of the light. We use high NA microscope objectives (0.95-NA, Zeiss N-Achroplan and 1.4-NA Zeiss Plan-Apochromat oil immersion objective) to allow a high degree of control of the light.

Our sample is a ZnO layer sprayed on a cover slide. The sample is prepared as detailed in Section 5.1.1. The thickness of the sample is $2.1 \pm 0.5 \mu\text{m}$, corresponding to about 3 transport mean free paths, and the average transmittance of the sample is close to 30% with respect to the same thickness of air. Part of the cover slide is clean, permitting measurement of the air matrix. Translation of the sample between the scattering material and the air medium is achieved with a high-accuracy stage (SmarAct SLC-1740-S and SLC-1720-S, 25 nm specified reproducibility). The objectives are mounted on piezo stages (Piezosystem Jena PX100 SG-D) that allow us to focus on the sample and vary the thickness of the air layer. Additionally, it enables us to measure the thickness of the sample *in situ* by first focusing both objectives on the surface of the cover glass, and then on the two surfaces of the scattering medium. The air TM is measured for an air thickness equal to that of the ZnO layer. The duration of the entire TM measurement is approximately 40 minutes and the resulting polarization-resolved TMs have a dimension of 2282×2282 .

Once the TMs of the ZnO sample and the air are measured, the SIMs and associated eigenvalues are calculated by solving the eigenvalue problem eq. (6.2). The complex eigenvalue spectrum is shown in Fig. 6.2, and it possesses three distinct features. First, the phase is isotropic, which means that there is no preferential phase for the SIMs, which conforms to our expectation for a strongly scattering medium. Second, the spectrum is not sharply bounded as there exist a few outliers. Finally, the amplitude of the eigenvalue distribution ranges from 0, when there is no transmitted amplitude through ZnO, until around $|\alpha| = 0.85$. That corresponds to a transmitted intensity of close to 70% with respect to air. This is significantly higher than the average transmittance $\langle \mathcal{T} \rangle = 0.3$ of a random incident wave. More measurements and analysis of the distribution are presented in Section 6.4.

6.3 SIM projection

Each of the eigenvalues plotted in Fig. 6.2 has an associated SIM. We synthesize and project the SIMs through both media using the same holographic method, and subsequently measure the transmitted fields to verify that their spatial profiles are the same.

The projected field of a SIM corresponding to a high eigenvalue is plotted in Fig. 6.3. The complex fields are normalized to their maximum amplitude through the respective medium and depicted using an HSV (hue, saturation, value) color scheme, where the color represents the phase and the brightness corresponds to the field intensity. Even though the spatial profile of the SIM looks like a random speckle, the bright spots of the fields transmitted through air and the scattering medium can be seen to resemble each other. In fact, the cosine similarity of the sampled fields, defined as

$$C = \frac{E_{\text{air}} \cdot E_{\text{ZnO}}}{\sqrt{E_{\text{air}} \cdot E_{\text{air}}} \sqrt{E_{\text{ZnO}} \cdot E_{\text{ZnO}}}} = \frac{\sum_i E_{\text{air},i}^* E_{\text{ZnO},i}}{\sqrt{E_{\text{air}} \cdot E_{\text{air}}} \sqrt{E_{\text{ZnO}} \cdot E_{\text{ZnO}}}}, \quad (6.3)$$

is 0.68.

In Fig. 6.4, we show the measured cosine similarity (in blue) for all the SIMs as a function of the modulus of the complex eigenvalue. We find a maximum cosine similarity of 0.72, and notice that 775 out of 2282 eigenvectors ($\approx 34\%$) have a similarity greater than 0.5. We also plot the predicted similarity (in red) of the transmitted fields by multiplying the incident SIMs E_{in} with the measured TMs,

$$C_{\text{TM}} = \frac{(T_{\text{air}} E_{\text{in}}) \cdot (T_{\text{ZnO}} E_{\text{in}})}{|T_{\text{air}} E_{\text{in}}| |T_{\text{ZnO}} E_{\text{in}}|}, \quad (6.4)$$

where $|\dots|$ denotes the norm of the vector. We note that a perfect similarity

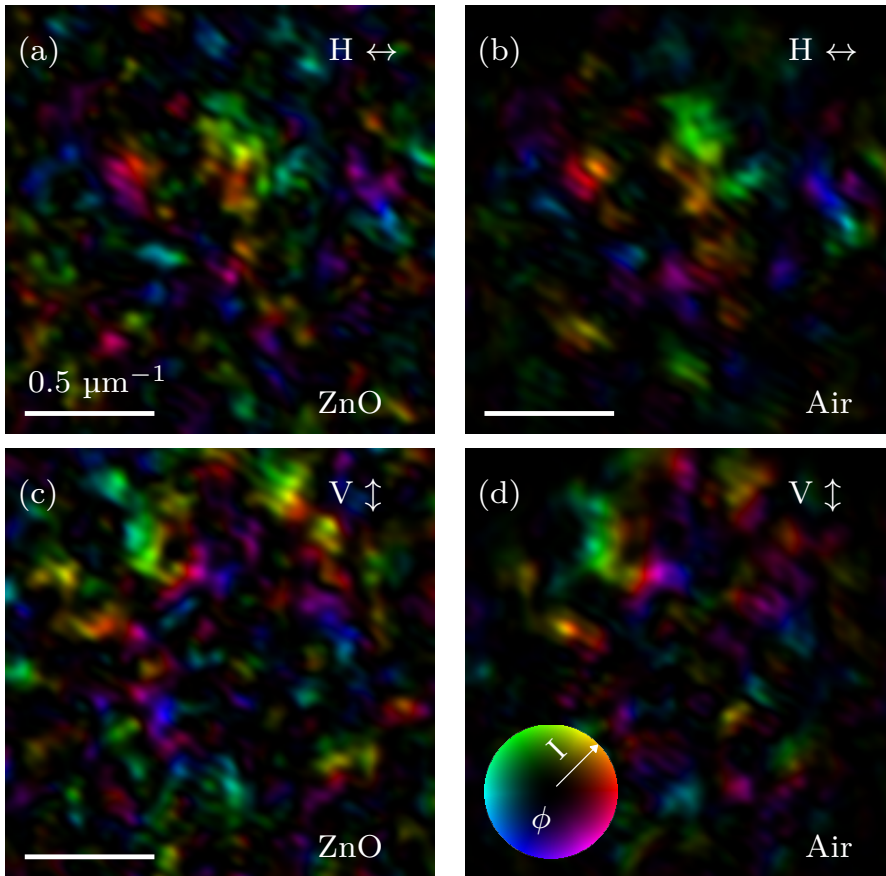


Figure 6.3: Field of a projected SIM through a layer of (a,c) ZnO and (b,d) the same thickness of air in the horizontal and vertical polarization components respectively. The cosine similarity of the fields is 0.68. The color represents phase and the brightness represents amplitude, as specified by the HSV (hue, saturation, value) color scheme shown in the inset in (d). [5]

of 1 is only expected for the exact generalized eigenvectors (eq. 6.1), while here we calculate them using the modified generalized eigenvalue equation (6.2). We observe that except for the very low $|\alpha|$, the predicted cosine similarity is very high (> 0.8). It is higher than the experimentally projected ones because the holographic projection is not perfect, induces some additional noise of its own, and is performed around four hours after the TM measurements which may incur small drifts.

It is interesting to notice in Fig. 6.4 that the cosine similarity is not uniform

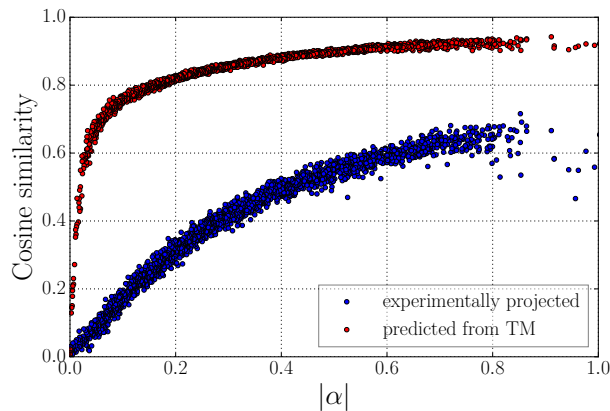


Figure 6.4: Cosine similarity of the scattering invariant modes propagated through air with the scattering invariant modes propagated through the scattering medium as a function of the eigenvalue modulus $|\alpha|$. The blue dots represent the experimental similarity and the red dots show the similarity predicted by the measured TMs. [5]

for all SIMs. For low magnitude eigenvalues we measure low cosine similarity, and for higher eigenvalues the cosine similarity increases to values as high as 0.72. The reason for this is that experimental noise has less effect on highly transmitting SIMs.

6.4 Eigenvalue statistics

So far, we have seen that SIMs exist and that we can successfully find them experimentally. However, we have only studied them as a mathematical construct derived from the transmission matrices. The fact that we can project them through air and a scattering layer with striking resemblance is merely an indication of the quality and precision of the optical setup, and doesn't disclose anything about the physical properties of the SIMs themselves. In this section, therefore, we would like to understand the distribution of the complex SIM eigenvalue spectrum which we showed in Fig. 6.2 and investigate whether it has traces of the DMPK statistics of light transport predicted by random matrix theory [3, 10–12]. To avoid the sampling effects originating from a spot basis, we study SIMs obtained from TMs measured in a Bessel mode basis as described in Chapter 4. We also use the experimental apparatus presented in Section 3.3.1 because it is optimized to measure TMs accurately. This apparatus cannot project the states physically, which is not a limitation when studying

statistics.

Since the SIM eigenvalue spectrum is obtained with TMs of both the ZnO and the air, we want to know the influence of the standard eigenvalue spectra of the individual TMs. In Chapter 4, we already discussed the eigenvalues of the TM of a slab of air. Hence, we start here by studying the eigenvalues λ of the ZnO TM satisfying the equation

$$T_{\text{ZnO}}E_{\text{in}} = \lambda E_{\text{in}}. \quad (6.5)$$

We use here the notation λ to differentiate from SIM eigenvalues α . The eigenvalue spectrum of a 1556×1556 TM of a scattering ZnO sample with a thickness of $5.1 \pm 0.1 \mu\text{m}$ is plotted in Fig. 6.5(a). We select a thicker sample than in Section 6.2 so that light transport lies more deeply in the diffusive regime. We observe that the distribution is not uniform as there is a higher concentration of low eigenvalues. This is in contrast to the spectrum of a random uncorrelated Gaussian matrix, which is a sharply bounded uniform distribution known as a Ginibre ensemble or a Ginibre disk [13]. This corroborates the finding in Chapter 5 that the elements of a TM of a scattering medium are correlated. We also showed that the correlations lie in the phases of the TM elements and that the singular value spectrum resembles the uncorrelated case when we scramble the phases. We perform the same test here for the eigenvalues λ_i and display the result in Fig. 6.5(b), where we do indeed observe a uniform Ginibre-like distribution.

Next, we look at the corresponding SIM eigenvalues α_i calculated by using the TM of a $5 \mu\text{m}$ -thick air layer, shown in Fig. 6.5(c). There is no discernible spiral that we observed for the air TM in Chapter 4 and there is no preferential angle in the distribution. In contrast, the high density around the origin, present in the eigenvalue spectra of both individual TMs, is clearly visible. Randomizing the phases of the ZnO TM and recalculating the eigenvalues results in the distribution in Fig. 6.5(d). The main difference that can be observed directly from these spectra is that when the phases are randomized, the eigenvalue disk shrinks. This is elucidated in the figure by plotting circles centered at the origin with a radius equal to the maximum SIM modulus of the true spectrum. We notice that no eigenvalue in Fig. 6.5(d) lies close to the circle. The size of the disk is therefore influenced by the mesoscopic correlations in the ZnO TM. Moreover, the density away from the origin looks more uniform, reminiscent of the properties of a Ginibre ensemble.

To gain more insight into the difference of the spectra in Fig. 6.5, we plot the corresponding histograms of the the eigenvalue amplitudes in Fig. 6.6. The red lines in the figure indicate the predicted distribution of a Ginibre ensemble with a disk size equal to the ZnO TM with random phases. We observe more clearly

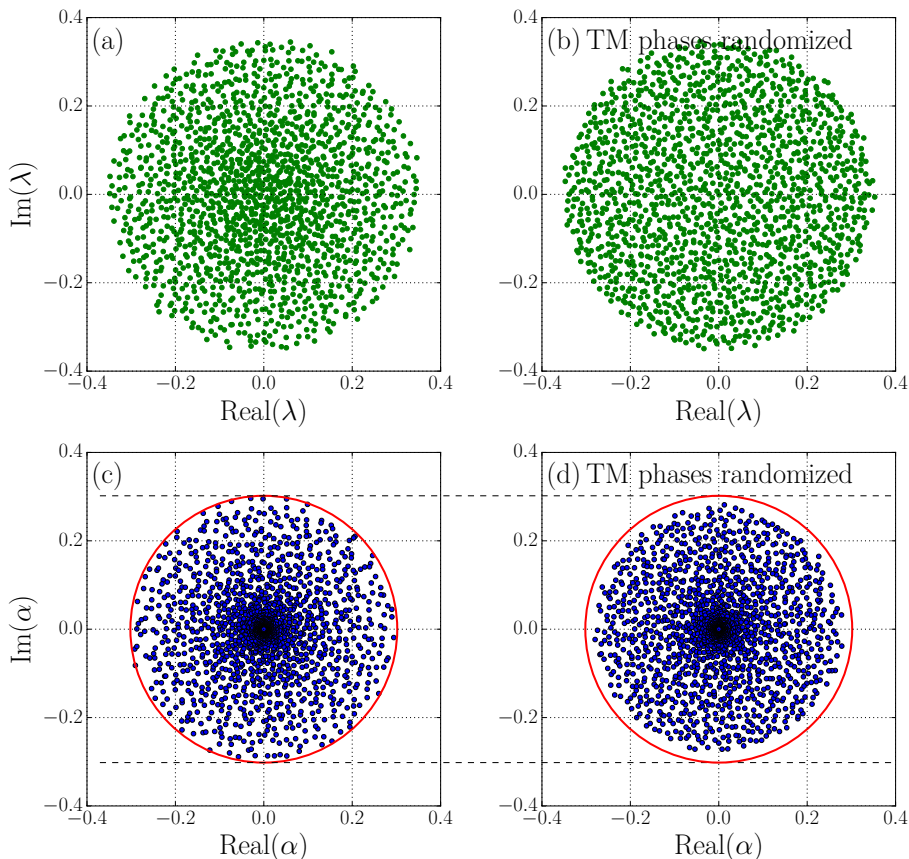


Figure 6.5: (a) Standard eigenvalue spectrum for a ZnO slab of thickness $5.1 \mu\text{m}$, and (b) the same spectrum when the phases of the ZnO TM are randomized. (c,d) SIM eigenvalue spectrum for the ZnO sample and an air reference with the same thickness before and after randomizing the ZnO TM phases. The circles have a radius equal to the maximum magnitude of the SIM eigenvalues of the non-randomized spectrum.

in the histogram of the standard eigenvalue moduli $|\lambda|$ of the ZnO TM that the inherent spectrum deviates from a Ginibre disk (Fig. 6.6(a)). After randomization of the TM phases, it coincides with the Ginibre result (Fig. 6.6(b)). Using our observation from Chapter 5 that a diffuse ZnO TM contains some of the DMPK signature, we deduce that in comparison to a Ginibre disk, the mesoscopic fluctuations give rise to a larger number of low eigenvalues λ_i and a smaller number of high ones.

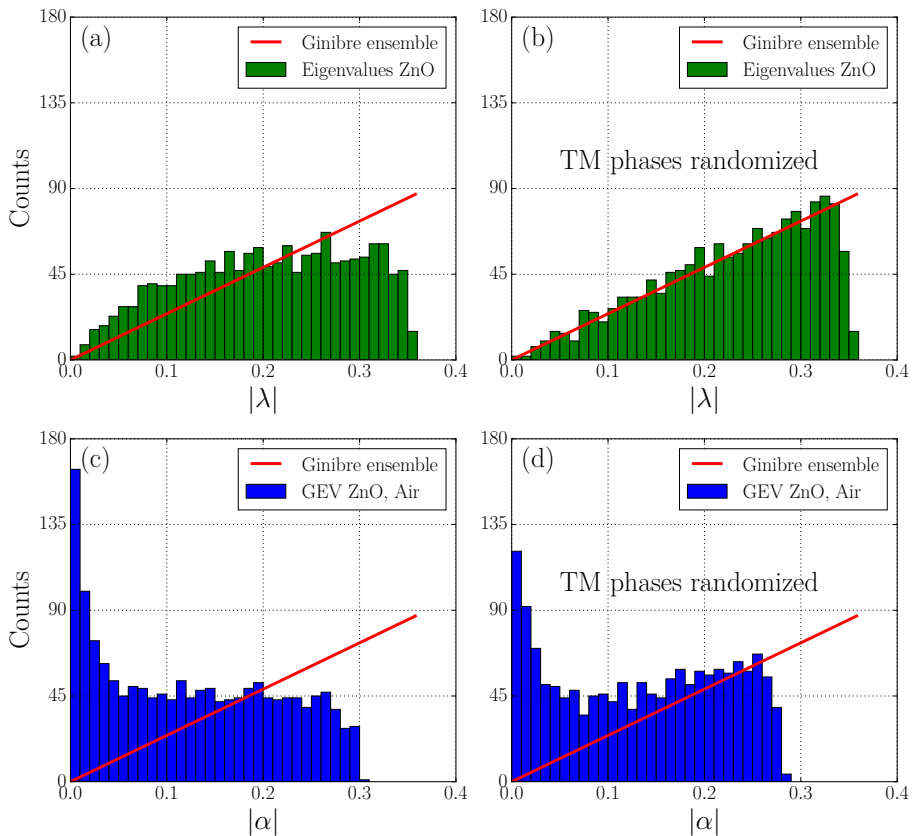


Figure 6.6: (a-d) Histograms of the eigenvalue moduli corresponding to the spectra (a-d) plotted in Fig. 6.5. The red lines indicate the theoretical distribution for a Ginibre ensemble associated to the ZnO TM with randomized phases.

The histograms of the SIM eigenvalue amplitudes $\{|\alpha_i|\}$ for the actual distribution and for random phases are shown in Fig. 6.6(c,d). Both seem to have some characteristics of the corresponding distributions of $\{\lambda_i\}$, with the non-randomized distributions exhibiting a higher number of low eigenvalues and the randomized ones approaching the Ginibre distribution better. Since the deviation of the statistics in Fig. 6.6(d) from the Ginibre disk is solely due to the air TM, we attribute the higher concentration of low SIM eigenvalues in Fig. 6.6(c) to both the mesoscopic correlations in the ZnO TM and the non-unitarity of the air matrix. Furthermore, randomization of the phases does not change the radius of the eigenvalue distribution $\{|\lambda_i|\}$, but it does suppress the largest SIM eigenvalues $\{|\alpha_i|\}$.

We therefore conclude that there exists a correlation between the TM of air and the TM of ZnO, which is plausible since even at about 7 mean free paths the sample TM contains some signature of the ballistic light. Additionally, the features of the SIM eigenvalue spectrum show effects of mesoscopic correlations in the scattering sample and of the deviation of the reference matrix from unitarity.

6.5 Avoidance of scatterers

By definition, SIMs are waves that exhibit the same transmitted wavefront through a scattering medium as through a non-scattering reference medium. This makes it plausible that SIMs avoid the scatterers in the scattering sample especially if the sample is sparse, i.e., it has scatterers separated by scatter-free regions. In this section, we investigate whether the SIMs do in fact avoid the scatterers. Since we cannot optically image inside a thick medium, we test our hypothesis on two cases of sparse scattering: a single scattering layer strewn with holes and a sample consisting of two such individual layers separated by a few microns.

6.5.1 Single scattering layer

We first investigate a single ZnO layer with several clearly identifiable air holes. Such a layer is found by looking at a transitional area on the sample (similar to the scattering ones described earlier) that lies between the thicker ZnO layer and a clean part of the glass slide. The LED image of the sample in our experiment is depicted in Fig. 6.7(a). The photograph is taken in a reflection configuration, so the dark areas correspond to the holes in the sample. This is also confirmed by Fig. 6.7(b), which shows the sum of all transmitted intensities of the incident focused spots on a hexagonal grid. It is clear that there is less transmitted light at the position of the scatterers. In fact, the positions of the scatterers, marked in red, are selected as the points of the hexagonal grid inside the delineated circle where the transmitted intensity is smaller than 65% of the maximum intensity. The value of 65% is chosen for this specific sample because it successfully identifies the scatterers visible in the microscopy image in Fig. 6.7(a). The circle represents the area in which the TM is measured in the Bessel basis. We find that 13% of this area is covered with scatterers.

We compute the SIMs of this sample by measuring the TMs of this layer and of a zero-thickness medium in a Bessel basis. As explained in Chapter 3, the TM of a zero-thickness layer includes only far-field contributions. The eigenvalue spectrum for the one-layer ZnO sample is plotted in Fig. 6.8(a). Since the scattering area comprises only 13% of the total area, it is not surprising that most

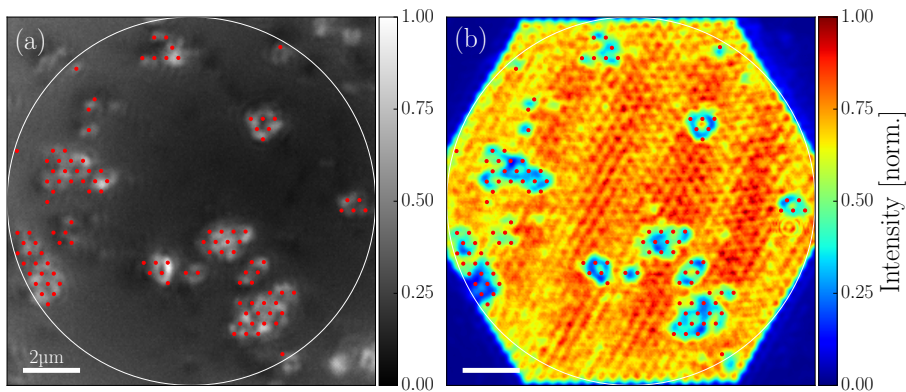


Figure 6.7: (a) Photograph of a single sparse ZnO layer taken in reflection with camera C3 by LED illumination (see Fig. 3.3). (b) Normalized sum of the transmitted intensities of all incident scan spots when performing the TM measurement. The red dots are the points on the hexagonal grid that correspond to the scatterer positions, and the circle indicates the region where the TM Bessel functions are defined. The scatterers occupy 13% of the area inside the circle.

eigenvalues are large and with phases peaked at zero instead of being random as in thick scattering samples. The cosine similarity of the SIMs exiting the sample and an equivalent zero-thickness medium are shown in Fig. 6.8(b), and we observe that 98% of all SIMs have a similarity higher than 0.5, which is the threshold we choose to separate similar and dissimilar SIMs. This is impressive because it is much higher than the clear area fraction of 87%. As observed in Section 6.3, the SIMs with high eigenvalues have the highest similarity and those with near-zero eigenvalues have a low signal-to-noise ratio and thus do not exhibit any resemblance.

For such a sparse sample, the “scattering” medium is equal to the reference medium for light propagating through the holes. We therefore expect the SIMs with the best cosine similarity and with high eigenvalues to propagate through the holes. To verify this hypothesis, we propagate the computed SIMs digitally through the sample by multiplying them with the measured TM of the sample. The two-dimensional spatial profile of the transmitted SIM is obtained by summing the Bessel functions with the appropriate complex coefficients obtained from the transmitted SIM in vector form. Finally, we superimpose the incident triangular lattice on this 2D intensity image and investigate the amount of light that falls on the grid points that correspond to the scatterers. In this way, we find the light that is propagated through the scatterers. For SIMs with a high

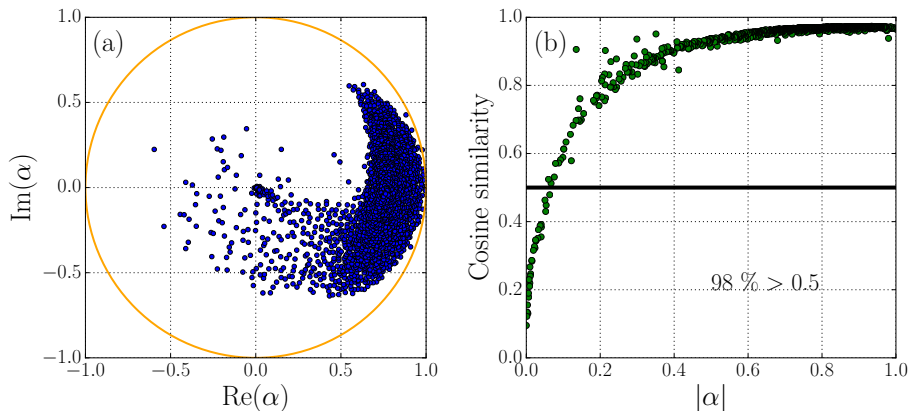


Figure 6.8: (a) Distribution of the complex eigenvalues for the single layer sample shown in Fig. 6.7. The unit circle of radius 1 is a guide to the eye. (b) Cosine similarity of the transmitted SIMs through the single layer and through a zero-thickness medium as a function of the eigenvalue modulus $|\alpha|$. The horizontal line at a similarity of 0.5 is our selected cutoff below which the fields are deemed not to resemble each other sufficiently. 98% of the SIMs lie above this line.

similarity, this is equivalent to studying the fraction of the incident light that falls on the scatterers because the field in air is completely ballistic. This is not the case for dissimilar SIMs, where we might underestimate the interaction due to a lack of knowledge about the backscattered light. Nonetheless, we are only interested in the properties of SIMs that have high similarity and hence our method of looking at the fraction of light that shines through scatterers is meaningful.

We perform this analysis for all the calculated SIMs and the results are encapsulated in Fig. 6.9. In (a), the fraction of the SIM intensity that shines through the scatterers is plotted as a function of the eigenvalue magnitude, where the color of the data points indicates the cosine similarity of the associated SIM. The dashed horizontal line at 13% represents the fractional area covered by scatterers. On average, an arbitrary wave has 13% of its intensity land on the scatterers. We notice that most eigenstates with large eigenvalues ($|\alpha| > 0.6$) lie below the dashed line, and several of them barely interact with the scatterers. This agrees with our prediction that the best transmitted SIMs propagate through the holes in the sample without interacting with the individual scatterers. The low SIMs ($|\alpha| < 0.1$) exhibit poor similarity and are drowned out by the noise, so we do not consider them. SIMs in the intermediate range ($0.1 < |\alpha| < 0.6$) interact more with the scatterers and thus transmit less

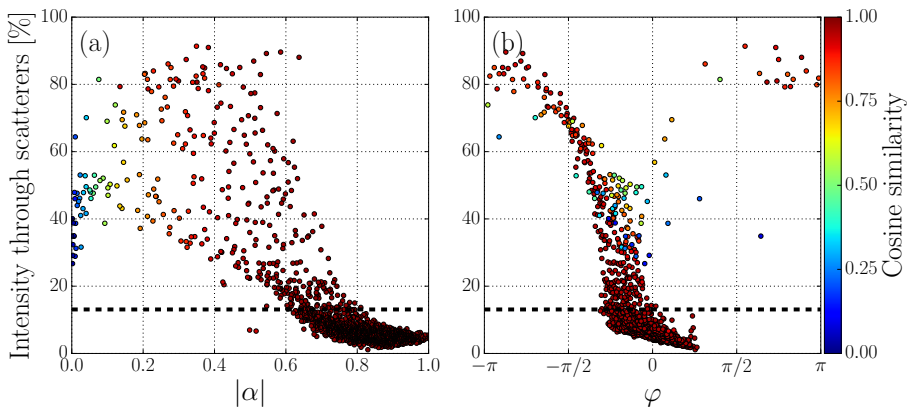


Figure 6.9: Percentage of the SIM intensity that shines through the scatterers as a function of the SIM (a) magnitude $|\alpha|$ and (b) phase φ . The color of the dots represents the cosine similarity of the transmitted SIMs plotted in Fig. 6.8(b). The dashed horizontal line indicates the area percentage (13%) occupied by the scatterers.

and possess a smaller eigenvalue. However, despite passing through scatterers, they still have a high similarity with the same waves propagated through air. The reason for this is that the sample is effectively a zero-thickness layer containing scatterers that are not a 100% opaque (see the transmission image in Fig. 6.7(b)), so light passing through these scatterers loses amplitude due to backscattering and sideways scattering, leading to light missing the detected aperture. The forward propagating light is not significantly distorted apart from this loss and a phase shift. Consequently, the eigenvalue is smaller depending on the transmitted amount but the similarity is not notably affected.

The information on the degree of interaction with the scatterers is more obvious in Fig. 6.9(b), which plots the same data as in (a) but as a function of the eigenvalue phase. The phase is the global phase delay experienced by the SIM passing through the scattering sample with respect to a zero-thickness layer. All SIMs below the dashed line have a phase close to zero because they avoid the scatterers and essentially propagate through air. If we neglect the SIMs with low cosine similarity, we observe that for SIMs that interact more and more with the scatterers, the phase delay gradually deviates from zero. The most interacting SIMs (around 80%) have close to a π -phase shift compared with those that miss the scatterers. We can safely conclude from both plots that the SIMs with high eigenvalues almost entirely avoid the scatterers, while the ones with lower eigenvalues interact more with the scatterers without loss of their similarity property.

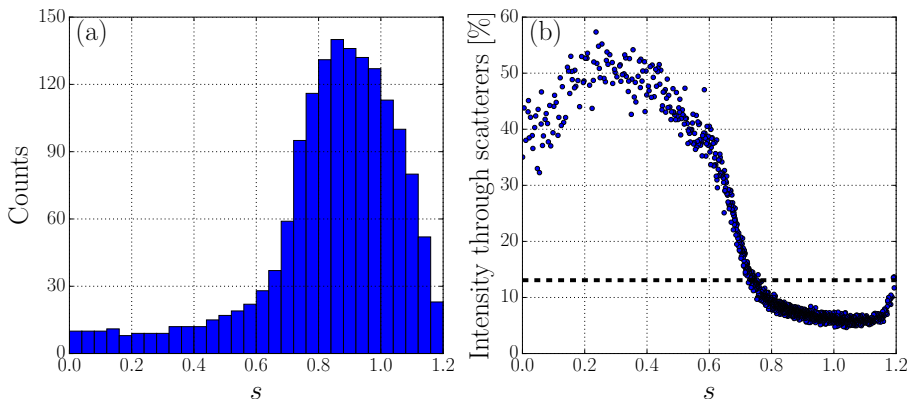


Figure 6.10: (a) Singular value histogram of the scattering layer. (b) The intensity of light that is transmitted through the scatterers as a function of the singular value s of the channel. The dashed horizontal line indicates the area percentage (13%) occupied by the scatterers.

We next compare the overlap of the SIMs with the scatterers to the same property of transmission channels of the single scattering layer. The open channels strictly avoid backscattering, so they can be hypothesized to avoid scattering altogether in sparse samples. The TM of the sample yields the singular value histogram plotted in Fig. 6.10(a). Since the layer is sparse, the distribution looks similar to that of a zero-thickness medium but with a few additional low singular values (closed channels) that are attributed to the scattering. The singular values are normalized with respect to the RMS value of a zero-thickness clear medium instead of the maximum value. Values larger than 1 occur due to noise (see Chapter 3).

For channels, we find the intensity spread on the scatterers as shown in Fig. 6.10(b). The open channels (with large singular values) fall below the dashed line to a value of about 5%. This is a small value, but not as small as in the case of SIMs where many have lower interaction. The upturn towards singular values of 1.2 correspond to unphysical states. They are artefacts of camera noise, as is confirmed by their spatial profile which contains unrealistically high spatial frequencies. These noise artefacts survive averaging in the matrix product $T_s^\dagger T_s$ [6]. The nonphysical states did not appear for the SIMs because in that case we have a product $T_{\text{air}}^\dagger T_s$ involving different matrices, so the noise does not cancel out. The intermediate and closed channels interact more with the scatterers, but they don't exceed an overlap of 60% whereas the SIMs went up to 90%. There seems to be little vertical spread in the plot, indicating that the channels with similar transmittance have around the same

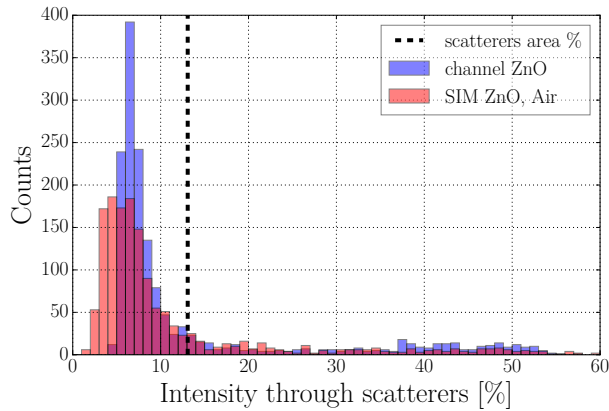


Figure 6.11: Histograms of the intensity percentage passing through the scatterers for the SIMs and the transmission channels. The dashed vertical line indicates the scattering area percentage (13%).

overlap with the scatterers. This is not the case for SIMs.

Since the point density in the scatter plots in Figs. 6.9 and 6.10 is hard to gauge by eye, the histograms in Fig. 6.11 are more revealing when comparing the SIMs and the transmission channels. Surprisingly but clearly, the best SIMs avoid the scatterers much better than the channels: we find that 359 SIMs (nearly a quarter) appear before the least interacting channel at 4.64%. The SIMs are designed to maintain their spatial profile, so we hypothesize that they achieve this best by emerging through the holes in the sample. On the other hand, as the open channels are constructed to maximize light transmission they find every possible way of passing through, even if it means deflecting off scatterers. Nonetheless, both types of waves are efficient in circumventing disorder in thin samples since just over 75% of both of them lie to the left of the dashed vertical line, which corresponds to the average scattering experienced by a random wave.

A visual proof of these observations is to study the spatial profiles of individual transmitted SIMs and channels through the single layer. Representative ones corresponding to large, intermediate and small transmission coefficients are depicted in Fig. 6.14. We clearly notice that the highly transmitting SIM in (a) circumvents the regions containing scatterers as there is practically no light in those regions. The open channel in (b) also prefers emerging through the holes, but the contrast in the intensity on the scatterers and off them is not as large. In the intermediate region, we see that both the SIM and the channel in (c) and (d) are “attracted” to the scatterers, and this tendency gets even more pronounced for the low SIM and closed channel in (e) and (f).

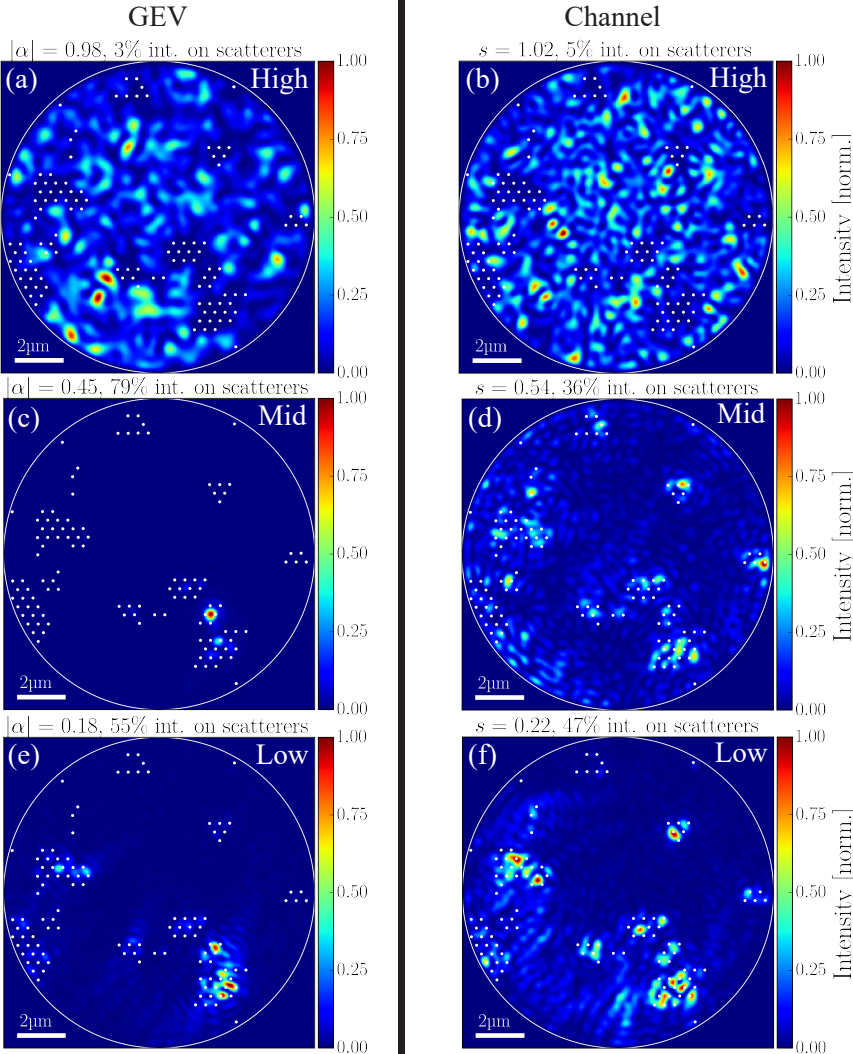


Figure 6.12: Normalized spatial intensity profiles of the transmitted SIMs (left) and channels (right) through the ZnO layer. They correspond to (a,b) high, (c,d) medium and (e,f) low transmission coefficients. The exact values are mentioned at the top of each image along with the intensity percentage that shines through the scatterers, which are marked with the white dots. The circle is the boundary of the area where the TM is probed.

6.5.2 Double scattering layer

We have established that high-transmission SIMs avoid scatterers for a single scattering layer. Since we are interested in 3D samples, we study next a sample that has 3D characteristics and yet allows imaging of the scatterers. In our case, the sample consists of two sparse layers separated by a non-scattering medium. As long as there is a small area percentage of scatterers, we expect the SIMs with high eigenvalues to pass through the holes and resemble the same wave in air. For that to be true, we hypothesize that the thickness of the reference medium at which the SIM avoids scatterers best should be equal to the optical sample thickness.

The configuration of the two-layer sample we have in our case, depicted in Fig. 6.12, consists of two single ZnO layers separated by a Mylar sheet with an approximate thickness of $6\ \mu\text{m}$. Mylar, which is a well-known brand name of a stretched polyester film, is a suitable material because it is transparent, non-scattering and robust to temperature fluctuations. Compared to the depth of field of the high-NA microscope objectives, which is less than $1\ \mu\text{m}$, the thickness of the Mylar sheet is much larger and hence the field profiles at either face of the sheet are completely dissimilar. The experimental scheme is therefore suitable to detect the scattering avoidance of SIMs at two independent layers.

The sample is prepared by first spraying a single layer of ZnO on a glass slide, which is achieved by spraying for a short duration of around five seconds. Once this layer has dried, we clean the borders of the glass slide of ZnO nanoparticles and apply optical glue all around the edges. We then lay a Mylar sheet on top of the glass slide and try to keep it as taut as possible to prevent the formation of air gaps between the nanopowder and the Mylar. Subsequently, we UV-cure the glue for three minutes so that the Mylar sheet remains firm in place. The

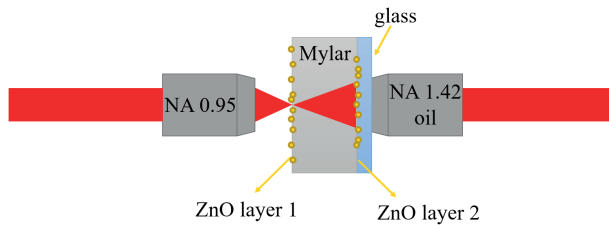


Figure 6.13: Sketch of the experimental configuration. Two weakly scattering layers consisting of ZnO nanoparticles are separated by a Mylar sheet. The double layer is glued to a microscope cover glass. The incident laser beam is focused on the front surface with a 0.95-NA air microscope objective, and the scattered light is imaged at the second surface with a 1.42-NA oil immersion objective.

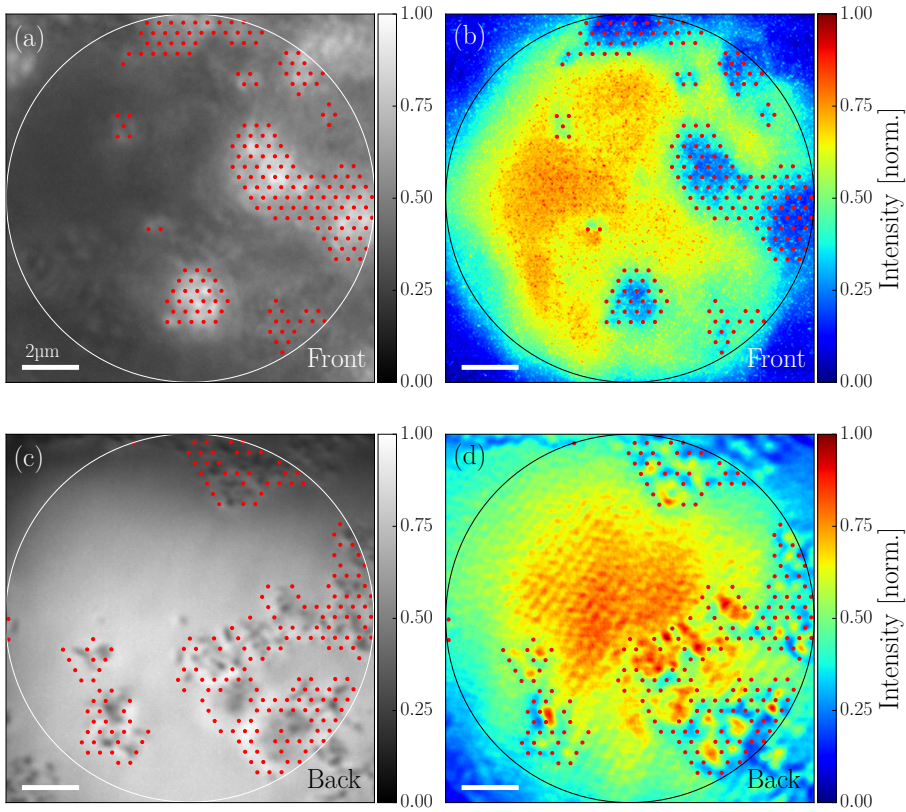


Figure 6.14: Double layer scattering sample. LED images of the (a) front and (c) back surfaces along with (b,d) the intensity sum of the transmitted incident spots on these surfaces. The red dots represent the grid points at scatterer positions and the circle defines the TM measurement area. 24% of both layers is occupied by scatterers.

second ZnO layer could also be realized by spraying, but for the sample used in this section, we chose to dust the nanopowder on the Mylar. To do this, we place the sample with the Mylar sheet facing up in a box and put some ZnO powder in a corner. We then blow on the ZnO with an air gun, resulting in the particles flying around in the box and getting deposited on the Mylar. The powder clings on robustly to the Mylar, and we keep blowing until a second ZnO layer is sufficiently formed.

The LED image of the front and back surfaces is depicted in Fig. 6.13 along with the corresponding sum of intensities of the incident spots on each of these two surfaces. The position of the scatterers are established by looking at the

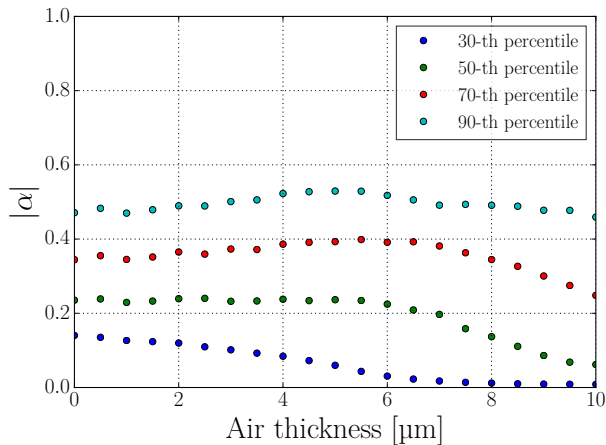


Figure 6.15: 30th, 50th, 70th and 90th percentiles of the SIM magnitudes $|\alpha|$ of the two-layer sample as a function of the thickness of the air layer in microns.

areas where there is low transmitted intensity. Each layer has a scatterer area fraction of 24%, so a random wave will overlap 24% with scatterers on both surfaces. The thickness of the sample, measured by focusing on both surfaces with the microscope objectives, is 8846 ± 200 nm. Since a stretched Mylar film becomes birefringent [14], we restrict ourselves to measuring only the HH polarization component of the TM of the sample. In spite of this limitation, we are still able to study whether the calculated eigenstates avoid the scatterers.

To calculate the SIMs of this sample with an air reference TM, we would like to know what is the best thickness of air to choose. Hence, we measure the TM of air for thicknesses going from 0 to 10 μm in steps of 0.5 μm , and subsequently calculate the SIMs using all these air TMs. To decide which is the best equivalent thickness of air, we investigate whether the magnitude of the SIMs peak for some air thickness. Fig. 6.15 shows some different percentile values of the SIM modulus as a function of the air thickness. We observe that the 90th percentile, which represents highly transmitting eigenstates without including outliers, has a maximum at a thickness of 5 μm . This is smaller than the measured thickness of 8.8 μm of the two-layer sample because the material in between is Mylar and not air. Since Mylar has a refractive index between 1.64 and 1.67, its effective thickness is approximately $8.8/1.65 \approx 5.3$ μm . However, the maximum at 5 μm is not sharp and suggests that the choice of the best equivalent thickness is not crucial. The lower percentile values have hardly any observable maximum and are not as sensitive to the air thickness unless we pick values greater than 6 μm , where we observe that the SIM magnitude drops

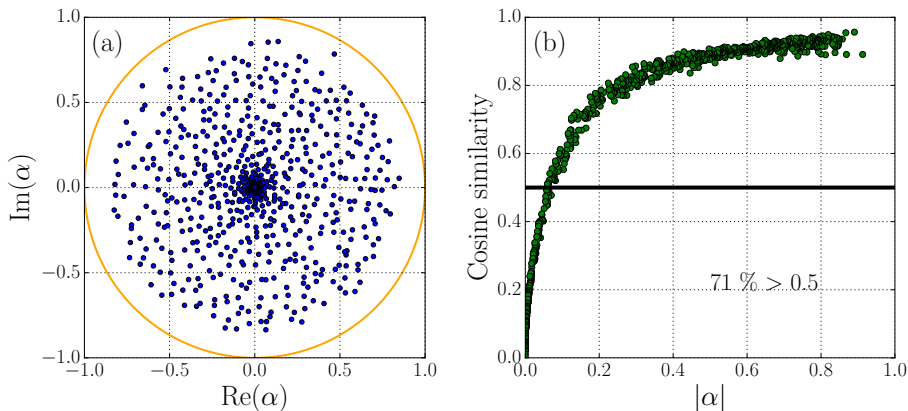


Figure 6.16: (a) Complex SIM eigenvalue spectrum for the double layer sample and 5 μm -air. The circle represents the unit circle with radius 1. (b) Cosine similarity of the transmitted SIMs through the sample and through air as a function of the eigenvalue modulus $|\alpha|$. 71% of the SIMs have a similarity higher than 0.5.

rapidly because part of the air field propagates outside the field of view. Since we saw in the one-layer case that the highest transmitting SIMs avoid scatterers most effectively, we consider only the 90th percentile and therefore take the best equivalent thickness of air as 5 μm .

The complex SIM eigenvalue spectrum and the cosine similarity of the transmitted fields through the sample and air (predicted from the TMs) are plotted in Fig. 6.16. Compared to the single layer sample, there are many more eigenvalues close to zero because there is more scattering and parts of the light propagating through the thicker sample fall outside the region where the TM is measured. The scattering also results in randomizing the phase of the eigenvalues. For the same reason, the transmitted fields through the sample and through 5 μm of air correlate less well. Nevertheless, 71% of them correlate higher than 0.5.

We digitally propagate the calculated SIMs through the two-layer sample and find the intensity through the scatterers as in the previous subsection. The results are summarized in Fig. 6.17, where the intensity percentage plotted is the average of the intensity percentages on the first and second layers. In (a), we notice that there are fewer SIMs under the dashed line (at 24%) than in the single layer, which intuitively can be explained by the notion that in a higher density of scatterers it is harder to avoid them all. Nonetheless, we observe the same trend that the states with the largest eigenvalues avoid the scatterers the best, while those with small ones hit the scatterers more. Unlike the mono-layer, the distribution of the intensity percentages are not as dispersed and follow a

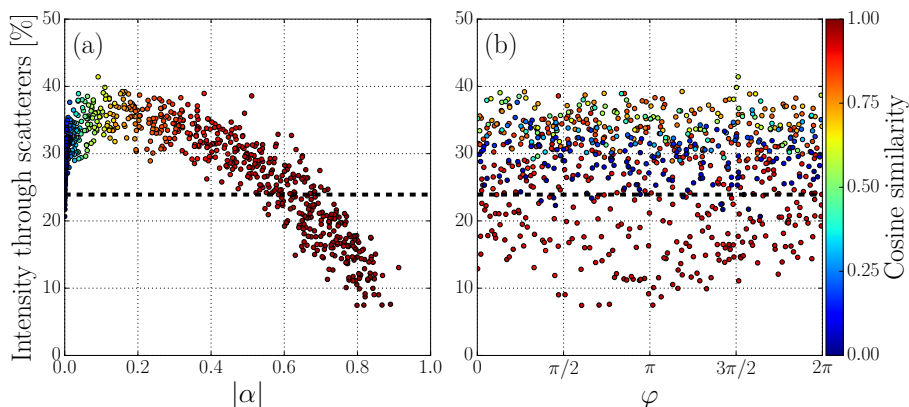


Figure 6.17: Intensity percentage that shines through the scatterers as a function of the SIM (a) magnitude $|\alpha|$ and (b) phase φ . The color of the dots represents the cosine similarity. The dashed horizontal line indicates the total area percentage (24%) occupied by the scatterers on both layers.

monotonous trend. In Fig. 6.17(b) however, the phase dependence is not clear since the eigenvalues themselves are spread out more or less randomly over all phase space.

The spatial profiles of some of the SIMs at the front and back surfaces of the double layer scattering sample are depicted in Fig. 6.18. The high SIM clearly avoids the scatterers on the first and second surface (a,d) and its spatial profile is visibly localized. The mid-range SIM (b,e) finds more of its intensity on the scatterers and its spatial profile is much wider, but it still correlates higher than 80% with its counterpart through 5 μm of air. The low SIM (c,f) looks similar to the intermediate one but correlates less well. Its intensity on the second surface lies mostly on the boundary of the TM measurement area.

To compare again how the SIMs fare with respect to the channels of the two-layer sample, we study the scattering avoiding properties of the channels displayed in Fig. 6.19. In (a), which plots the channel intensity percentage that lands on the scatterers, we observe that apart from the noisy low singular values ($s < 0.1$) the interaction reduces with higher transmission of the channels. The minimum interaction is around 10%. The upturn at the largest singular values correspond to unphysical eigenstates as can be confirmed by looking at their spatial profiles. A handful of SIMs have less than 10% interaction, as can be seen in the histogram of the channel and SIM intensity on the scatterers in Fig. 6.19(b). We observe a peak for the channels at a low overlap with the scatterers which rises far above the SIMs distribution. This indicates that a

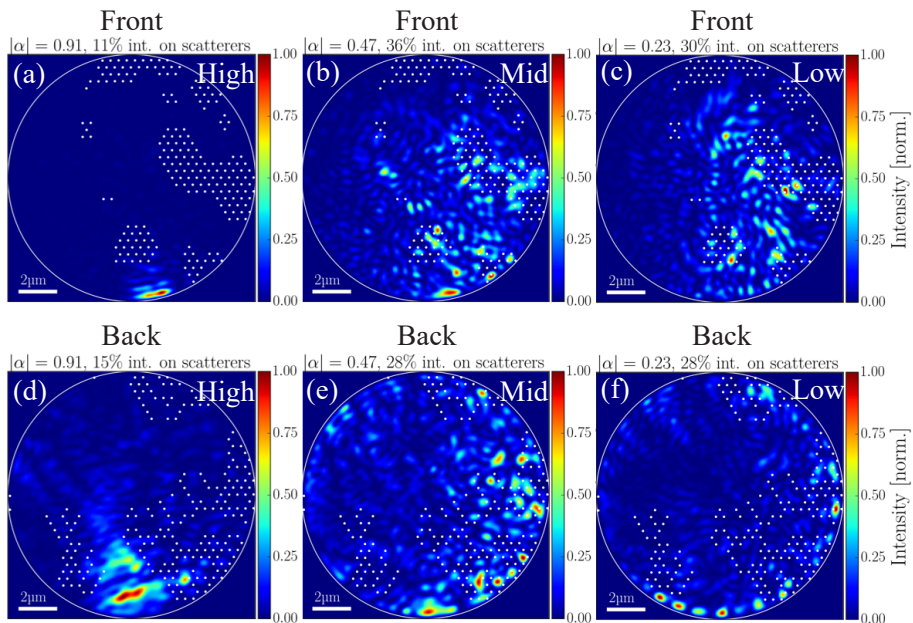


Figure 6.18: Normalized spatial intensity profiles of the high, mid-range and low SIMs at the (a-c) front and (d-f) back surfaces of the double layer. The eigenvalue modulus is mentioned at the top of each image along with the intensity percentage that is transmitted through the scatterers, which are marked with the white dots. The circle is the boundary of the area where the TM is defined.

larger number of channels experience reduced scattering compared to SIMs.

Finally, we compare the spatial widths of the transmission channels and SIMs in Fig. 6.20. The width w is calculated as the standard deviation of the intensity values inside the measurement region

$$w = \sqrt{\frac{1}{\iint dx dy I(x, y)} \iint dx dy I(x, y) \cdot [(x - \mu_x)^2 + (y - \mu_y)^2]}, \quad (6.6)$$

where x and y are the pixel coordinates, $I(x, y)$ is the intensity value at the position (x, y) , and μ_x and μ_y are the centroids in the x - and y -directions given

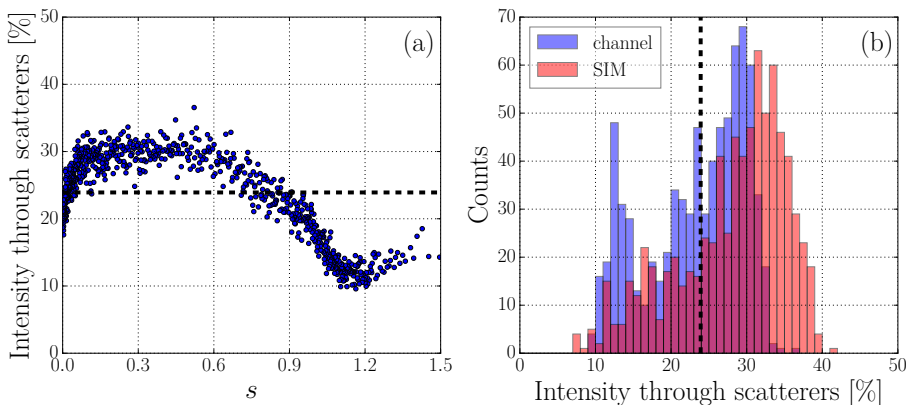


Figure 6.19: (a) The intensity of light that shines through the scatterers as a function of the singular value s of the channel. (b) Histogram of the channel and SIM intensity percentages through the scatterers. The dashed line indicates the total area percentage (24%) occupied by the scatterers.

by

$$\mu_x = \frac{1}{\iint dx dy I(x, y)} \iint dx dy I(x, y) \cdot x, \quad (6.7)$$

$$\mu_y = \frac{1}{\iint dx dy I(x, y)} \iint dx dy I(x, y) \cdot y. \quad (6.8)$$

We look here at the width of the fields incident on the sample, i.e., on the first surface. For the channels, we notice that excluding the high unphysical singular values ($s > 1.1$), the large transmission coefficients correspond to smaller widths, and vice versa. This behavior agrees with the recent observations reported by Yilmaz *et al.* [15], albeit the authors calculated the width as an inverse participation ratio (IPR). The SIMs follow a similar trend, but the greatest difference between the SIMs and channels is that the highest SIMs possess a width which is smaller than that of the most open channels. Most of the other SIMs are also narrower than their channel counterpart when ordered by transmission coefficient. This shows that the SIMs are more transversally confined waves than the open channels for a weak scattering medium, especially the ones with high transmission.

In summary, we observe that for a sparse double-layer sample, the SIMs with high transmission are spatially more confined than random waves and avoid scatterers most efficiently on both surfaces simultaneously. However, the use of a Mylar film in our sample has certain limitations. First, in the

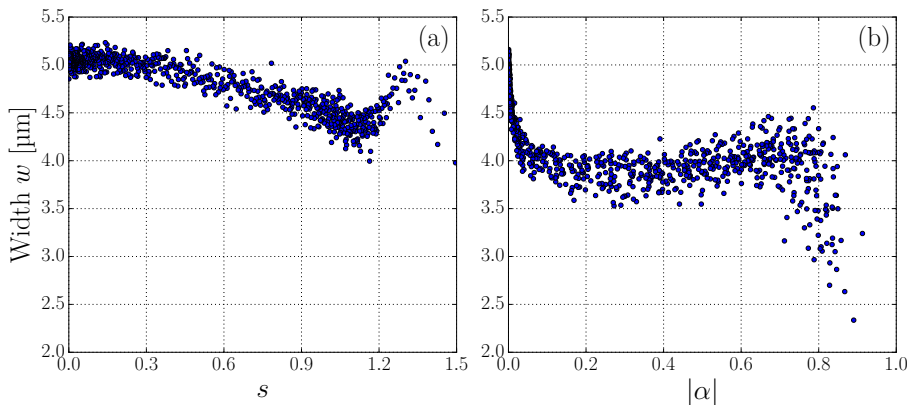


Figure 6.20: Spatial width w of the (a) channels and (b) SIMs incident on the first surface as a function of the singular value s and eigenvalue $|\alpha|$ respectively. The widths are calculated according to eq. (6.6).

way we fabricate our sample, there exist air pockets between the Mylar sheet and the underlying glass slide which induce unwanted internal reflections at these interfaces with a high refractive index contrast. This also results in a nonuniform local thickness that can cause a reduced cosine similarity between the waves transmitted through the sample and through air. Second, Mylar is birefringent and therefore the polarization of an incident field on a plain Mylar film is not the same as it passes through the non-scattering layer. This prevents us from measuring SIMs of the polarization-resolved TM with a clear reference. Finally, we used air as the reference medium and not a clear Mylar film because measuring its TM is hard due to the aforementioned reasons as well as the difficulty of focusing light on its clean surface with a very low reflection coefficient.

6.6 Conclusion

We have shown here the first observation of scattering invariant modes (SIMs), which are waves that are transmitted with the same spatial profile through air and a strong scattering medium. We found these SIMs by measuring the transmission matrices of air and a scattering layer of ZnO nanoparticles. We successfully projected them through both media using digital holography and the complex transmitted fields had a similarity as high as 0.72. We also showed that the SIMs are sensitive to the transport physics of the sample because the statistics of their eigenvalues are partially explained by transport theory.

Finally, we also observed that in sparse scattering samples, SIMs with large eigenvalues circumvent disorder by avoiding the scatterers and are more confined than the most open transmission channels. The remarkable properties of the SIMs make them a suitable candidate to understand the dynamics of ballistic light in disordered media.

Bibliography

- [1] I. M. Vellekoop and A. P. Mosk, “Focusing coherent light through opaque strongly scattering media,” *Opt. Lett.* **32**, 2309–2311 (2007).
- [2] A. Mosk, A. Lagendijk, G. Lerosey, and M. Fink, “Controlling waves in space and time for imaging and focusing in complex media,” *Nature photonics* **6**, 283–292 (2012).
- [3] S. Rotter and S. Gigan, “Light fields in complex media: Mesoscopic scattering meets wave control,” *Rev. Mod. Phys.* **89**, 015005 (2017).
- [4] S. Popoff, G. Lerosey, M. Fink, A. C. Boccarda, and S. Gigan, “Image transmission through an opaque material,” *Nature Communications* **1**, 81 (2010).
- [5] P. Pai, J. Bosch, M. Kühmayer, S. Rotter, and A. P. Mosk (in preparation).
- [6] M. Tanter, J.-L. Thomas, and M. Fink, “Time reversal and the inverse filter,” *The Journal of the Acoustical Society of America* **108**, 223–234 (2000).
- [7] M. Nieto-Vesperinas, *Scattering and Diffraction in Physical Optics*, 2nd Edition (World Scientific Publishing Company, 2006).
- [8] J. Bosch, S. A. Goorden, and A. P. Mosk, “Frequency width of open channels in multiple scattering media,” *Opt. Express* **24**, 26472–26478 (2016).
- [9] W.-H. Lee, “Binary synthetic holograms,” *Appl. Opt.* **13**, 1677–1682 (1974).
- [10] O. Dorokhov, “On the coexistence of localized and extended electronic states in the metallic phase,” *Solid State Communications* **51**, 381 – 384 (1984).
- [11] P. Mello, P. Pereyra, and N. Kumar, “Macroscopic approach to multichannel disordered conductors,” *Annals of Physics* **181**, 290 – 317 (1988).
- [12] C. W. J. Beenakker, “Random-matrix theory of quantum transport,” *Rev. Mod. Phys.* **69**, 731–808 (1997).
- [13] J. Ginibre, “Statistical ensembles of complex, quaternion, and real matrices,” *Journal of Mathematical Physics* **6**, 440–449 (1965).
- [14] E. F. Borra, R. Content, C. Delisle, and J. Gauvin, “Optical tests of thin plastic films,” *Publications of the Astronomical Society of the Pacific* **104**, 1239 (1992).
- [15] H. Yılmaz, C. W. Hsu, A. Yamilov, and H. Cao, “Transverse localization of transmission eigenchannels,” *Nature Photonics* **13**, 352–358 (2019).

7 Summary and outlook

In this thesis, we have investigated statistics of light propagation through a medium by measuring the transmission matrix (TM) of the medium sampled in a basis that minimizes crosstalk. We have shown in our work that the sampled TM decouples the sample from aberrations and misalignment of the optical setup and is a faithful probe to describe the underlying physics of the sample. This provides a high degree of control which can not only be used for imaging purposes, but also to understand the mesoscopic transport physics inside complex media.

First, to remove any ambiguity of the definition and interpretation of the optical TM, we have given an explicit relation of the TM with the transmission operator and the Green's function, which is a mathematically rigorous concept that is well-known in literature. We showed that the TM is band-limited and, unlike the Green's function, does not contain the near-field information. However, the beauty of the TM is that it is a powerful tool that does not require to possess any knowledge of the internal structure of the scattering medium or the near-field terms of the scattered light field.

Experimentally, we have made significant improvements on previously used methods enabling us to accurately measure a large portion of the TM almost free of sampling artefacts. We showed that sampling the TM at the Rayleigh criterion using a basis of Airy spots on a hexagonal lattice exhibits the least crosstalk at the same density of all real space and k -space lattices. We validated our sampling scheme by measuring the polarization-resolved TM of a zero-thickness reference, where the incident and transmitted fields lie on the same plane. Our results were in good agreement with numerical calculations.

The measured matrix in an Airy spot basis describes the system including optical aberrations and misalignment. To isolate the TM of the sample from that of the optical setup, we further improved our method by resampling the matrix into a basis of Bessel modes of the first kind that is orthogonal and complete on a circular area barring edge effects. We compared the measurements performed in the spatial and Bessel bases and demonstrated that the TM in the Bessel basis provides a more accurate representation of the actual system. In the process, we serendipitously discovered a direct analogy between the eigenvectors of the TM of air and the Fox-Li modes of a confocal and lossy optical cavity. We found that in the spot basis, which contains system imperfections,

the transmission eigenvectors are Ince-Gaussian modes, which also appear in asymmetric cavities. Moreover, the aberration-corrected Bessel basis yields the principal modes of propagation in air which coincide with the true Fox-Li modes of a cylindrically symmetric resonator.

Next, using the established Bessel mode basis, we measured the TM of a strongly scattering isotropic layer of zinc oxide (ZnO) nanopowder. The resulting singular values, representing the transmission coefficients of the transmission channels, reveal the presence of strong mesoscopic correlations in the medium that are non-existent for a random Gaussian matrix. In a sample with a thickness of 10 μm , we found “open” channels that have more than 6 times greater intensity transmission than an average channel, and “closed” channels that have practically zero transmission. We also observed mesoscopic correlations of the medium through the intensity statistics of the transmitted speckle profiles of the individual channels of the TM. Additionally, we noticed that we systematically observe decreased correlations when the incident field couples to a higher number of channels. This confirms that the observed correlations are due to coupling to a single or few channels of the transmission operator.

As a probe to understand ballistic light, we used the transmission matrices of a diffuse medium and of air to find waves that exit with the same spatial profile through both media. These special waves, which we refer to as scattering invariant modes (SIMs), effectively pass through the scattering medium as if it were non-existent. We successfully calculated these SIMs from the measured TMs of the scattering layer and of air, projected them through both media experimentally and observed a cosine similarity as high as 0.72. Additionally, we noticed that in sparse scattering media, the highly transmitting SIMs circumvent disorder by avoiding the scatterers and are spatially more confined than the most open channels.

As an outlook, possible future explorations that can follow this work are the distribution of transmission channels in the presence of absorption or for different samples, e.g. anisotropic samples, photonic crystals and colloidal systems. Reflection matrices, and subsequently scattering matrices, can also be measured with the same procedure and yield more understanding of light transport. Moreover TMs can be used for practical applications such as imaging [1, 2], security [3], precision measurements [4], and to perform computations of interest to machine learning and artificial intelligence [5]. Eventually, our novel method of measuring TMs yielding accurate eigenchannel statistics could pave the way to discover mesoscopic effects at the single channel level, leading to possible new observations not yet explored by theory.

Bibliography

- [1] S. Popoff, G. Lerosey, M. Fink, A. C. Boccara, and S. Gigan, “Image transmission through an opaque material,” *Nature Communications* **1**, 81 (2010).
- [2] H. Yılmaz, “Advanced optical imaging with scattering lenses,” Ph.D thesis, University of Twente (2015).
- [3] S. A. Goorden, M. Horstmann, A. P. Mosk, B. Škorić, and P. W. H. Pinkse, “Quantum-secure authentication of a physical unclonable key,” *Optica* **1**, 421–424 (2014).
- [4] D. Bouchet, R. Carminati, and A. P. Mosk, “Influence of the local density of states on the localization precision of single particles in scattering environments,” (2019).
- [5] “LightOn,” <https://www.lighton.ai/> (2019).

Samenvatting en vooruitzichten

In dit proefschrift wordt de statistiek achter lichtpropagatie door een medium onderzocht door het meten van de transmissiematrix (TM) van dit medium, in een basis waarin overspraak geminimaliseerd is. We laten zien dat de bemonsterde transmissiematrix het monster ontkoppelt van afwijkingen in, en foutieve uitlijning van, het optisch systeem en een betrouwbaar meetmiddel is om de onderliggende fysica van het monster te beschrijven. Dit levert een hoge mate van controle welke niet alleen gebruikt kan worden om af te beelden, maar ook om de mesoscopische transporteigenschappen in een complex medium te begrijpen.

Ten eerste, om dubbelzinnigheid in de definitie en interpretatie van de optische TM te voorkomen, geven we een expliciete relatie tussen de TM en de transmissieoperator en Greense functie, welke een wiskundig rigoreus en in de literatuur wel-bekend concept is. We laten zien dat de TM bandbreedtebegrensd is en, in tegenstelling tot de Greense functie, geen informatie bevat over het nabije veld. Daarentegen is de TM een krachtig stuk gereedschap welke geen kennis behoeft over de interne structuur van het verstrooiende medium of de nabije-veld termen van het verstrooide lichtveld.

Op experimenteel gebied hebben we significante vooruitgang geboekt op eerder gebruikte methoden, waardoor het ons mogelijk is om met hoge precisie een groot deel van de TM te meten, vrijwel vrij van bemonsteringsartefacten. We laten zien dat, van alle bemonsteringsschema's in de reële ruimte en de k -ruimte, het bemonsteren van de TM aan de hand van het Rayleigh criterium, gebruikmakend van een basis van Airy schijven op een hexagonaal rooster, de minste overspraak oplevert voor dezelfde bemonsteringsdichtheid. We bevestigen de correctheid van ons bemonsteringsschema door het meten van de polarisatie-opgeloste TM te meten van een referentiemonster van dikte nul, waarvan de inkomende en uitkomende lichtvelden in hetzelfde vlak behoren te liggen. De resultaten van deze referentiemeting komen overeen met numerieke berekeningen.

De in de Airy-schijfbasis gemeten matrix beschrijft het gehele systeem, inclusief optische abberaties en foutieve uitlijning. Om de TM van het monster te isoleren van de TM van het optische systeem verbeteren we onze methode nog verder, door de matrix opnieuw te bemonsteren op een basis van Bessel-functies van de eerste soort, welke orthogonaal en compleet is op een circulair gebied wanneer randeffecten worden verwaarloosd. We vergelijken de metingen

in de ruimtelijke en Besselbasis met elkaar en laten zien dat de TM in de Besselbasis een nauwkeurigere representatie van het echte systeem levert. Tijdens dit proces wordt per toeval ontdekt dat er een directe analogie is tussen de eigenvectoren van de TM van lucht en de Fox-Li toestanden van een confocale en lekkende trilholte. We ontdekken dat de transmissie-eigenvectoren in de Airy-schijfbasis, welke de onvolkomendheden van het systeem bevat, Ince-Gauss toestanden zijn, die ook voorkomen in asymmetrische trilholten. De voor afwijkingen gecorrigeerde Besselbasis bevat de voornaamste propagatietoestanden voor voortplanting van licht door lucht, welke gelijk zijn aan de echte Fox-Li toestanden van een cilindrisch-symmetrische resonator.

Vervolgens wordt in de Besselbasis de TM van een sterkverstrooiende, isotrope laag van zinkoxide (ZnO) nanopoeier gemeten. De singuliere waarden van deze TM, te interpreteren als transmissiecoëfficiënten van de transmissiekanalen, onthullen de aanwezigheid van sterke correlatie op mesoscopische schaal in het medium. Dergelijke correlatie is afwezig in het geval van een willekeurige Gaussische matrix. In een monster met een dikte van 10 μm ontdekken we “open” kanalen die meer dan 6 keer de hoeveelheid licht doorlaten dan een gemiddeld kanaal, en “gesloten” kanalen die praktisch geen licht doorlaten. Door de intensiteitsstatistiek van de specklepatronen van individuele kanalen te bestuderen ontdekken we correlaties van het medium op mesoscopische schaal. Bovendien worden systematisch minder correlaties waargenomen wanneer het inkomende lichtveld koppelt met een hoger aantal kanalen. Dit bevestigt dat de waargenomen correlaties het gevolg zijn van koppeling naar een enkel, of slechts een paar kanalen van de transmissieoperator.

Om ballistisch transport van licht door het medium te begrijpen worden de transmissiematrices van een diffuus medium en van lucht vergeleken, met als doel om golfvormen te vinden die het beide media verlaten met hetzelfde ruimtelijke profiel. Deze speciale golven worden hier verstrooiingsonafhankelijke toestanden (*scattering invariant modes* of SIMs) genoemd en planten zich door het verstrooiende medium voort alsof het er niet is. Deze SIMs worden met succes uit de voor lucht en voor een verstrooiend medium gemeten TMs berekend. Wanneer deze golven vervolgens door medium gestuurd worden wordt een cosinusgelijkenis tot 0.72 waargenomen. Bovendien wordt opgemerkt dat in media met weinig verstrooiende nanodeeltjes de SIMs met de hoogste transmissie de verstrooiende deeltjes missen en dat deze SIMs een kleiner gebied bestrijken dan de meeste open kanalen.

Toekomstig werk op basis van resultaten uit dit proefschrift kunnen zich richten op de verdeling van transmissiekanalen van absorberende monsters, zoals het geval is voor anisotropische monsters, fotonische kristallen en colloïdale systemen. Reflectiematrices, en hierop volgend verstrooiingsmatrices, kunnen

gemeten worden volgens dezelfde procedure en leveren nog meer inzicht in het transport van licht door dit soort monsters. Bovendien kunnen TMs gebruikt worden voor praktische toepassingen zoals het maken van afbeeldingen [1, 2], digitale beveiliging [3], precisiemetingen [4], en om berekeningen te doen op het gebied van machine learning en kunstmatige intelligentie [5]. Uiteindelijk kan onze nieuwe methode van het meten van transmissiematrices met nauwkeurige eigenkanaalstatistiek tot gevolg leiden tot de ontdekking van mesoscopische effecten op de schaal van slechts één kanaal, wat kan leiden tot ontdekkingen waar in de theorie nog geen uitspraak over is gedaan.

Bibliografie

- [1] S. Popoff, G. Lerosey, M. Fink, A. C. Boccara, and S. Gigan, “Image transmission through an opaque material,” *Nature Communications* **1**, 81 (2010).
- [2] H. Yilmaz, “Advanced optical imaging with scattering lenses,” Ph.D thesis, University of Twente (2015).
- [3] S. A. Goorden, M. Horstmann, A. P. Mosk, B. Škorić, and P. W. H. Pinkse, “Quantum-secure authentication of a physical unclonable key,” *Optica* **1**, 421–424 (2014).
- [4] D. Bouchet, R. Carminati, and A. P. Mosk, “Influence of the local density of states on the localization precision of single particles in scattering environments,” (2019).
- [5] “LightOn,” <https://www.lighton.ai/> (2019).

Acknowledgments

This thesis is only a partial representation of all the trial and errors, the frustrations and the little victories that culminated in the beautiful results presented in this book. I've matured as a scientist, a teacher, a guide and more importantly as a person. All of this would not have been possible without acknowledging several people, whose help and goodwill I've often taken for granted.

Firstly, I would like to thank my supervisor Allard for giving me the opportunity to pursue a PhD in his research group. Allard, it has been a great pleasure working with you during the last four years and I really appreciate your constant support and influx of creative ideas. I've learned to work a lot more independently thanks to your liberal style of guidance. Your eye for detail and thoroughness and your emphasis on quality has definitely made me a better scientist. The best thing I can say about you is that even though results took a while in coming, I've never once felt stressed under your supervision, and I think a big part of that stems from your excellent man-management skills.

It is only natural to extend my gratitude to Sanli, who co-supervised my PhD project. Sanli, when the NanoLINX group was formed in Utrecht four years ago, it started on a positive note and I give you massive credit for laying down all the practical groundwork that underlies a successful and organized research group. I marvel at your dynamism in trying out and implementing new ideas, and the best example of that is the innovative Experiment Design course that you created and which I greatly enjoyed being a part of.

A major part of my acknowledgments goes to my colleagues at the Nanophotonics Department, both past and present, without whom I could not have achieved what I did during my PhD. First, my partner in crime, Jeroen, who started on the same day as me and with whom I worked on different aspects of the same project. Jeroen, it has been a terrific ride together and you have been the perfect sounding board for all my scientific endeavors, ranging from discussing crazy "complex random" ideas to solving day-to-day technical issues. You're one of the most helpful members of our group and the countless number of hours you have spent trying to solve other people's problems in the lab is remarkable. This, along with your obsession of lab organization and safety, has made working in the lab a very pleasant experience for all.

Moving on to my office-mates, who have shared first hand all the normal highs and lows that accompany scientific research, I have only positive things

to say about them. Arjon, I will cherish all the interesting conversations we have had, especially on our common passion for sports and discussing all the latest news and highlights. Your cheerfulness and sense of humor has made my time in the office a memorable one. I also want to thank you for introducing me to “Dutch” culture. Sebas, aka the Python master, you were the other piece of the puzzle that made our office the social room. You brought the whole group together by taking the lead in organizing events and it was fun hanging out with you. I will always remember the one summer when we went for daily workout sessions during lunch, and when we finally got the entire Nanophotonics group to participate.

Jasper, thank you for influencing me with your enthusiasm and passion for science and for being loud and vocal about it. Bohdan, you are a great storyteller and came to life during borrels and group dinners. I’ve been entertained to some very fascinating and dark stories thanks to you. Dashka, I enjoyed our interactions and have some great memories of times when we spontaneously went out after work. Marcel, I admire that you always have an opinion of your own and appreciate that you were never bothered with me entering your office on countless occasions for various (at times non-scientific) reasons. Dorian, you are one the smartest people I know and I’m inspired at the sheer amount of time and effort you spend on your research. This wonderful energy along with the interest you show in everyone’s projects makes you a wonderful role model for anyone aspiring to be a successful scientist. Jacob, thanks for bringing up off-beat topics during lunch which often make me look at the world from a different perspective. Zhu, your constant smile is contagious and I’m always happy to listen to your interesting stories from China. Karindra, it’s impressive how you manage your time doing so many different things. You’ve taught me that it’s not impossible to pursue more than one passion seriously. Pegah, I appreciate your frankness in dealing with people and your push to make the group more social.

The Nanophotonics department would also not be same without the other PIs and support staff, who have a major role in ensuring a healthy research atmosphere. Peter, “my absolute hero”, I admire your honest and direct approach towards scientific research and education and will miss your sarcastic one-liners. I thoroughly enjoyed working with you as a teaching assistant for the Photon Physics course, and I applaud your openness to implement my suggestions. Dries, you’re the most colorful personality in our department and I’m in awe at your readiness to do new and crazy things! Your passion and dedication towards your hobbies rubs off on me as I aim to emulate your versatility in various activities. I appreciate that I could just walk into your office and start scribbling equations on your whiteboard. Mijke, you’ve been the most

wonderful secretary, always anticipating my needs and helping out even before I asked you for it! Your liveliness is the glue that binds the group together and I am fortunate to have someone with whom I can share the occasional coffee break without having to talk about science. Floor, thank you for guiding me through all the administrative tasks at the start of my PhD. The contribution of all technicians in my time here has been immense, and I've always felt welcome into their offices to ask for help. Dante, besides your technical help, I learned a lot from you both on a scientific and personal level. Thanks to your "phrase-a-week" routine, I've vastly improved my Dutch during my time here. "Ouwe" Paul, thank you for your patience and effort in designing mechanical components for my optical setup. You're always happy and greeting everyone on the floor, and so enthusiastic to organize borrels. Cees, you work like an efficient machine and I'm amazed how you follow up on all your tasks so diligently – the group is definitely going to miss you when you retire! Frits, I enjoyed our discussions on classical music and old Dutch expressions.

I cannot forget to thank some former colleagues who I have been fortunate to work with. Sergei, thank you for all your valuable tips and tricks when I was constructing my optical setup. You always made our coffee breaks fun and I recall some fun memories of spending time outside work. Sid and Abhi, we had plenty of open discussions and it was truly worthwhile to organize a couple of 1-week research workshops back in India. Javi, you are a great example of an independent scientist and I wish I could be as meticulous as you are. Diana, we share a lot of common interests and I still fondly remember our special interactions. I also had the great pleasure of supervising a couple of students. Arfor, you were always so eager to learn and I am proud of your tremendous progress in such a short period of time. Alice, you've started really well and I'm sure you will end up with some fantastic results. Additionally, I am also grateful to all students of the Photon Physics and Experiment Design course for making me a better scientist and teacher. I express my gratitude to our collaborators Stefan Rotter and Matthias Kühmayer from TU Vienna for working so hard to complement our experimental results on scattering invariant modes (Chapter 6) with numerical calculations. Finally, I would like to thank all Bachelor and Master students who brought life to our group and to other former colleagues with whom I had fruitful discussions.

There is also a whole bunch of people outside work who kept me sane and in good spirits amid long, arduous and frustrating days. They played a big role in my personal life and deserve to take some credit for my PhD. First, my housemates Kristof and Gordian who I have spent so much time with, I will cherish the vast range of emotions we shared and the crazy things we did together. My friends Rahaman, Suchi, Teja and Vimmu, thank you for filling

the “Indian” gap in my life and for spending so many memorable evenings together. You are all genuinely kind-hearted and I know I can always count on you. I’m thankful to my badminton family in Utrecht, who have always treated me so well and where I have developed a different side of myself. Special mention goes to my 92-year-old trainer Tjoa, who is a living legend and who continues to inspire me with his energy levels and enthusiasm. Daniel, we seem to connect on a different level and I treasure the deep conversations we have had. Finally, a massive thank you to all my friends, both in India and abroad, for staying in touch with me and for giving me constant support. Navaneeth and Prithiv, our regular calls means a lot to me and shows that distance is not a barrier for effective communication.

Last but not least, I want to thank my entire family, both here in Europe as well as in India, for constantly standing by my side and showering me with unconditional love. I thank my sister for inspiring me to go off the beaten track and to live life on my own terms. My grandmother, a role model in my life, is full of positive thoughts for everyone and has taught me the meaning of patience and compassion. My aunt Sudha-akka, who is always so happy to talk to me, is the most innocent person I know. Finally, I am eternally grateful to my parents for being my ultimate well-wishers and for shaping me into the person I am today. Thank you for showing me the way and for encouraging me to pursue my dreams!

About the author

Pritam Pai was born on 20th October, 1991 in Puducherry, India. In 2012, he graduated with a Bachelor's degree from the Sri Aurobindo International Centre of Education in Puducherry, where he majored in Physics. He then enrolled for a two-year Master's program at the University of Bonn in Germany. He specialized in Experimental Optics and worked for a year on his research project titled "Sub-ballistic transport in coupled dissipative plasmonic waveguide arrays" in the group of Prof. Stefan Linden. He obtained his Master's degree in 2015 and subsequently went on to pursue a PhD under the supervision of Prof. dr. Allard P. Mosk and dr. ir. Sanli Faez at Utrecht University in the Netherlands. In his research, the results of which are described in this thesis, he developed a novel method for measuring the optical response of a sample that allows the retrieval of accurate and faithful statistics of light transport in the sample. He also showed a new application of finding scattering invariant light waves that are transmitted through a disordered material as if it were transparent. In addition to his scientific research, he was a teaching assistant for the Master's course "Photon Physics" for three years, and a course coordinator for the newly introduced "Experiment Design" Master's course. Besides, he also took part in scientific outreach activities by presenting his work on open days of the university and by serving as a member of the Utrecht OSA (Optical Society of America) Student Chapter that promotes optics to the public and in local schools.